

# Wireless Power Charger System for Mobility Scooter

by

Nelcy Pahola PORRAS RODRIGUEZ

THESIS PRESENTED TO ÉCOLE DE TECHNOLOGIE SUPÉRIEURE IN  
PARTIAL FULFILLMENT FOR A MASTER'S DEGREE WITH THESIS IN  
RENEWABLE ENERGIES AND ENERGY EFFICIENCY.  
M.A.Sc.

MONTREAL, JULY 20, 2020

ÉCOLE DE TECHNOLOGIE SUPÉRIEURE  
UNIVERSITÉ DU QUÉBEC



Nelcy Pahola Porras Rodriguez, 2020.





This Creative Commons licence allows readers to download this work and share it with others as long as the author is credited. The content of this work can't be modified in any way or used commercially.



**BOARD OF EXAMINERS**

THIS THESIS HAS BEEN EVALUATED  
BY THE FOLLOWING BOARD OF EXAMINERS

Mr. Kamal AL-HADDAD, Thesis supervisor  
Department of Electrical Engineering, École de technologie supérieure

Lyne Woodward, Chair, Board of Examiners  
Department of Electrical Engineering, École de technologie supérieure

Dr. Rawad Zgheib, External Examiner  
Institut de recherche Hydro Québec IREQ

THIS THESIS WAS PRESENTED AND DEFENDED  
IN THE PRESENCE OF A BOARD OF EXAMINERS AND PUBLIC

JULY 7, 2020

AT ÉCOLE DE TECHNOLOGIE SUPÉRIEURE







## **ACKNOWLEDGMENT**

Foremost, I would like to thank my parents (Jose Maria Porras Peña-Maria Cleotilde Rodriguez) and my family, who had been the most important support. Their deepest love and wise advice taught me to be strong and put my utmost efforts into this thesis.

Throughout my master's degree, I have had the opportunity to be instructed by talented professors who always guided and encouraged me to finish this thesis. Thanks to my supervisor Kamal Al-Haddad, who helped me to finish my studies with patience. A special shout-out to the ETS University. I enjoyed every day at the campus, library, and labs.

Finally, I would like to thank my friends who supported me through this journey.







# **Système de chargement de batteries sans fils pour les scooters de mobilité**

Nelcy Pahola PORRAS RODRIGUEZ

## **RÉSUMÉ**

L'objectif de cette recherche est le développement d'un système de chargement de batteries sans fils pour les scooters de mobilité utilisés par les personnes âgées dont la mobilité est réduite ou par les personnes handicapées. L'ambition de ce système est d'offrir une solution pour les communautés qui dépendent des chaises électriques ainsi que de leurs batteries pour leur offrir un maximum de mobilité et pour améliorer leur qualité de vie. En considérant que l'utilisation des scooters de mobilité dépend directement des capacités de leurs batteries ainsi que du réseau de recharge, une solution sans fils présente au domicile ou dans des places publiques peut offrir plus de mobilité aux personnes utilisant ces scooters. Les systèmes sans fils sont expliqués et les convertisseurs à résonance sont présentés, dans ce travail. Aussi une topologie de convertisseur résonant LLC a été sélectionnée parce qu'il présente les meilleures performances pour la charge de batterie. De plus, la conception de la bobine inductrice sans contact ainsi que sa géométrie prenant la forme en spirale archimédienne sont détaillées. De plus, le contrôle de la tension en boucle fermée est décrit. Un prototype expérimental a été réalisé au laboratoire du GREPCI à l'ÉTS et les résultats expérimentaux sont présentés avec une efficacité de 80% pour 1cm d'espace considérant un convertisseur résonant LLC opérant à une fréquence de 100 kHz et délivrant de la puissance active à une batterie 12V et 12A pour un scooter à mobilité.

**Mots-clés :** transfèrent d'énergie sans fil, scooter de mobilité, mobilité réduite, convertisseur résonant.



# **Wireless power charger system for mobility scooter**

Nelcy Pahola PORRAS RODRIGUEZ

## **ABSTRACT**

The main purpose of this research is to develop a wireless power system in order to charge the batteries of mobility scooters used by the elderly with limited mobility or disabled people. The original intention of this proposed system was not only to offer a solution for the incapacitated community who rely on electrical wheelchair and their batteries for maximum mobility but to improve the groups' quality of life. Considering that mobility scooters' functionality depends directly on battery capacity and charging network, a powerful wireless solution could be located at home or in public places. This wireless power system can provide more freedom and enhanced assisted mobility to those needy people. As a first step, the micro-mobility devices are studied, and the mobility scooters are classified. Then, the power wireless systems are explained, and the resonant converters are shown. An LLC resonant converter is then selected and designed due to its best performance for a battery charging application. Moreover, the coil design and an Archimedean Spiral Design geometry are presented and detailed. Besides, the voltage closed-loop control is described and tested accordingly. Finally, the experimental results, obtained from the experimental setup developed in the GREPCI laboratory, are presented showing the efficiency of 80% with a 1 cm air gap for an LLC converter operating at of 100 kHz resonance frequency and delivering power for a 12 V, 12A battery used for a mobility scooter.

**Keywords:** Wireless power transfer, mobility scooter, reduced mobility, resonant converter.



## TABLE OF CONTENTS

Page

INTRODUCTION .....	1
CHAPTER 1      LITERATURE REVIEW .....	3
1.1      Mobility Vehicles.....	3
1.2      Micro-Mobility Devices.....	5
1.2.1      Pride GoGo Elite Traveler .....	8
1.2.2      Drive Scout 4 .....	9
1.2.3      Merits .....	10
1.3      Wireless Power Systems Classification .....	12
1.3.1      Near Field.....	13
1.3.2      Far Field.....	14
1.4      Wireless Power Standards.....	15
1.5      Electromagnetic interference(EMI) /Electromagnetic Compatibility (EMC) for Wireless Power Transfer .....	16
1.6      Topologies of AC-DC Resonant Converters .....	18
1.7      Resonator Structure.....	25
1.8      Application: 200 W WPT system with Data Transfer .....	29
1.9      Control strategies of the LLC converter topology .....	31
1.9.1      Variable Frequency .....	32
1.9.2      Constant Frequency Operations.....	34
CHAPTER 2      ANALYSIS OF THE LLC CIRCUIT TOPOLOGY .....	37
2.1      LLC Circuit Topology .....	37
2.1.1      Fundamental characteristics of the LLC resonant converter .....	37
2.2      Operation of a Full Bridge Resonance Converter.....	39
2.2.1      Waveforms in the resonant converter .....	39
2.2.2      Data transmission between transmitter and receiver .....	39
2.2.3      Loosely coupled system.....	39
2.2.4      Closely Coupled System.....	40
2.3      First Harmonic Approximation.....	41
2.4      Impedance Calculation.....	44
2.4.1      Theory of resonant tank operation .....	45
2.5      Transfer Function.....	49
2.6      Design and simulation of simplified circuit using MATLAB .....	52
CHAPTER 3      DESIGN PROCEDURE OF THE COUPLING COILS .....	59
3.1      Design of Wire Litz for the Coupling Coils.....	59
3.1.1      Calculating Overall Gauge of the Wire .....	60
3.1.2      Number of Strands .....	60
3.1.3      Construction of the Litz Wire .....	61



3.2	Design of coils' geometry .....	63
3.3	Simulation of Coils in MATLAB .....	67
3.3.1	The Spiral Resonator.....	68
3.3.2	Resonance Frequency and Mode .....	68
3.3.3	Coupling Mode between Two Spiral Resonators .....	69
3.3.4	Variation of System Efficiency with Transfer Distance .....	70
3.4	Laboratory Tested Coils.....	72
CHAPTER 4 CONTROL OF LLC CONVERTER .....		77
4.1	Modelling of the System .....	77
4.1.1	The Root Locus.....	78
4.1.2	Representation using Bode Diagram .....	81
4.2	Voltage Control Loop .....	82
4.3	Compensator PI Design .....	83
4.3.1	The Root Locus of the PI (Close Loop).....	84
4.3.2	Bode Diagram of the PI .....	87
4.4	Simulation in MATLAB .....	87
CHAPTER 5 EXPERIMENTAL VALIDATION .....		91
5.1	Design of PCB- LLC and rectifier .....	91
5.1.1	PCB LLC Primary.....	91
5.1.2	PCB LLC Secondary.....	92
5.2	Description of Hardware Setup.....	92
CHAPTER 6 EXPERIMENTAL RESULTS.....		97
6.1	Output Inverter.....	97
6.2	Air Gap Variations.....	98
6.2.1	Air Gap variation of 1 cm .....	99
6.2.2	Air Gap variation of 2 cm .....	100
6.2.3	Air Gap variation of 5 cm .....	101
6.2.4	Air Gap variation of 10 cm .....	102
6.3	Experimental results.....	103
6.4	DC exit on the Battery .....	104
6.5	System efficiency .....	104
6.6	200 W System .....	105
CONCLUSION .....		107
APPENDIX A .....		111
APPENDIX B .....		113
APPENDIX C .....		117
LIST OF BIBLIOGRAPHICAL REFERENCES.....		125



## LIST OF TABLES

	Page
Table 1.1.	Structure description of micro-mobility vehicles(International, 2019) .....6
Table 1.2	Scooters selected.....7
Table 1.3	Diagnostic code of the Pride GoGo elite (Corp, 2012).....9
Table 1.4	Code Fault of the Drive Scout 4 (Manufacturing, 2017 .....10
Table 1.5	Flash Code Error(Merits).....11
Table 1.6	Topologies with high resonant WPT (Cem Som, 2019).....20
Table 2.1	Design Specification .....51
Table 5.1.	Components of the designed WPT Charger Scooter. ....95
Table 6.1	Efficiency.....104







## LIST OF FIGURES

	Page
Figure 1.1	Micro-mobility vehicles.....5
Figure 1.2	Code classification of micro-mobility devices(International, 2019) .....7
Figure 1.3	Scooter GoGo Pride (Corp, 2012) .....8
Figure 1.4	Battery Pack GoGo Pride(Corp, 2012) .....8
Figure 1.5.	Typical problems with mobility scooters.....12
Figure 1.6	WPT Classification(Jawad, 2017) .....13
Figure 1.7	WPT in resonance inductive (Longzhao Sun, 2018) .....14
Figure 1.8	WPT Standards (Cem Som, 2019).....15
Figure 1.9	General WPT architecture(Cem Som, 2019).....17
Figure 1.10	Classification of the resonant circuits used.....19
Figure 1.11	WPT Systems Topologies (Sheng-Yang, 2018) .....21
Figure 1.12	Gain curves vs frequency of a CL series resonant topology.....22
Figure 1.13	Gain curves vs frequency of an LC parallel resonant topology.....23
Figure 1.14	Gain values vs frequency of a CL parallel resonant topology .....24
Figure 1.15	Resonant structure geometries for WPT systems (Abou Houran, 2018)...25
Figure 1.16	Classification of Litz constructions types (technologies, 2018) .....28
Figure 1.17	Topology of Inductances in a WPT system (Cem Som, 2019).....29
Figure 1.18	200 WPT development kit (Elektronik, 2019).....29
Figure 1.19	Current flow transmitter through the 200W. WPT system .....30
Figure 1.20	Current flow receiver through the 200W. WPT system .....30
Figure 1.21	Control types in an LLC converter .....32
Figure 1.22	Diagram of a voltage-controlled oscillation for an LLC converter .....33



Figure 1.23	Diagram of Self-Sustained Oscillation Control for an LLC converter .....	34
Figure 1.24	Diagram of Asymmetrical PWM control for an LLC converter.....	35
Figure 1.25	Diagram of a modulator pulse control in the secondary side of the LLC converter .....	36
Figure 2.1	LLC Converter topology.....	38
Figure 2.2	A typical configuration of the resonant converter .....	42
Figure 2.3	Simplified converter circuit squared showing $V_{os}$ and $V_{sq}$ . No linear non-sinusoidal circuit .....	42
Figure 2.4	Equivalent Circuit of the converter. Linear sinusoidal circuit.....	43
Figure 2.5	Resonant Tank equivalent circuit non-sinusoidal circuit.....	44
Figure 2.6	Resonant Tank equivalent circuit linear sinusoidal circuit .....	45
Figure 2.7	LLC Regions (Appendix A, Solving equation 2.5 varying $Q_e$ ). .....	46
Figure 2.8	LLC Operation (Huang, 2011).....	48
Figure 2.9	ZVS Gain for different $Q_e$ .....	48
Figure 2.10	Bode diagram of the LLC Tank impedance.....	49
Figure 2.11	Converter Specifications step-by-step design and circuit parameter selections.....	51
Figure 2.12	Voltage-gain function $M_g$ with different values of $L_n$ . .....	53
Figure 2.13	Simplified circuit of the LLC converter.....	56
Figure 2.14	Output voltage from the LLC converter .....	56
Figure 2.15	Areas showing ZVS and ZCS converter operation. ....	57
Figure 2.16	Peak-gain curves in MATLAB .....	58
Figure 3.1	Litz Design process.....	59
Figure 3.2	Spiral Coil. ....	63
Figure 3.3	Coil Diameters .....	63
Figure 3.4	Coil Distances .....	63



Figure 3.5	Coil Geometry.....	66
Figure 3.6	Primary coil inductance measures .....	67
Figure 3.7	Secondary coil inductance measures .....	67
Figure 3.8	Antenna mesh (Appendix C) .....	68
Figure 3.9	Spiral Impedance (Appendix C) .....	69
Figure 3.10	Magnetic Field (Appendix C) .....	70
Figure 3.11	S Parameters.....	71
Figure 3.12	Efficiency (Appendix C).....	71
Figure 3.13	Setup use for the VNA Test. ....	72
Figure 3.14	S Parameter (Smith Chart with the Y (real part) and Z (Imaginary)).....	73
Figure 4.1	Conversion scheme block diagram used in the simulation. ....	77
Figure 4.2	Root locus of the system with Re of 1 Ohm .....	78
Figure 4.4	Root locus of the system with Re of 50 Ohms.....	79
Figure 4.5	Root locus of the system with Re of 80 Ohms.....	80
Figure 4.6	Root locus of the system with Re of 1000 Ohms.....	80
Figure 4.7	Bode Diagram of the LLC system .....	81
Figure 4.8	Feedback Control loop.....	82
Figure 4.9	Digital Feedback Control loop.....	83
Figure 4.10	Root locus of the close system with PI compensator and Re of 1 Ohm ....	84
Figure 4.11	Root locus of the close system with PI compensator and Re of 20 Ohms.	85
Figure 4.12	Root locus of the close system with PI compensator and Re of 50 Ohms.	85
Figure 4.13	Root locus of the close system with PI compensator and Re of 80 Ohms.	86
Figure 4.14	Root locus of the close system with PI compensator and Re of 1000 Ohms .....	86
Figure 4.15	PI Controller Bode .....	87



Figure 4.16	Simulation of the LLC converter topology with PI Controller.....	88
Figure 4.17	PI Parameters .....	88
Figure 4.18	Output signal of the LLC converter with the PI controller .....	89
Figure 4.19	FET Voltage and Current.....	90
Figure 5.1	Scheme of LLC primary circuit .....	91
Figure 5.2	PCB design of LLC primary circuit.....	91
Figure 5.3	Scheme of rectifier secondary.....	92
Figure 5.4	PCB of rectifier secondary circuit.....	92
Figure 5.5	3D Rectifier and Filter. ....	92
Figure 5.6	Hardware setup in the laboratory .....	93
Figure 5.7	WPT Scooter Charger fully implemented.....	96
Figure 6.1	Experimental setup for the inverter circuit .....	97
Figure 6.2	Oscilloscope waveforms at the Inverter Output.....	98
Figure 6.3	Design circuit and hardware connections/Channels in the oscilloscope ...	98
Figure 6.4	Current and voltage levels at the primary and secondary coils for an air gap of 1 cm between coils, max power transfer.....	99
Figure 6.5	Current and voltage levels at the primary and secondary coils for an air gap of 2 cm between the coils. ....	100
Figure 6.6	Current and voltage levels at the primary and secondary coils for an air gap of 5 cm between the coils .....	101
Figure 6.7	Current and voltage levels at the primary and secondary coils for an air gap of 10 cm between the coils .....	102
Figure 6.8	Current and voltage levels at the primary and secondary coil with short circuit operation. ....	103
Figure 6.9	Voltage levels at battery and in the secondary coil.....	104
Figure 6.10	Waveforms from 200 W kit showing both v and i.....	105
Figure 6.11	200 W kit hardware setup in GREPCI Lab.....	106



## **LIST OF ABBREVIATIONS**

EV	Electrical vehicle
MOD	Mobility demand
RIFD	Radio frequency identification
WPT	Power wireless transfer
PMBLMS	Permanent Magnet brushless motors
HMI	Human machine interface
BLDM	Brushless Linear Motor
EFM	Electric Force Motors
WIDIS	Wheel Independent Drive and Independent Steering
EMI	Electromagnetic interference
EMC	Electromagnetic compatibility
ISM	Radio spectrum reserved internationally for industrial, scientific and medical
RF	Radio Frequency
IEEE	Institute of electrical and electronics engineers
FCC	Federal communications commission
SAR	Specific absorption rate (SAR)
APWM	asymmetrical pulse-width-modulated
SSOC	Self-Sustained Oscillation Control
VCO	Voltage controlled oscillation
PDM	Pulse Density Modulation Control
AWG	American Wire Gauge







## INTRODUCTION

Nowadays, the power of wireless transfer is studied by many companies, and researchers around the world are making charging systems for electric cars, mobile phones, and domestic electronics. One of the markets for this technology, which has a great social impact, is mobility vehicles for disabled and/or elderly people with limited autonomy.

While reviewing the prior art discussing mobility aids and the differences between frames, robots and the 3- and 4-wheel scooters, the most common use of scooters is the 4-wheel scooter base on the literature review (International, 2019) this type of scooters provide a better stabilizing function as well as a room for groceries and a comfortable sitting position, with 12-20 V batteries and an output current 8-12A storing nominal energy reaching 240 Wh.

Since, these wireless power charging systems are already available in the marketplace, none are available especially for mobility scooters employing voltage ranges and current outputs. The goal of this research is to develop a power wireless transfer particularly designed for mobility scooters.

The wireless power transfer is defined by the transmitter (Tx) and receiver (Rx), which basically define the efficiency of the system as measured by the air gap length between the two coils. An Archimedean Spiral Design is proposed and simulated in MATLAB. Furthermore, a voltage control (PI) circuit is tuned, and experimental results are presented and elaborated. A prototype is developed with a maximum input voltage of 10 V and the air gap from 1 cm to 10 cm, with an efficiency of the system around 80% at 1 cm with a switching frequency of 100 kHz.



## **OBJECTIVES**

The main objective of this research is to develop a wireless charging system for mobility scooters. First, identifying the most common scooters that are studied in the USA and Canada market. Based on the chosen model, a wireless power system charging of 12 V and 12 A is selected. Moreover, having the electrical specifications of the prototype a DC-DC converter is proposed with a switching frequency of 100 kHz. Then, a voltage control with a PWM on the primary gates is proposed. Finally, a hardware setup is created in the GREPCI laboratory.



## **CHAPTER 1**

### **LITERATURE REVIEW**

#### **1.1 Mobility Vehicles**

One of the most common symptoms in elderly people is the decreasing function of their musculoskeletal system with a higher tendency for women. Issues like osteoporosis and dorsal arthritis predominantly in those over age 60, almost always affect the hips and knees. Consequently, the loss of independence and a poor quality of life can affect their social life. Activities, which were once a part of their normal daily life, such as buying groceries or even having a medical appointment can become an excruciating and all-day marathon. Due to the reduction of mobility, depression, and isolation often develop in these types of patients. As a solution, medical aids have been developed. Some of these aids include wheelchair, frames, and mobility scooters. As an example, researchers have compared a walking frame, active which is the one with electrical motors and passive which has no motor on the prototype. The frame with motor is a regular walking aid, some of them can have on the top of the wheels, a 24 DC motor to control the torque and the speed. The system has a contact sensor to check if the user is on the frame and a lithium-ion battery with a nominal voltage of 25 V and 15 A as a current output in addition to a control box with AVRATMega 32A microcontroller is used.

On the other hand, MOD (mobility demand) services like Uber and Lyft have been helping users who tend to take a fast and safe transport method. Therefore, the most common solutions are mobility scooters, because they are autonomous and reliable. It is expected that the next generation of mobility includes autonomous vehicles, especially in cities like Singapore. Some of these vehicles have mapping and localization in 3D, dynamic re-planning path capability for online obstacles avoidance, and a web-based booking system. Also, it is mentioned how autonomous vehicles have been developed by model predictive equilibrium point control (MPEC), a control system consisting of the quick and responsible decisions taken by the vehicle



As a summary of this research, a planner takes the decisions and plans the path for the user. Moreover, this system is using a camera in the seat, a computer with the ubuntu operation system, a joystick, and an STM32F4 microcontroller.

The electric characteristics of mobility scooters are studied,(Kim, 2015 ) where a scooter uses a DC brush motor and the mechanical commutation causes low power density, low reliability, and poor heat dissipation. One type of motor is the permanent magnet brushless motors (PMBCMS) that have high efficiency, low noise, low moment of inertia, and free maintenance. Nevertheless, this magnet motor can be divided into two categories, a Brushless Linear Motor (BLDM) with a trapezoidal back Electric Force Motors (EFM) and a permanent magnet synchronous motor (PMSM) with a sinusoidal back EFM. The claim of this study is to show how the PMSM has more efficiency than the other motors under a sinusoidal commutation. Besides, the electrical design in scooters, a PWM control method for a steering wheel in an electric mobility scooter is explained (B. Kim, 2012). Mainly a 4-wheel scooter is developed using an android tablet as a human-machine interface (HMI) and the control of the four-individual wheel unit achieves the best performance in speed, low effort transport in a street environment.

Another kind of smart mobility vehicle is a robot scooter. An example of a robot with a complete autonomous mobility system running in an urban area with other robots and bicycles in the streets of Japan was developed. The navigation system of the robot, path following, obstacles avoidance, and grid map matching were presented (J. Sallan, 2009). A mobility scooter was modified with a SH 7125 microcontroller, DC gear, and a fiber-optic gyro TA60007, showing as a result an autonomous scooter robot running a 1.1 km in a real environmental area. Unfortunately, the aid solutions for elderly people sometimes have a problem with technical support, battery maintenance and life expectancy.



Therefore, companies such as Pride, Drive, and Metits have been studying the power wireless transfer technology as an environmentally suitable solution for better maintenance and life expectative of batteries. Usually, the batteries in those scooters must be changed after 6 months of daily use. The wireless power transfer (WPT) is a safe, convenient, and a smart solution for electric vehicles. However, these systems have less efficiency than their wired charging counterparts.

## 1.2 Micro-Mobility Devices

While classifying the e-mobility vehicles, micro-mobility is the definition of small vehicles, such as e-bikes and scooters as shown in Figure 1.1. Moreover, a SAEJ3104 human electric vehicle for driveline/roadways interaction standard was developed, where the safety is evaluated taking the batteries and the top speed on the pathways into consideration. (International, 2019).

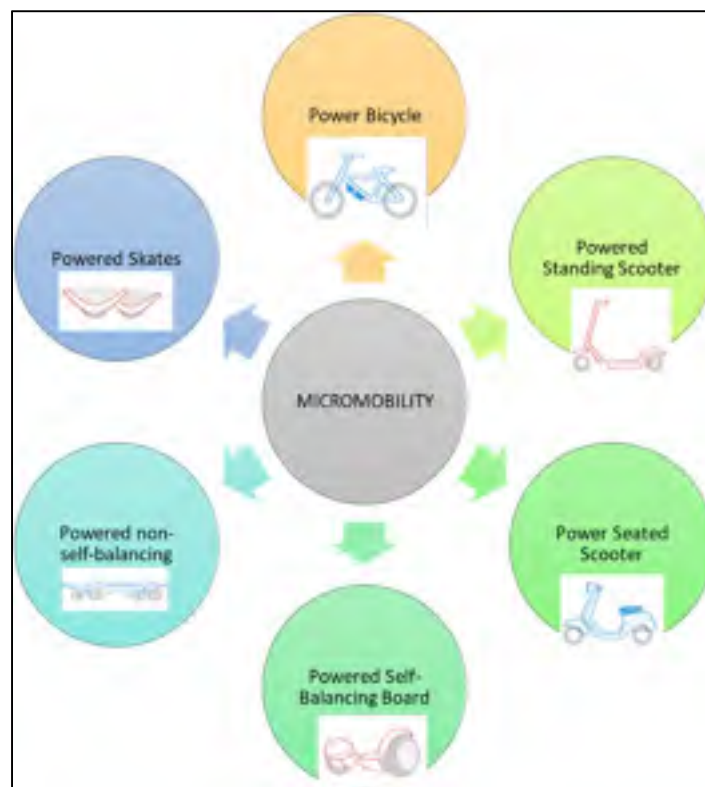


Figure 1.1 Micro-mobility vehicles



Table 1.1 shows, the physical features of each vehicle, such as self-balancing, seat, and operable pedals. These characteristics are used for the sake of structure, description, and comparison.

Table 1.1. Structure description of micro-mobility vehicles  
(International, 2019)

<b>STRUCTURE DESCRIPTION</b>	<b>Center Column</b>	<b>Seat</b>	<b>Operable pedals</b>	<b>Floorboard/foot pegs</b>	<b>Self-balancing</b>
<b>Powered Bicycle</b>	Yes	Yes	Yes	Possible	No
<b>Powered Standing Scooter</b>	Yes	No	No	Yes	No
<b>Powered Seated Scooter</b>	Yes	Yes	No	Yes	No
<b>Powered Self-balancing board</b>	Possible	No	No	Yes	Yes
<b>Powered Non-Self-Balancing Board</b>	No	No	No	Yes	No
<b>Powered Skates</b>	No	No	No	Yes	Possible

On the other hand, Figure 1.2, shows the classification codes of the vehicle with special requirements. This is the categorization of the micro-mobility vehicles for the SAE standard.



Name	Code	Description
<b>Curb weight</b>		
Ultra lightweight	WT1	Curb weight ≤ 50 lb (23 kg)
Lightweight	WT2	50 lb (23 kg) < curb weight ≤ 100 lb (45 kg)
Midweight	WT3	100 lb (45 kg) < curb weight ≤ 200 lb (91 kg)
Midweight Plus	WT4	200 lb (91 kg) < curb weight ≤ 500 lb (227 kg)
<b>Vehicle width</b>		
Standard-width	WD1	Vehicle width ≤ 3 ft (0.9 m)
Wide	WD2	3 ft (0.9 m) < vehicle width ≤ 4 ft (1.2 m)
Extra-Wide	WD3	4 ft (1.2 m) < vehicle width ≤ 5 ft (1.5 m)
<b>Top speed</b>		
Ultra low-speed	SP1	Top speed ≤ 8 mph (13 km/h)
Low-speed	SP2	8 mph (13 km/h) < top speed ≤ 20 mph (32 km/h)
Medium-speed	SP3	20 mph (32 km/h) < top speed ≤ 30 mph (48 km/h)
<b>Power source</b>		
Electric	E	Powered by an electric motor
Combustion	C	Powered by an internal combustion engine

Figure 1.2 Code classification of micro-mobility devices(International, 2019)

For this project, the e-mobility vehicles that are going to be used are mobility scooters. Doing some research on price and efficiency on the actual mobility scooter market, the electrical parameters design were considered for follow the brands shown in Table 1.2.

Table 1.2 Scooters selected

BRAND	PRIDE	DRIVE	MERITS
SERIE	GoGo Elite Traveler	Scout 4	S141, Pioneer 4
BATTERY	12V/18Ah	12V/18Ah	12V/35Ah
PRICE/BATTERY EACH	47\$	47\$	93\$



### 1.2.1 Pride GoGo Elite Traveler

The PRIDE scooter consists of 4 wheels, mobility seat, a key switch, throttle control lever, horn button, speed adjustment dial, and battery charge level meter. The battery model is shown in Figure 1.4 which includes 2 batteries of 12 V/18Ah.



Figure 1.3 Scooter GoGo Pride (Corp, 2012)

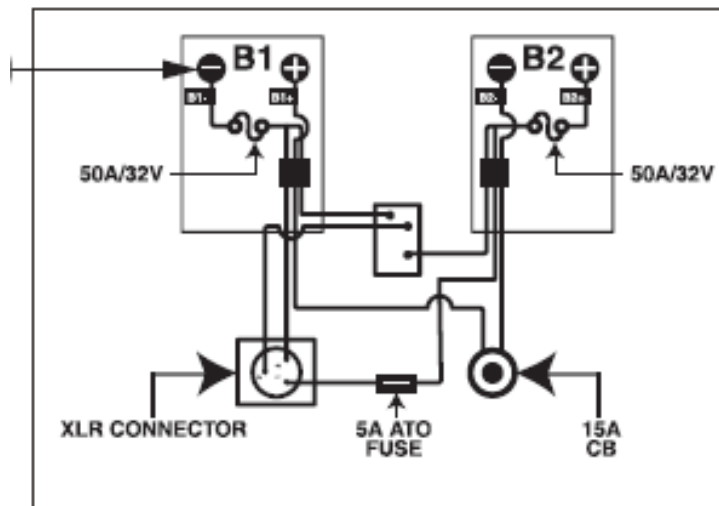


Figure 1.4 Battery Pack GoGo Pride(Corp, 2012)



Table 1.3 shows the diagnostic code error. That process helps the final user to figure out the behavior of the scooter. Some of them (1,2,3) are related to the battery status and are easy to solve with a battery charger or a charger station nearby.

Table 1.3 Diagnostic code of the Pride GoGo elite(Corp, 2012)

DIAGNOSTIC CODE	CONDITION	SOLUTION
■ (1)	Battery voltage is too low to operate the Travel Scooter.	Charge batteries as soon as possible.
■■ (2)	Battery charge is too low.	Charge batteries.
■■■ (3)	The Travel Scooter's battery voltage is too high to operate the scooter, or the charger is still connected to the off-board charger port.	Unplug charger and/or turn key off, then back-on again. If traveling down a slope, reduce Travel Scooter speed to the minimum setting.
■■■■ (4)	Current limit time out.	Turn the Travel Scooter off for a few minutes, then turn your Travel Scooter back on.
■■■■■ (5)	The manual freewheel lever is in the (forward) freewheel position.	Remove the key from the key switch, then push the manual freewheel lever to the drive (rearward) position and restart your Travel Scooter.
■■■■■■ (6)	Throttle control lever not at center position at start up.	Verify that the batteries are fully charged. If the batteries are fully charged, then return the throttle control lever to center position, turn Travel Scooter off then back on.
■■■■■■■ (7)	Speed put away.	Contact your authorized Provider for assistance.
■■■■■■■■ (8)	Minor faults occur.	Contact your authorized Provider for assistance.
■■■■■■■■■ (9)	Other internal errors.	Contact your authorized Provider for assistance.

## 1.2.2 Drive Scout 4

The Drive Scout 4 scooter consists of a wheel mobility chair that is light, easy to drive and has a troubleshooting process (Table 1.4). In this case, the problems are indicated through LEDs located in front of the steering wheel.



Table 1.4 Code Fault of the Drive Scout 4 (Manufacturing, 2017)

Flash Code	Description	Recommended Action
1,1	Thermal Fault	Power off the scooter, let rest for 15 minutes, and power on
1,2	Throttle Fault	Check throttle connection, replace if necessary
1,3	Speed Pot Fault	Check speed pot connection, replace speed pot if necessary.
1,4	Low Voltage	Charge the battery pack
2,3	Main Fault	Contact your authorized Drive Medical Provider
3,2	Brake Fault	Engage the freewheel lever to “drive” mode
3,4	Throttle Fault	Make sure the throttle is in the rest or neutral position when powering on
4,5	Battery Fault	Check connections to the battery & charge the battery pack if necessary

### 1.2.3 Merits

This Merits scooter is slightly bulkier than the other two, and its error indicator is a LED located onto the steering wheel. The number of flashes indicates the errors as shown in Table 1.5.



Table 1.5 Flash Code Error(Merits)

Flash Code	Description
1	Battery needs recharging
2	Battery voltage too low
3	Battery voltage too high
4	Current time limit out
5	Magnetic Brake fault
6	Not in neutral at power up
7	Speed pot error
8	Motor volts error
9	Other internal error

Among the flash codes, the first 3 are referring to the battery state. After studying the three scooters' pride mobility was selected, then a literature review of power wireless systems for this type of battery will be presented.

Some of the mechanical problems that can be presented with these scooters are shown in Figure 1.5, As an example with the GoGo elite scooter (Pride), a bearing had to be changed after taking a slope of more than 45 degrees. Another issue presented with thee Scout4 (Drive), it was a peak current on the charger that caused the controller to get burnt. For the other scooter the merits of the S141 Pioneer after a week of use, the batteries must be changed.



GoGo Elite Traveller (Pride)	Scout 4 (Drive)	S141 Pioneer 4 (Merits)
 <p>Cost: \$150</p>	<p>Curtis Model 1212 Motor Speed Controller (control of permanent magnet drive motors for battery powered vehicles)</p>  <p>Cost: \$210</p>	<p>New Batteries after 1 week</p>  <p>Cost: \$200</p>

Figure 1.5. Typical problems with mobility scooters

### 1.3 Wireless Power Systems Classification

For the last few decades, a huge interest in WPT has developed. This technology has been viewed as a viable alternative to reduce the need for wires.

The types of transmission can be divided into two categories: far field and near field. The first one is mainly designed for low-power applications with lower priority of transmission efficiency. This system is normally used with microwave or laser. The second one, the near-field transmission, is highly efficient and less radiofrequency is presented. The resonant coupling has become dominant in WPT as is shown in Figure 1.6.



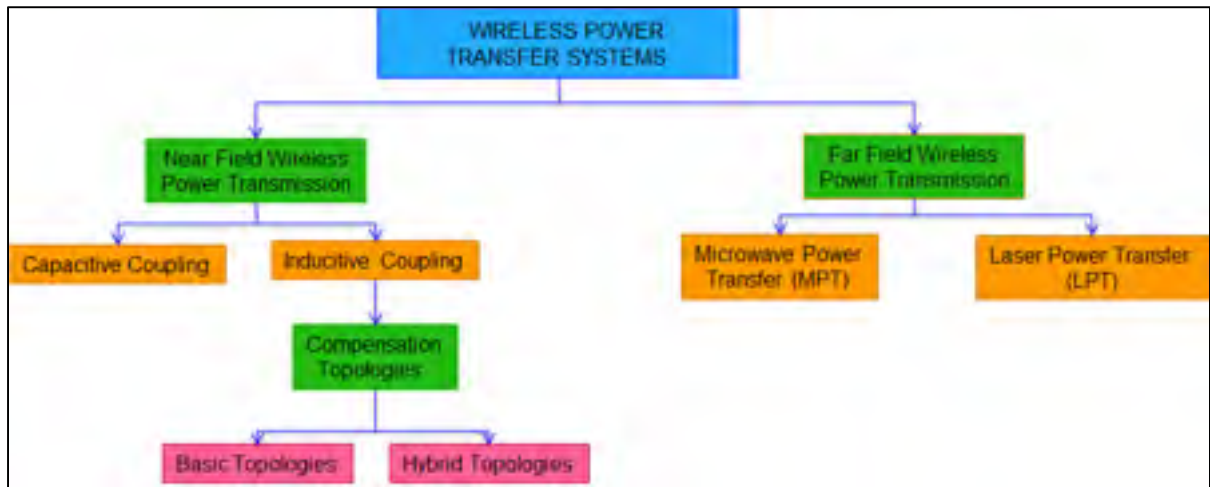


Figure 1.6 WPT Classification(Jawad, 2017)

### 1.3.1 Near Field

Near-field wireless energy transfer can be conducted using wire coils with a short distance. Moreover, it can work with an operational frequency of around 10 kHz to several mega-Hertz. Near field is subdivided into the following categories.

**Capacitive coupling:** transferring energy between two electrodes that form a capacitance, where electric fields are created, and displacement current maintains the current stability.

**Resonant Inductive Coupling:** there is normally a low coupling between the coils. Mostly on these systems, a large inductance voltage is primarily necessary. Consequently, a high current is generated, and greater losses are present in both coils, quantified by the Q factor. It is normal in order to compensate for the secondary leakage inductance; as a result, a capacitance is connected in parallel or in series with the coil. This kind of system is one of the most popular. A simple flowchart is shown in Figure 1.7.



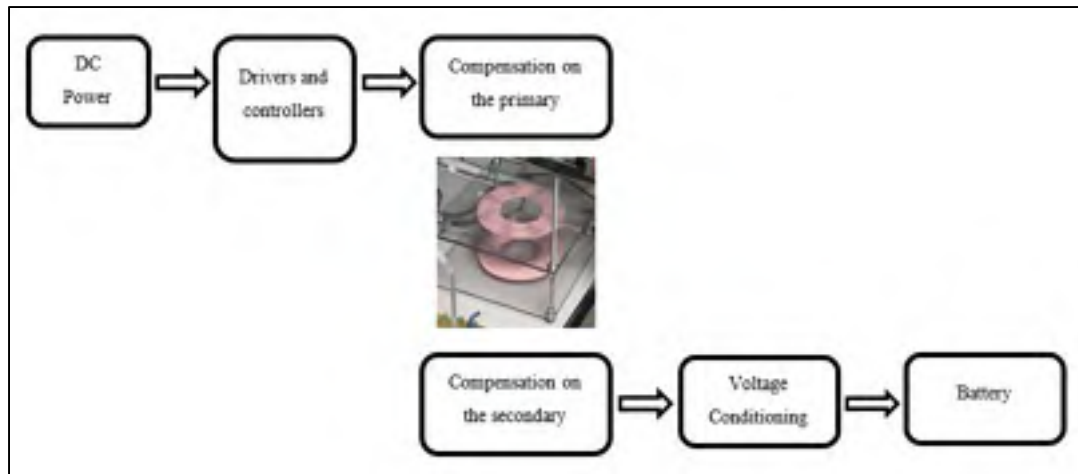


Figure 1.7. WPT in resonance inductive (Longzhao Sun, 2018)

**Inductive Coupling:** In this case, a conductor with a current flowing generates a magnetic field. When the wire is wound into a coil, the magnetic field is concentrated. Basically, the magnetic field strength of a coil is defined by the flux density.

### 1.3.2 Far Field

With this technology, energy can be transferred over several kilometers.

### Microwave power transmission

The power transmission which consists of electric energy conversion to microwaves using a magnetron. On reception, microwave energy is converted to electrical energy using a rectifier and an antenna.

### Laser Radiation:

Photonic energy is transferred from the transmitter to the receiver using a laser. This technology allows for a high energy concentration in long distances. The power can be transmitted without high-frequency interference. Besides, this energy can be transmitted via



free space or optical conductors. However, poor efficiency can be reached depending on the weather conditions. However, the transmitter and the receiver must have a line of sight contact.

Near field is going to be used for the battery charger on the mobility scooter with a resonant coupling based on the descriptions that were mentioned in this chapter such as distances between the coils, frequency and coupling. In the next section, different topologies of resonant converters are going to be explained in order to choose the best topology for this project.

## 1.4 Wireless Power Standards

Nowadays there are two low power wireless power standards as illustrated in Figure 1.8. The Qi and the AirFuel. The wireless power consortium or Qi standard is characterized by the coupling between the two coils, the transmitter, and the receiver and the alignment between them. The most popular application is the phone charger. This standard uses band communication. In contrast, the AirFuel Alliance architecture is like Qi, but the coil structure is different. On the AirFuel, the coils are loosely coupled. Consequently, high leakage is presented.

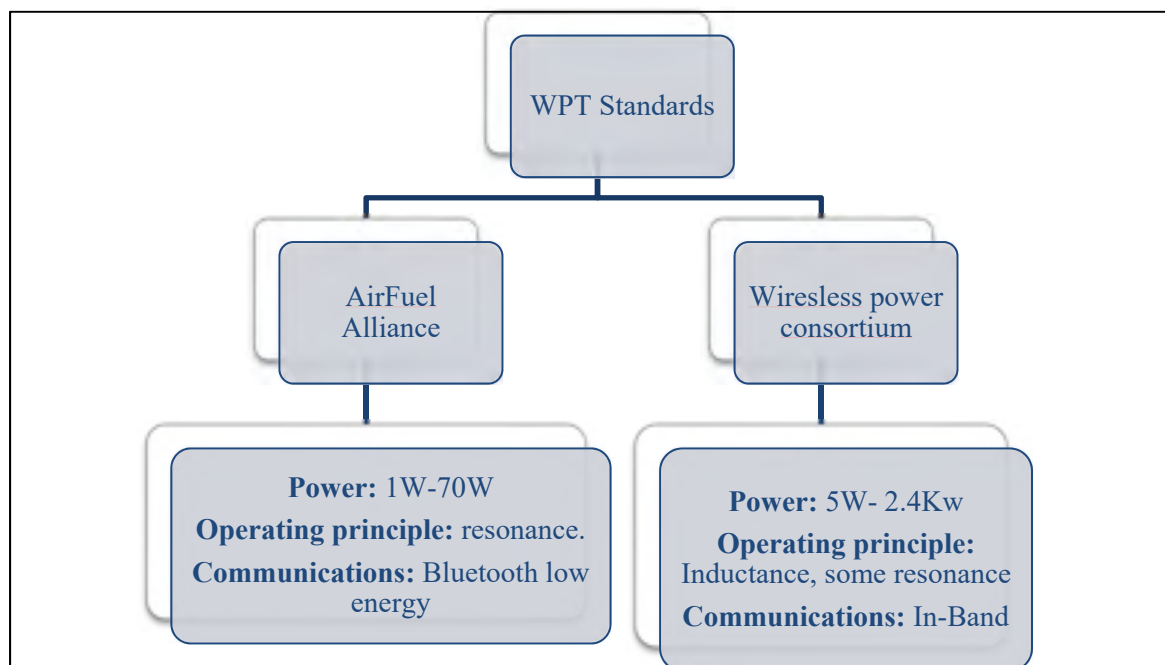


Figure 1.8 WPT Standards (Cem Som, 2019)



## **1.5 Electromagnetic interference (EMI) /Electromagnetic Compatibility (EMC) for Wireless Power Transfer**

Electromagnetic interference (EMI) and Electromagnetic Compatibility (EMC) protection is important in WPT systems and should be considered during the R&D process. Highly resonant power transfer systems based on AirFuel standards are subject to EMI regulation as any other power converter as well as other regulations.

The EMI propagation in a wireless power system is more difficult than traditional power circuits because classic techniques significantly impact the performance of the coil and tuning circuits. There are three standards that govern EMI:

- The radiated EMI limits;
- The internationally for industrial, scientific and medical (ISM) bands;
- The non-ionizing human radio frequency exposure limits.

The biggest challenge for consumer wireless power products, based on the AirFuel standard, covers the frequency range of radiated emissions from 6 MHz to 1 GHz. The ISM band radiator standards limit the frequency bandwidth of radiated energy but essentially allow unlimited radiated power, with a few exceptions in the frequencies targeted for wireless power transfer. However, the limits for exposure to human radiofrequency (RF) adopted by the Federal communications commission (FCC), the institute of electrical and electronics engineers (IEEE), and the International Commission for Protection against Non-Ionizing Radiation (ICNIRP): based on specific absorption rate (SAR) become the power limiting factor for the wireless power transfer systems.

AirFuel-based wireless power transfer systems operate at 6.78 MHz which is an unlicensed ISM band frequency, with 13.56 MHz and 27.12 MHz as additional suitable ISM band frequencies, which can be used in special cases and power levels. Near Field Communications (NFC), popular in products such as RFID and card readers, which now include smartphones, use Citizen Band 13.56 MHz radio, licensed, and many radio-controlled devices use 27.12



MHz. These two frequencies are the 2nd and 4th harmonics of 6.78 MHz and some designers have suggested that since these frequencies are also ISM bands, the need to suppress EMI at these frequencies can be relaxed, thereby reducing the requirements for EMI filter design. This approach is not recommended because products, such as smartphones, already include NCF functionality, which can be damaged by the wireless power transfer system.

A radiated EMI system consists of five basic components: 1) an EMI source, 2) a transmission path 3) a radiator (antenna) 4) a receiver and 5) the radiated EMI standards that define the spectral limits of electromagnetic energy, as shown in Figure 1.9.

EMI filtering is not considered as a component of an EMI system, but rather as a means of limiting the propagation of energy in the system and the frequency range in order to minimize the electromagnetic emissions from the antenna. The receiver should not be confused with the receiver used for EMI testing, but rather any circuit (receiver) that can be corrupted by the radiated spectral energy. In addition, a far-field receiver, like the one used for EMI compliance testing, cannot distinguish whether the source is an H-field ( $di/dt$ ), an H-field can inductively couple interference currents into neighboring conduction paths or an E field ( $dc/dt$ ) is the measurement of interference voltage.(Cem Som, 2019).

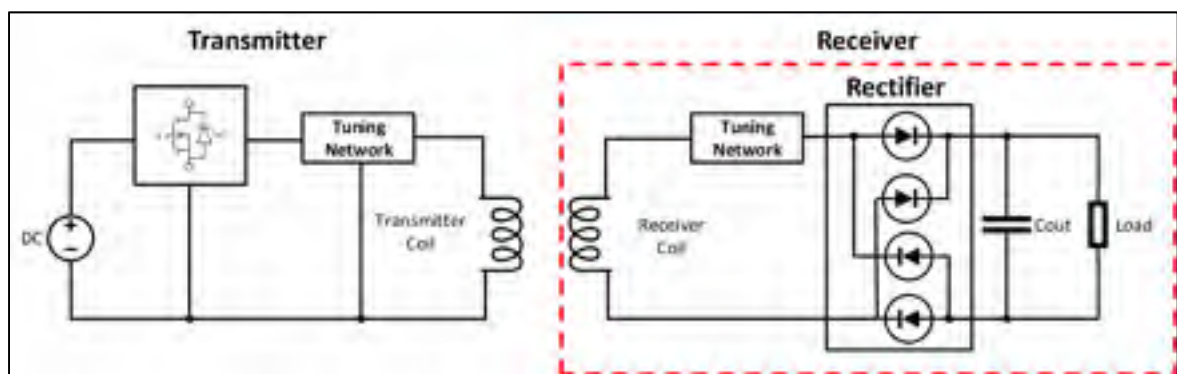


Figure 1.9. General WPT architecture(Cem Som, 2019)

The EMI radiator in a traditional power electronic product can be a combination of circuit boards, cable harnesses, and ports. This is true for a wireless power product too, but the source



coil becomes the main radiator due to its size, construction, and function. For this reason, EMI radiators, owing to the balance of the wireless system, are not discussed as they are equivalent to traditional power electronic products, and classic solutions can be used for EMI compliance. The source coil is simply a large inductor with high impedance. Current in the coil is supplied by the amplifier which is enhanced by series-tuning the coil with a capacitor to yield low impedance. This current generates the H-field used for power transmission and thus radiates any spectral energy present in the current. All frequencies, except for the fundamental transmission frequency, are deemed unwanted as they can exceed the EMI limits imposed by the standards and must, therefore, be adequately attenuated from the current prior to entering the source coil.

## **1.6 Topologies of AC-DC Resonant Converters**

Electrical resonance occurs in an AC circuit when the two reactances which are opposite and equal cancel each other for a determinate frequency, which is denominated as a resonance frequency. As an example of a resonance circuit, a capacitor and an inductor can be connected in series, when the resonance frequency indicates the real and imaginary impedances are equal but with opposite signs; consequently, the real part remains due to ESR (Equivalent Series Resistance).

Therefore, working with a WPT system in resonance allows the maximum power transfer of energy defined also by the distance between the coupled coils sharing the same magnetic path. Considering that the losses in the circuit are due to the parasitic resistances of the real components determined at the resonance frequency, this leads to the best performance that can be obtained by such a system.

The WPT consists of a transmitter and a receiver. This AC input is rectified after the transfer coils which can be circular, rectangular, or of other kinds. The resonant circuits used in the industry are shown in Figure 1.10.



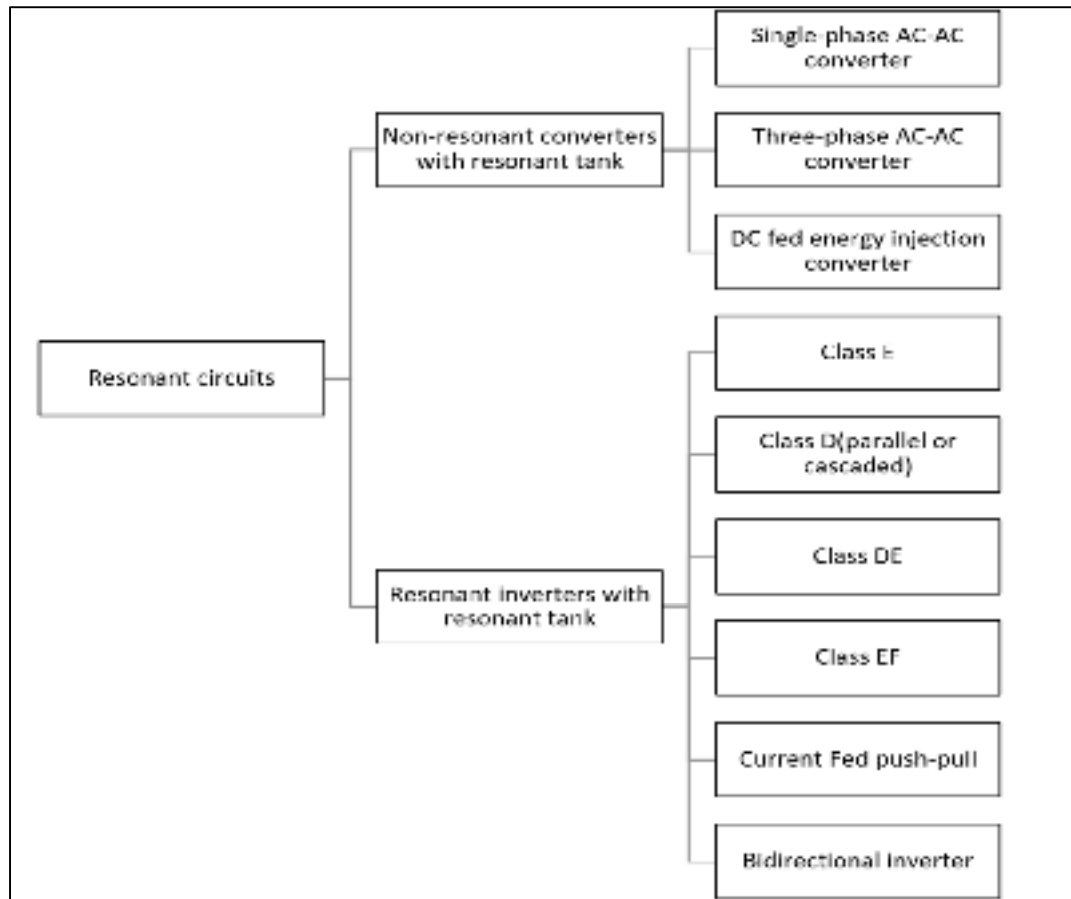


Figure 1.10 Classification of the resonant circuits used in the industry (Jiang, 2017)

Some characteristics of these resonant circuits can be listed as follows: the AC-DC converters help to use an AC power from the grid to DC power.

These topologies can be listed as:

- Single-phase AC-AC converters: can show free oscillation and energy injection control, as advantage DC-link (It is the DC voltage that is fed into the inverter and as the name implies, the two sources are linked together with a filter capacitor) and bulk energy storage can be zero;
- Three-phase AC-AC: in this topology, a high current operation is presented;



- DC Fed Energy: low power level can be transfer.

In spite of the fact that those 3 non-resonant converters described before upgrade the resonance frequency with low switching losses, they have high undulation currents in the resonant tank (also called as a resonant circuit is an LC circuit consisting of an L inductor and a capacitor C), which are the consequences of the energy undulation (Jiang, 2017).

For most applications, the non-resonant converters are neither easy to control nor provide stable output. As a result, a resonant inverter with resonance tank is a better solution for near-field WPT system; some of which are:

- Class E: it is an LC tank without DC energy injection; in this topology, high efficiency at high frequency and high-power level is granted. In contrast, a low-power production is presented;
- Class D and DE: in the class D with full bridge a lower switching is given. Also, the combination of DE represents a low switching voltage with a high frequency operation;
- Class EF: On this topology, a switch drain voltage and output current can conduct a better interference performance.

As a summary, on Table 1.6, a small comparison was made.

Table 1.6 Topologies with high resonant WPT (Cem Som, 2019).

Parameter	Number of FETs	Gate Driver requirements	DC supply to Coil RMS Voltage Gain	Differential-Mode configurable	ZVS using resonance	(Load dependent)	Load Current in Passives
Single-Ended Class E	1	Ground Referenced	$\frac{1}{\sqrt{2}} = 0.707$	Yes	Yes	No	Yes
Current Mode Class D	2	Ground Referenced	$\frac{\pi}{\sqrt{2}} = 2.22$	Already	Yes		No
Single-Ended Voltage-Mode Class D	2	Level Shifted	$\frac{\sqrt{2}}{\pi} \cdot G_{Match}$	Yes	No		Yes
Single-Ended ZVS Class D	2	Level Shifted	$\frac{\sqrt{2}}{\pi} = 0.45$	Yes			No

On other topologies, The LC, LLC, and LCL are topologies that can help overcome a high efficiency in the WPT systems for mobility scooters.



Moreover, on the WPT systems with inductance coupling there are 4 main topologies: Serie-Serie (SS)-Serie Parallel (SP), Parallel Serie (PS), Parallel-Parallel (PP).

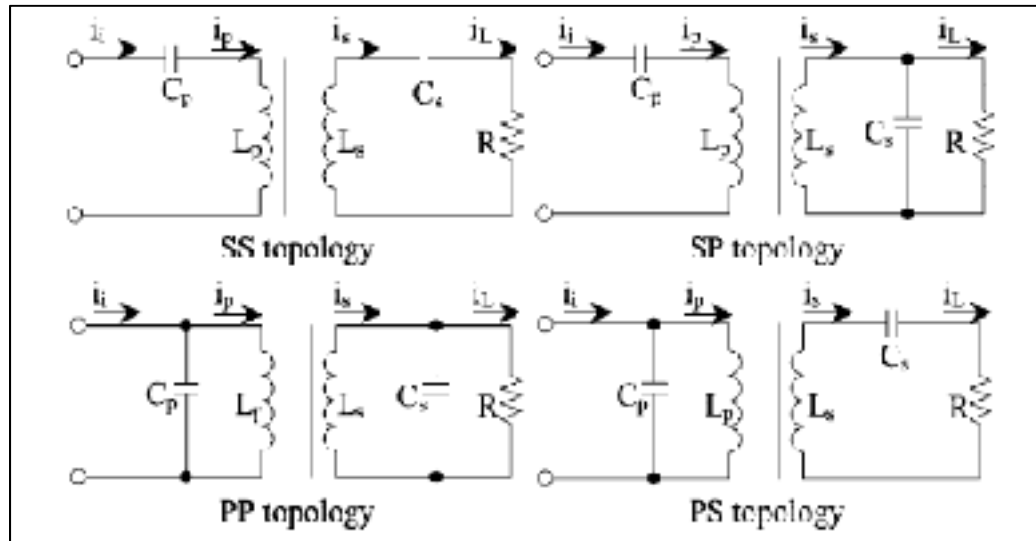


Figure 1.11 WPT Systems Topologies (Sheng-Yang, 2018)

The topology selection depends on the final applications of the system. However, the Serie-Serie topology is a well-known structure as the resonant capacitor value is not affected by the coupling coefficient of the coils, which means the system is neither going to be really affected by the distance between coils nor by the load change.

Series resonance has at least two resonant elements connected in series and cascaded between input and output (Figure 1.12). At the resonant frequency, the impedance of the resonant elements connected in series becomes zero. Therefore, the input-output gain is equal to one. Besides, the SR provides a lowering function of voltage as a buck converter. Parallel resonance is formed by at least one inductor and one capacitor as shown in Figure 1.13 and Figure 1.14. The gain voltage can be very high around the resonant frequency. The Notch resonance is formed either with an LC in parallel and placed in series, or with a LC in series and placed in parallel with the output load.



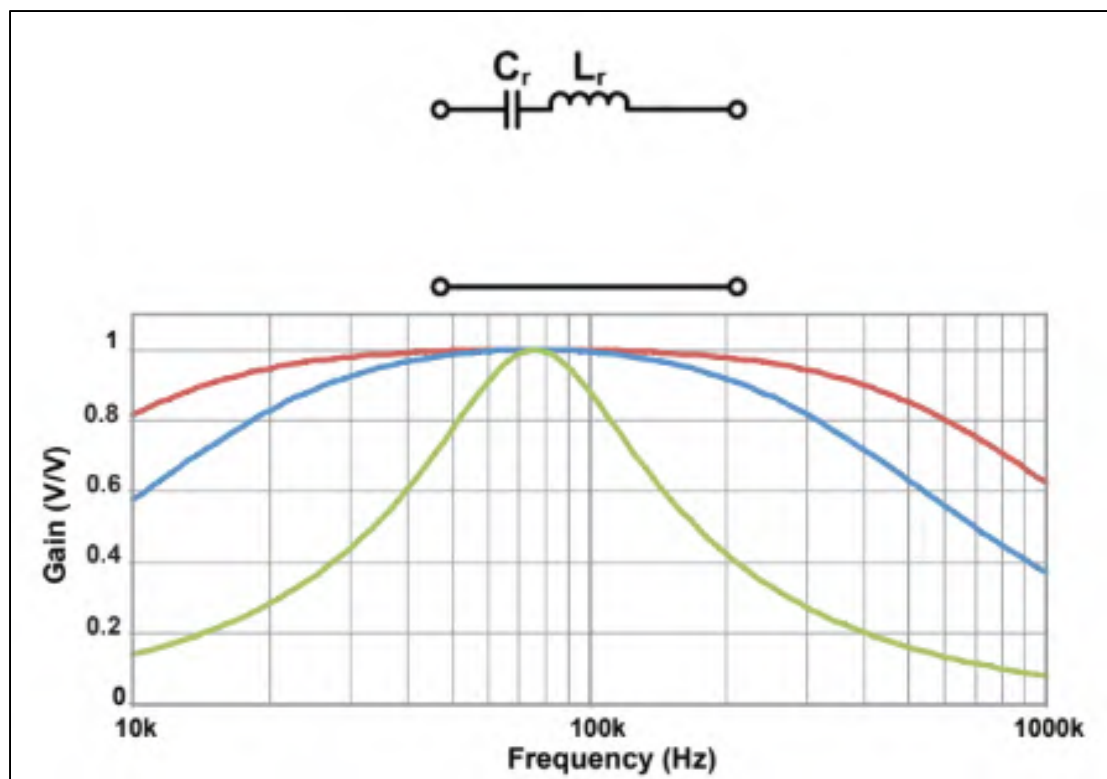


Figure 1.12. Gain curves vs frequency of a CL series resonant topology  
(W. Z. Li, H.; Deng, J.; Li, S.; Mi, C.C, 2016)



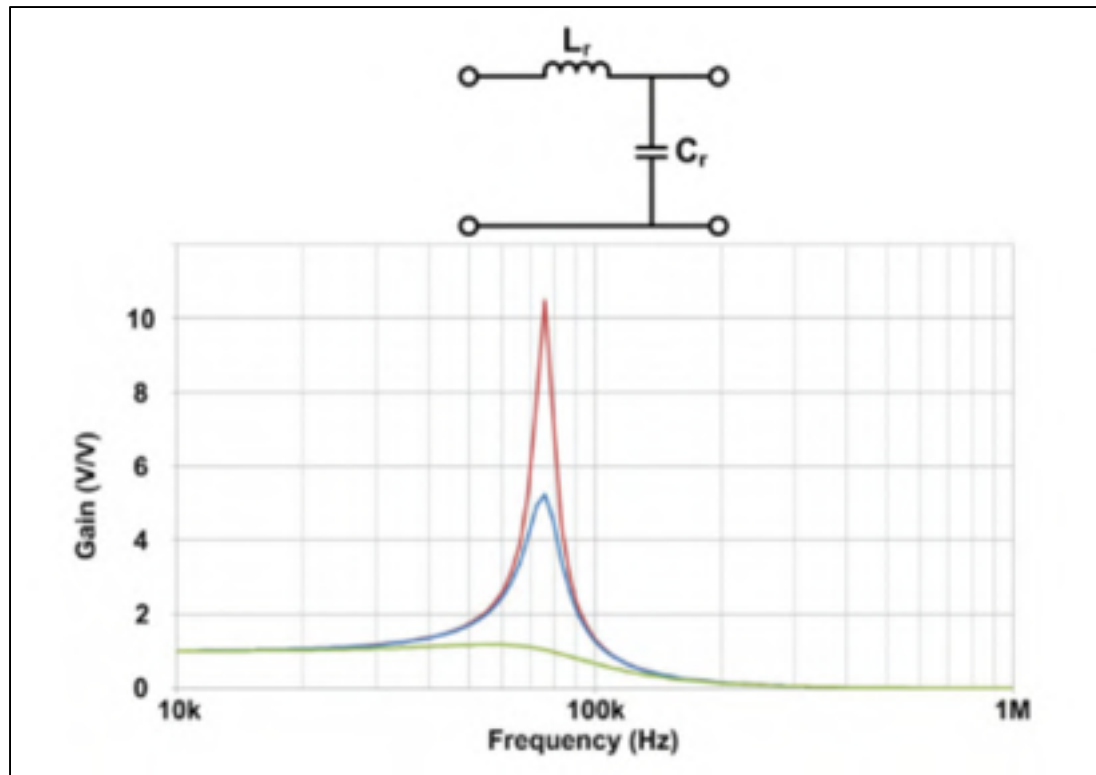


Figure 1.13. Gain curves vs frequency of an LC parallel resonant topology  
(W. Z. Li, H.; Deng, J.; Li, S.; Mi, C.C, 2016)



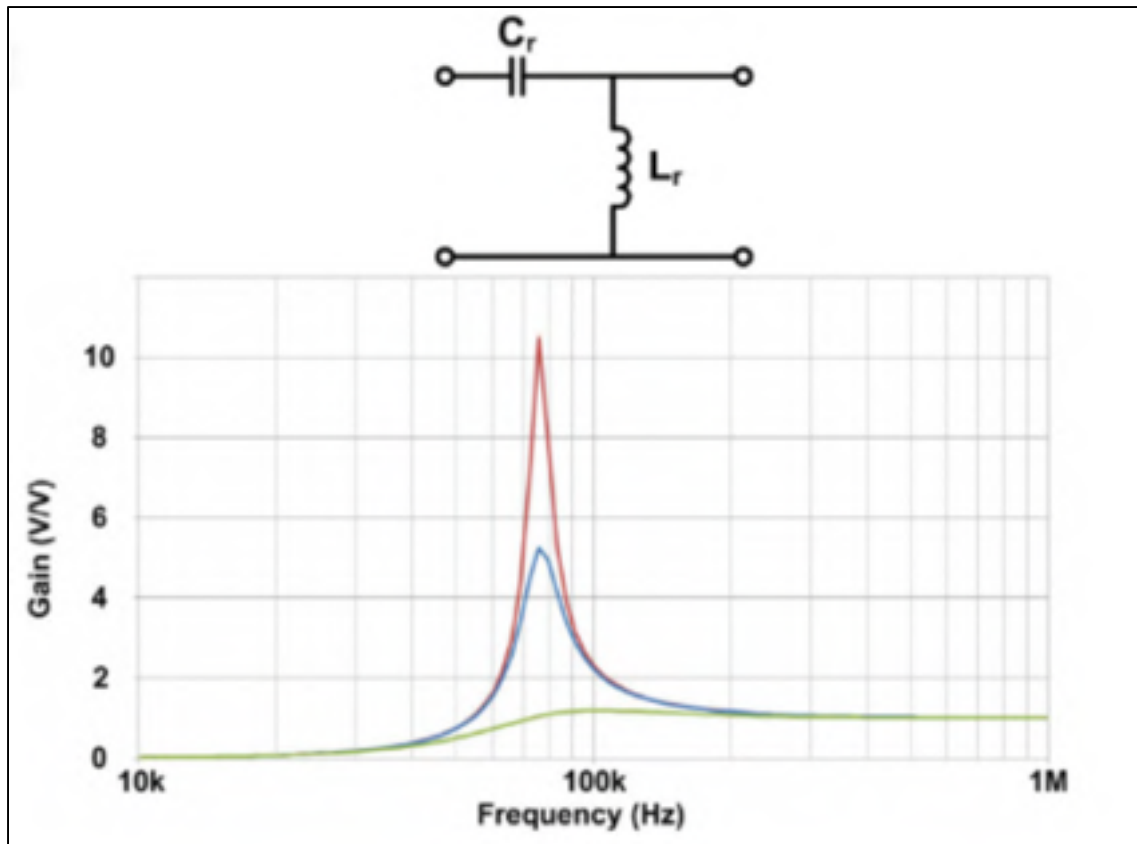


Figure 1.14. Gain values vs frequency of a CL parallel resonant topology  
(W. Z. Li, H.; Deng, J.; Li, S.; Mi, C.C, 2016)

The main advantage of resonant converters is their reduced switching loss via mechanisms known as zero current switching (ZCS) and switching at zero voltage (ZVS). The activation and / or deactivation transitions of the different semiconductor elements of the converter can occur at zero crossings of quasi-sinusoidal waveforms of the resonant converter. This eliminates some of the switching loss mechanisms. Consequently, the switching loss is reduced, and resonant converters can operate at switching frequencies higher than comparable PWM converters. Zero voltages switching can also eliminate some of the sources of electromagnetic interference generated by the converter.



In resonant converters, the power flow can be controlled by the switch to change the frequency of the rectangular voltage, its duty cycle (or both), and by special control schemes, such as phase shift control. An ideal switch is characterized by very high gain and extremely fast switching. Although users often ignore the intricacy of the switching operation, assuming this is not critical to the design overall, the fact is that a good understanding of the factors that affect switching can have a deep effect on system performance, especially frequency, and is therefore of vital interest to the user who needs to optimize its design.

## 1.7 Resonator Structure

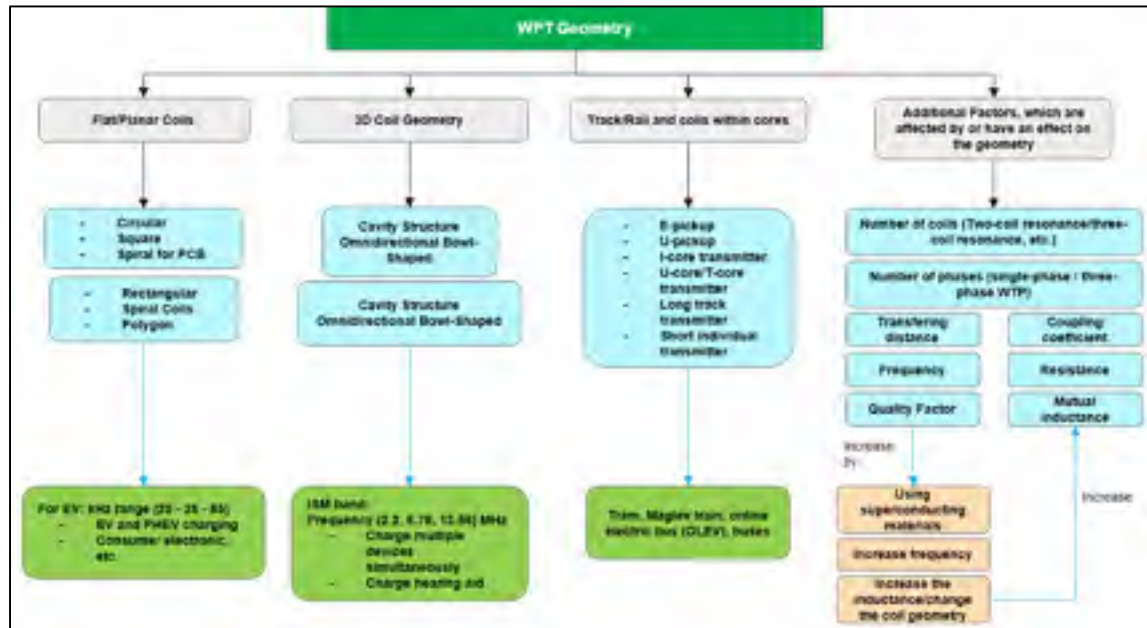


Figure 1.15 Resonant structure geometries for WPT systems (Abou Houran, 2018)

Figure 1.15 shows several research works related to resonator structure geometry such as Flat/Planar Coils, 3D Coil Geometry, Track/Rail and coils within cores and additional factors which are affected by or influence the geometry. The suitable application type is also given for each structure as well as some frequency ranges. Different studies have been investigated based on the shape of the resonator.



Geometries as flat/planar shaped coils can be defined as rectangular-shaped structure (W. Z. Li, H.; Deng, J.; Li, S.; Mi, C.C., 2018), octagonal Resonator (Park, 2016), or a double coil D (DD) (W. W. Zhang, J.C.; Abraham, A.M.; Mi, C.C., 2015). In addition, the defected ground structure (DGS) is presented in (Hekal, 2017). DGS means that a "fault" has been incorporated into the ground plan of a flat microwave circuit: this DGS technique is adopted to improve various parameters of a microwave circuit, such as low gain and narrow bandwidth.

Three-dimensional (3D) geometries are investigated, such as for instance, bowl-shaped transmitter coils (Campi, 2016), which are used for charging hearing aids, cylindrical coils (F. L. Zhang, J.; Mao, Z.; Sun, M., 2012), helix-loop resonators (Yang, 2014), and conical coils. In (Chabalko, 2014), the three-dimensional resonant cavity is presented, which offers a good way of charging multiple devices simultaneously.

Coils' materials are discussed, for example, a receiver coil made of aluminum is used in (Song, 2014). In (Jeong, 2016), the authors proposed a helical-type coil made of superconductors in order to increase the quality factor of the coils. In (Kang, 2017), the authors applied an MCR WPT system (planar textile resonators or PTRs) to wearable consumer electronics by using flexible materials.

Coils with cores are given, such as dipole-type coils (M. K. Kim, H.; Kim, D.; Jeong, Y.; Park, H.H.; Ahn, S, A, 2015), which present a WPT prototype that is capable of transferring the power up to a 5 m distance. To charge vehicles, buses, trams, and trains, long-track transmitter and short-individual tracks are used (M. K. Kim, H.; Kim, D.; Jeong, Y.; Park, H.H.; Ahn, S, 2015). Moreover, E-core and U-core types are discussed (Wang, 2017).

In Electric Vehicle applications due to space limitations, some structures such as the helix, the omnidirectional, the cavity or the conical structure cannot be used, yet the resonators are designed in a spiral or flat coil shape. The advantages of these geometries are that they are printable and easy to implement at low cost. Furthermore, dynamic charging systems are used, which can be divided into two categories according to the track length. The first category is the long track transmitter, which can charge multiple EV at the same time. The long track transmitter system is simple partly due to the low number of components. One example of that kind of system is the Online Electric Vehicle (OLEV) with a maximum charging power up to 100 kW. The downside of this design is its low efficiency of 74%.



The second category is the short-individual transmitter with a length of about 1 m. These systems are arranged in an array to make a tracking lane and each transmitter has a compensation circuit, which can be excited based on the location of the receiver. The benefit of this structure is flexible, but its downside is that it requires many circuit components and converters making it more difficult to implement.

The first reason why the coils used for WPT systems are planar is that the profile area of the coils is small, which means it is easy to integrate with the other parts of the system. The other reason is that when the coils are wider than all the transmission systems, they can reach larger distances and the system becomes more tolerant of alignment errors between transmission and receiver coils. Interestingly, the most common material for the conduction coils is copper, which has excellent conductor thermal and electrical properties also in the WPT systems, this material has a good performance in high frequencies. When an AC current travels through the coil, the current through the coils is not uniform, which costs a reduction of the efficacy area on the conductor; on the inner section fewer current travels, and consequently, the electrical resistance is higher. One of the materials widely used nowadays is Litz wire, which is formed by an enamel copper fiber having the most similar impedance in all the copper threads. Some of those are shown in Figure 1.16.



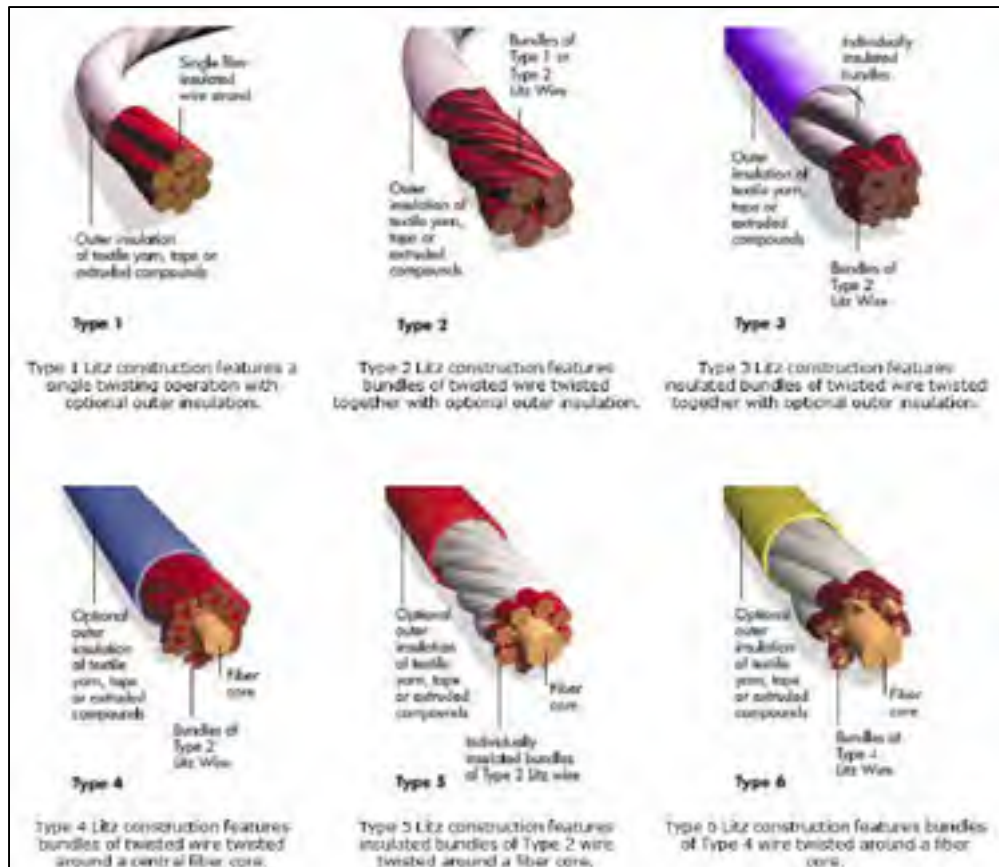


Figure 1.16 Classification of Litz constructions types (technologies, 2018)

## Wireless Power Transfer Coil Selection

For the selection of the coils, two main factors must be considered: the lower and the higher resonant frequency in the wireless power system. A classical inductance topology is shown in Figure 1.17.



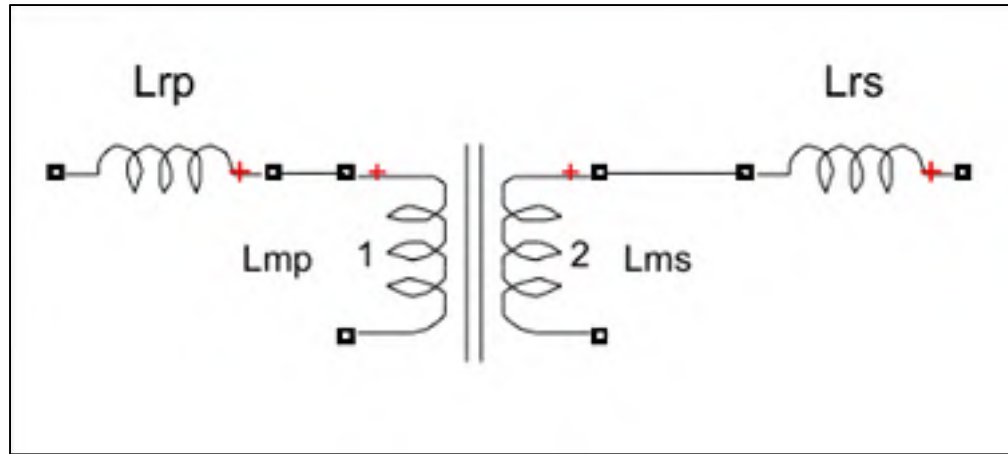


Figure 1.17 Topology of Inductances in a WPT system (Cem Som, 2019)

In the series power transfer systems (Figure 1.17) tuning increases the current; as a result, the impedance is lower, on the other hand, the parallel tuning increases the voltage the impedance. During the design stage, the current and voltage requirements can be found following specific load conditions. Coupling factor and load power variations change the tuned resonance of the coils and this fact must be considered when the amplifier and the rectifier are designed so as to avoid the exchange of highly reactive power in the resonant circuit.

### 1.8 Application: 200 W WPT system with Data Transfer

The described application only allows for wireless transfer on or off. Many applications including the industrial and medical sectors require more control over the signals as well as the possibility to transfer data.



Figure 1.18. 200 WPT development kit (Elektronik, 2019)



This type of transfer includes inductive coupling based on the magnetic flux between two coils. On the transmitter side, there is an oscillator, which works as an inverter feeding a resonant circuit constituted by the transmitter coil. On the receiver side, the system consists of the receiver coil and the rectifier, which generates DC current from high frequency AC input. The oscillator generates an alternating current from the input AC voltage, which then generates an alternating field in the transmitter coil. The energy is transmitted between the transmitter coil and the receiver coil, thanks to counter induction between the two coils according to Faraday's law of induction, and it is then rectified and passed onto the load.

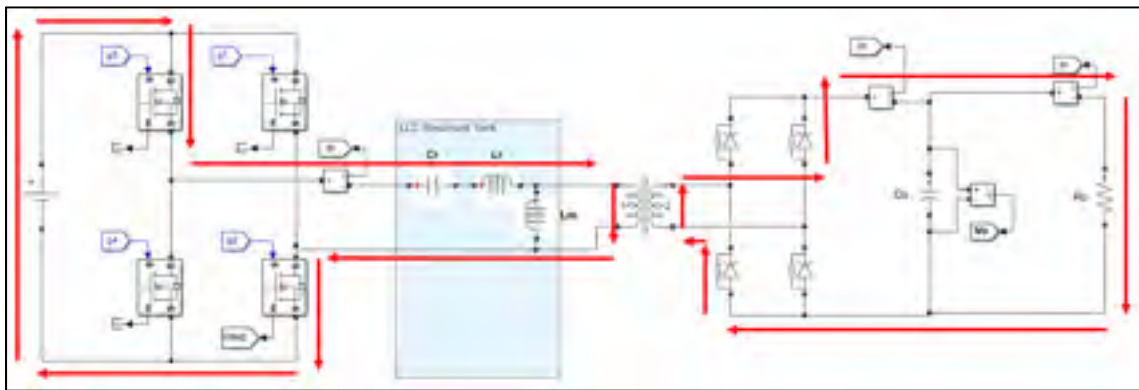


Figure 1.19 Current flow transmitter through the 200W. WPT system

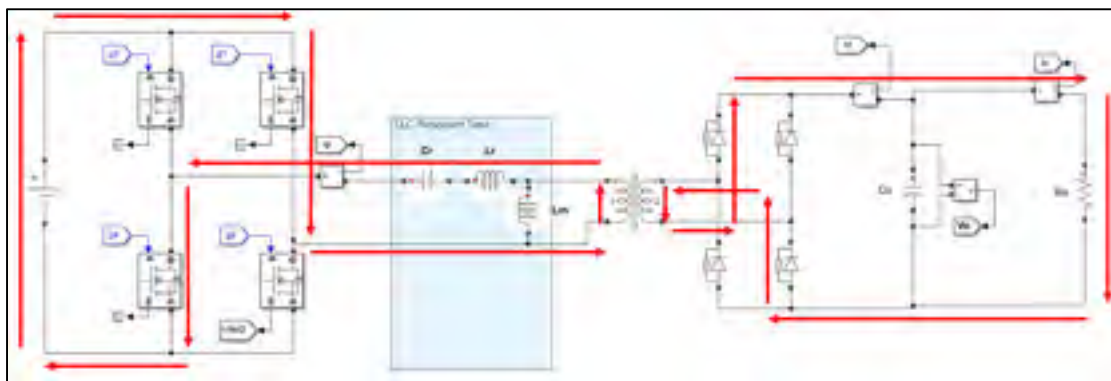


Figure 1.20 Current flow receiver through the 200W. WPT system



The stray flux is a direct outcome of larger distances between transmitting and receiving coils resulting in energy transmission decreases. This can be alleviated by resonant inductive coupling improving the range and the efficiency of the circuit. An LC series resonant circuit can be used, and the resonant frequencies of the oscillating circuit must be tuned. The very high stray inductance is almost completely compensated with capacitors in series with the wireless power transfer. The circuit is not self-oscillating, so the switching frequency is determined by the oscillator and is tuned to the resonant frequency of the series resonant circuit.

Advantages of this concept:

- Large power scale (from 10 W to several 10 kW);
- Good EMC thanks to the sinusoidal aspect of the resonant circuit and rectifier;
- Efficiency over 90% due to zero voltage MOSFET turn-on switching;
- Easy adaptability for many voltages/current uses;
- The output voltage can be higher or lower than the input voltage by adjusting the switching frequency.

## **1.9 Control strategies of the LLC converter topology**

The application of control theory and feedback can eliminate steady-state errors, moderate system sensitivity to parameter changes and disturbances, and modify the gain or phase of the system over the desired frequency range. Moreover, to achieve output voltage regulation any converter must be coupled with a feedback control system.



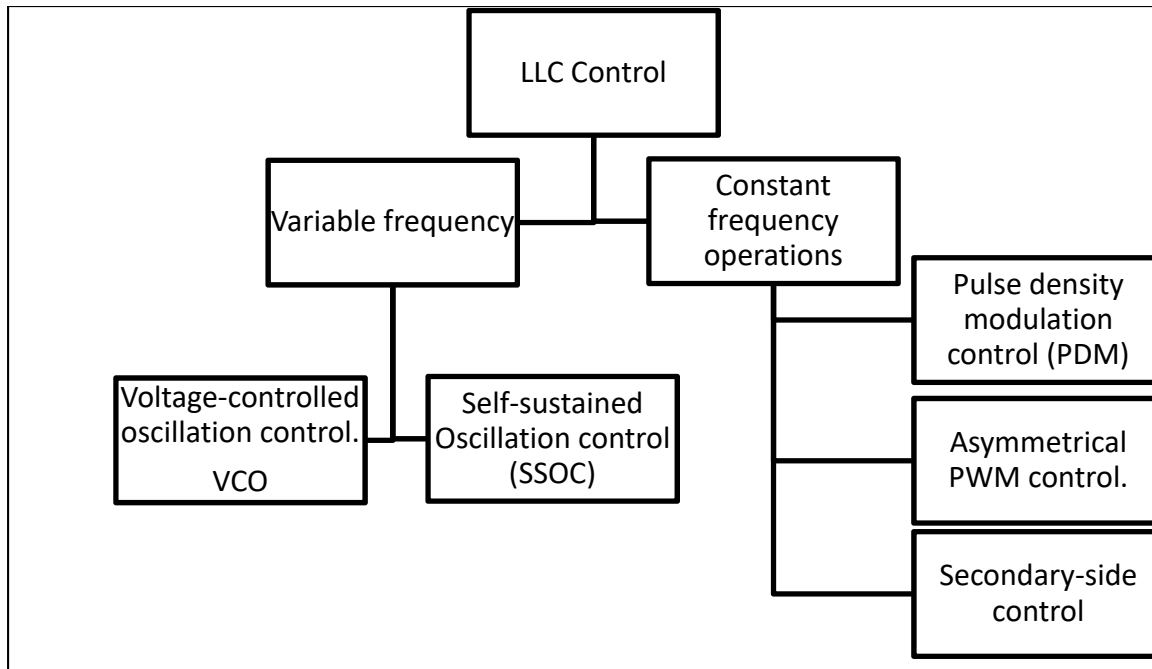


Figure 1.21. Control types in an LLC converter

### 1.9.1 Variable Frequency

For the output voltage regulation, the LLC resonant converter varies its switching frequency to manipulate the voltage gain observed at the output. This type of control requires a gate drive signal that has a constant duty cycle but varying the frequency.

**Voltage controlled oscillation control:** to implement variable frequency control, an actuator that can produce a variable frequency signal is required and can be realized by a voltage-controlled oscillator (VCO). The VCO is defined by an electronic circuit designed to produce an oscillation frequency based on the control voltage and can be implemented on the gates of the primary side of the topology as is shown in Figure 1.22. Besides, the frequency of the gates is varied in contrast to line and load. Changing the impedance of the resonant tank wide-ranging the converter gain change. Complex design in the magnetic components is necessary (F. Musavi, 2013),(S. W. Kang, 2014),(S. Kang, 2016)



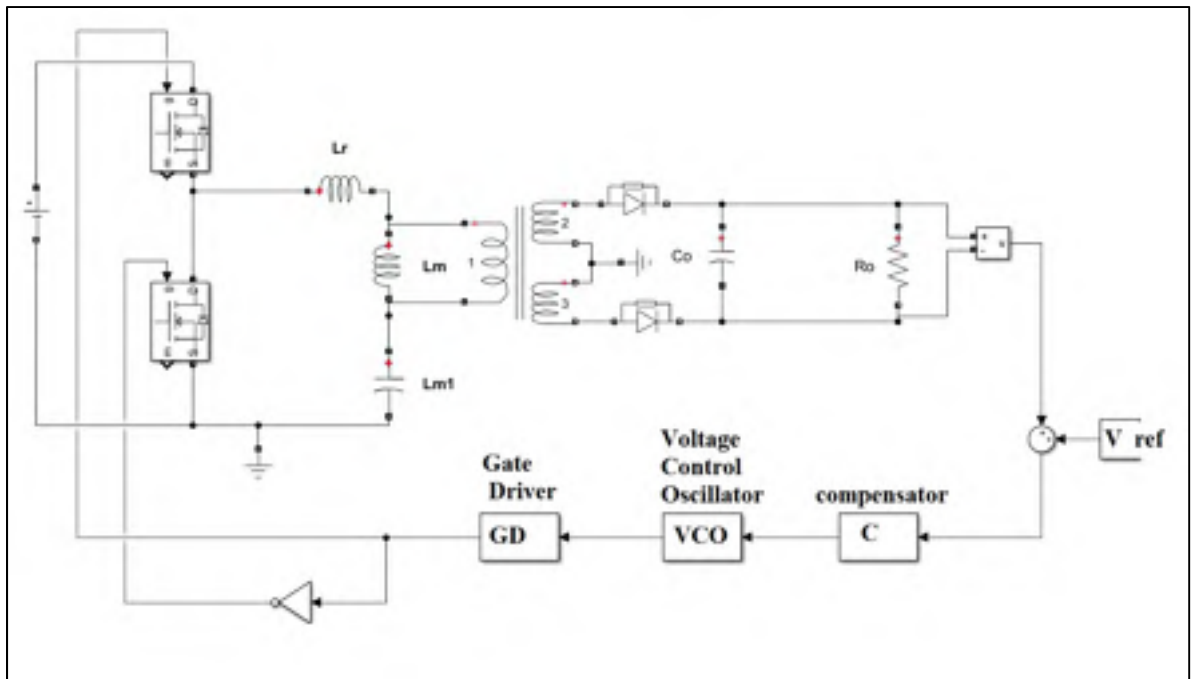


Figure 1.22 Diagram of a voltage-controlled oscillation for an LLC converter

**Self-Sustained Oscillation Control (SSOC):** is used to achieve voltage regulation and high frequency for a wide range of load currents. This type of control allows a minimum power factor angle and consequently a smaller primary current to reduce conduction losses, leading to a better working efficiency. The control diagram is shown in Figure 1.23.(P. Kowstubha, 2014)



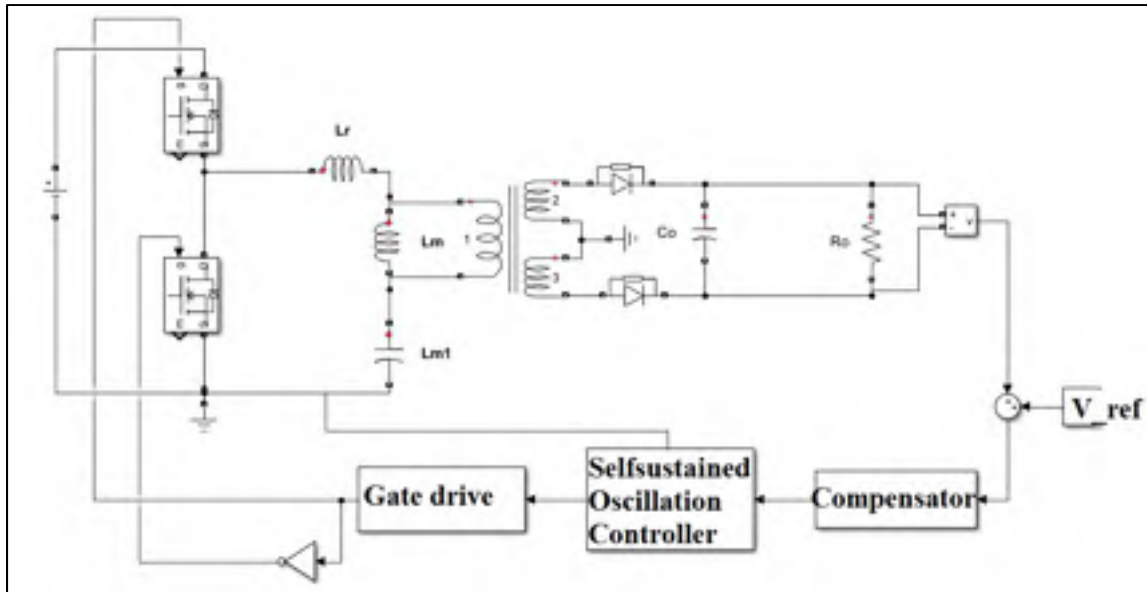


Figure 1.23 23Diagram of Self-Sustained Oscillation Control for an LLC converter

The main objective of the SSOC controller is to control the switching frequency to simultaneously guarantee both output-voltage regulation and ZVS of the converter. To achieve this operation, the SSOC is composed of two control loops: an inner loop and an outer loop. The inner loop adjusts the phase shift or control angle between the resonant current and inverter output voltage to guarantee ZVS under any operating condition. The outer control loop adjusts output voltage according to the reference value, and the control voltage is compared to the sawtooth that is synchronized, with zero-crossing the resonant current to adjust the required phase shift for ZVS. (Jain, 2007a, 2007b; L. Sahaya Senthamil, 2012).

### 1.9.2 Constant Frequency Operations

This type of control is a fixed frequency and modifies the duty cycle of the pulses to regulate the output voltage. **Asymmetrical PWM control:** it can achieve the zero-voltage switching (ZVS) turn-on the power switches of the primary side and to reduce the circulating current loss. Besides, in the turn-off cycle, the ZCS can be achieved by the output diodes. Moreover, for controlling the on and off time in the switches, a constant frequency is delimited. This control improves the magnetic elements. The APWM has shown in Figure 1.24.



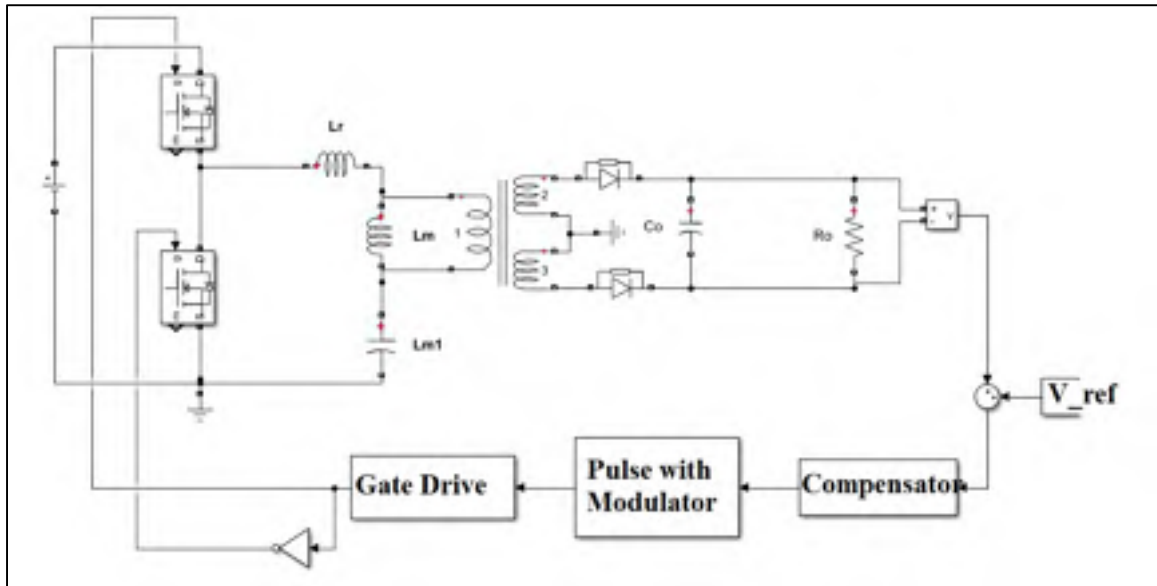


Figure 1.24 Diagram of Asymmetrical PWM control for an LLC converter

Generally, APWM control schemes have the stress with unbalance of the output components and the reverse recovery problem on the secondary side of the transformer. In contrast, the decrease in the duty cycle increases harmonics. (B. Kim, 2012; Nakaoka, 2009; W. Cha, 2016)

**Pulse Density Modulation Control (PDM):** this power control is provided by deleting some of the on-pulses without changing the turn-on the duration of the switch. The output power of the converter decreases as the number of the deleted pulses increases. The PDM is also known as a burst mode control. The output power is controlled; however, the voltage is not the same design as the Asymmetrical PWM, but the PWM block is digital. This control method has the characteristics of voltage stress and high conduction loss. (H. Mizutani, 2013; Oncu, 2017)

**Secondary-side control:** As the name indicates the control is in the secondary side of the transformer; a synchronous rectifier (SR) is used to control the time on of the MOSFET as shown in Figure 1.25. Increasing a filter output selection has led to keeping the ripple low at the output. (H. Wu, 2015; J. Liao, 2011; W. Feng, 2010).(P. Kowstubha, 2014).



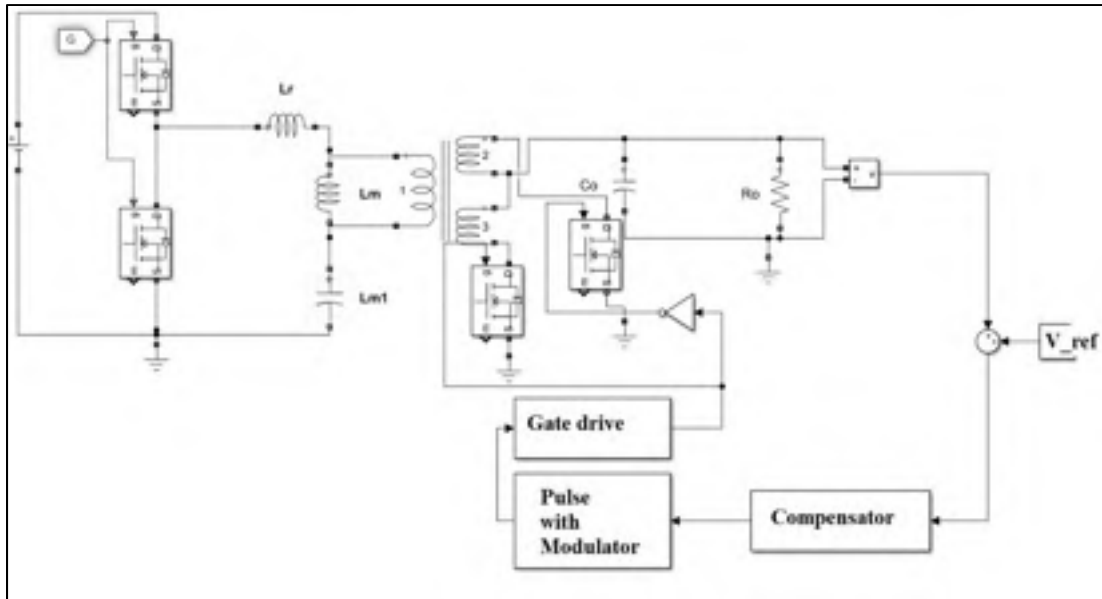


Figure 1.25 Diagram of a modulator pulse control in the secondary side of the LLC converter

The review of the literature shows that the efficient control method is asymmetrical PWM control giving a fixed frequency and load despite giving the option of a simple filter selection. In this chapter, the main uses of micro-mobility vehicles with power wireless systems are listed. Besides, based on market research, the common brands are pride, drive, and merits with the best performance and low price. Moreover, the WPT systems are detailed as far-field and near field. In this research, the near field is going to be used because it is highly efficient, and less radiofrequency is presented for battery charger purposes.

The geometry-shape as a spiral coil planar with Litz material is nowadays used in the WPT systems. The LLC converter is selected because it is a topology that has high efficiency in energy transfer for WPT systems in the near field.



## **CHAPTER 2**

### **ANALYSIS OF THE LLC CIRCUIT TOPOLOGY**

#### **2.1 LLC Circuit Topology**

The LLC type of circuit topology has the following characteristics:

- Easy design for the inverter working as a voltage source in the primary side;
- Output voltage regulation on the whole power output range;
- Three free design steps: voltage gain range between the input and the output, work frequencies interval, quality factor;
- The inductor series in the resonant tank mitigates the peak current on the inverter and on the resonant tank;
- LLCs are generally used in distributed power systems and WPT; this converter has the advantage of zero voltage switching (ZVS) overall operation mode. Besides it can reduce the power losses during the switching and low EMI (electromagnetic Interference) emission as well.

##### **2.1.1 Fundamental characteristics of the LLC resonant converter**

The main circuit components and layout of the LLC are shown in Figure 2.1. The bridge inverter switches are controlled with 50% duty cycle. The frequency control is variable to regulate both the output voltage and current. The LLC topology can be implemented as well in half or full-bridge configuration (Martinelli, 2001).



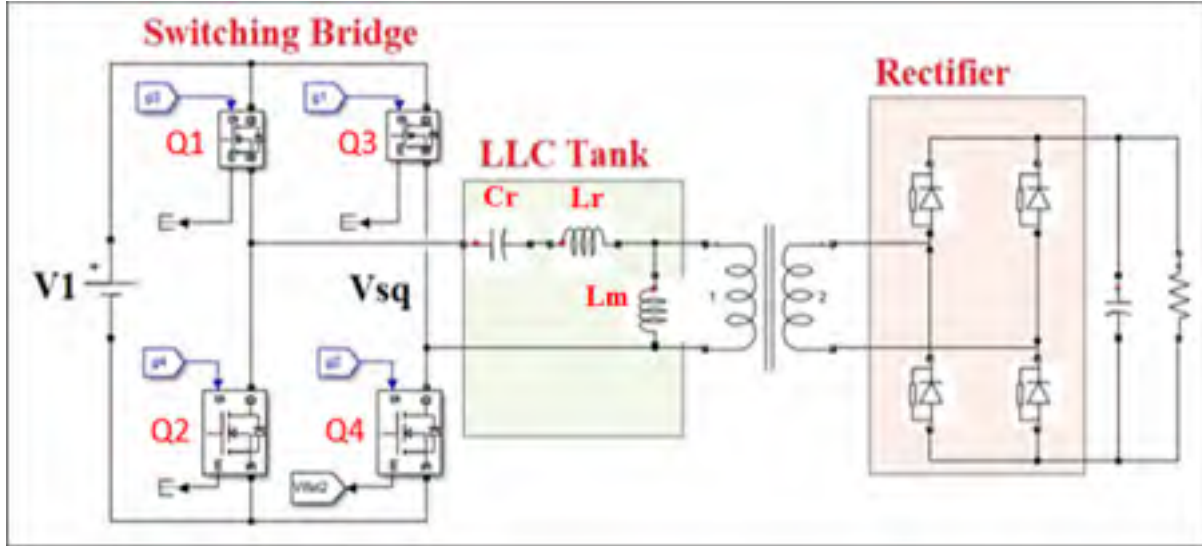


Figure 2.1 LLC Converter topology

As shown in Figure 2.1,  $V_1$  is the DC input voltage and  $V_{sq}$  is the output voltage of the inverter. The switching bridge can be half-bridge as shown in Equation (2.1) or a full-bridge topology as shown in Equation (2.2). Having the topology of the switching bridge the DC bus voltage  $V_1$  is calculated by:

$$V_1 = V_{sq}/2 \text{ (half-bridge)} \quad (2.1)$$

$$V_1 = V_{sq} \text{ (full – bridge)} \quad (2.2)$$

The configuration of the resonant tank consists of the  $C_r$  that is well known as resonant capacitance, the inductances  $L_r$  (resonant inductance) and  $L_m$  (transformer's magnetizing inductance).



## **2.2 Operation of a Full Bridge Resonance Converter**

A typical converter full-bridge converter topology has three main parts. Such as switching bridge, LLC tank, transformer, and rectifier. The switching bridge power switches as Q1, Q2, Q3, and Q4 are generally MOSFETs.

### **2.2.1 Waveforms in the resonant converter**

A sinusoidal current flow is circulating in the resonant circuit, voltage and current signals are phased shifted because the switching frequency of the full bridge is higher than the resonant frequency of the series resonant tuned circuit. There are two operation points, the inductive operation point which the phase shift presents Zero Voltage Switching (ZVS) operation possibly giving the highest efficiency. On the other hand, a capacitive operation point is when the current precedes the voltage, the converter no longer works in ZVS mode, but in Zero Current Switching (ZCS) mode. The ZCS operation leads to higher losses because of the current commutates into the body diodes of the MOSFETs resulting in possible destruction of the MOSFETs.

### **2.2.2 Data transmission between transmitter and receiver**

Two series resonant circuits also enable transmission of data between the transmitter and receiver side and vice versa by modulating the alternating field between the coils.

### **2.2.3 Loosely coupled system**

#### **Transmitter coil tuning**

The transmitter coil can be represented by an inductor. It is typically measured using a Vector Network Analyzer (VNA). Before turning the transmitter coil, it should be placed in its base mode defined as being in its final product state, and without any device or foreign metal object present. Although a shunt capacitor can be connected to the coil that increases the impedance,



this is not typically done as it tends to increase the coil sensitivity to load changes and foreign metal objects.

A series capacitor is used to reduce the impedance. In some instances, a designer may terminate the tuning either inductively or capacitively depending on the use case adjustment requirements.

### **Receiver Coil Tuning**

The receiver coil is like the transmitter coil and can also be represented by an inductor. Before tuning the receiver coil, it should also be placed in its base model without any source or foreign metal object present.

A shunt capacitor can be connected to the coil that increases the impedance. The higher impedance of shunt tuning is helpful to increase the output voltage of the coil but should be used sparingly as it can increase the loading impact and/or excessive undesirable imaginary impedance shifting on the transmitter coil. A series capacitor is used to reduce the impedance.

#### **2.2.4 Closely Coupled System**

The wireless power transfer energy system compliance with the EMC limits is non-trivial. The challenge is that the transmitter and receiver coils behave like a transformer with a poor coupling factor and a very large air gap. This leads to a very high stray electromagnetic field in the vicinity of the coils. EMC measurements have shown that broadband interference can occur in the spectrum of the fundamental wave through to the signal. If the level of interference measured is kept below the limit with some margin, it may be assumed that the limits of the interference field strength are also maintained.

Magnetic field can inductively couple interference currents into neighboring conduction paths. Usually, a greater separation or a ferrite absorber sheet, such as a flexible sintered ferrite sheet is helpful to minimize the interferences



## **2.3 First Harmonic Approximation**

The analysis of the resonant converters' family is complex. The characteristic of reactive elements and switching in the vicinity of resonance frequencies introduces non-linearities that are not represented in an average model of the converter. In the article (Huang, 2011) authors present several methodologies to linearize or obtain a transfer equation of several shapes. Among them, the First Harmonic Approach (FHA) will be presented. One of the most useful methodologies this technique is based on assuming that the current flowing through the circuit is of sinusoidal type. In the LLC tank only circulates the fundamental component of the signal. Since the frequency of switching is always around the series resonance frequency, the fundamental component of the current will be the one that is considered for the calculus of the power transfer in the circuit. In this case, the high-frequency harmonics can be neglected. If the switching frequency is moved away from the resonant frequency, more harmonic components appear that will produce less accuracy. The design process in order to define the ratings of the components is followed by:

1. Representing the square input voltage and current with the fundamental component, ignoring the other harmonic components;
2. Ignoring the effect of the output capacitor, the rectifier, and the dispersion inductance in the secondary of the transformer;
3. Referencing the variables from secondary to primary;
4. Representing the square voltage in the secondary of the transformer referenced to the primary with the fundamental component, ignoring the other components.



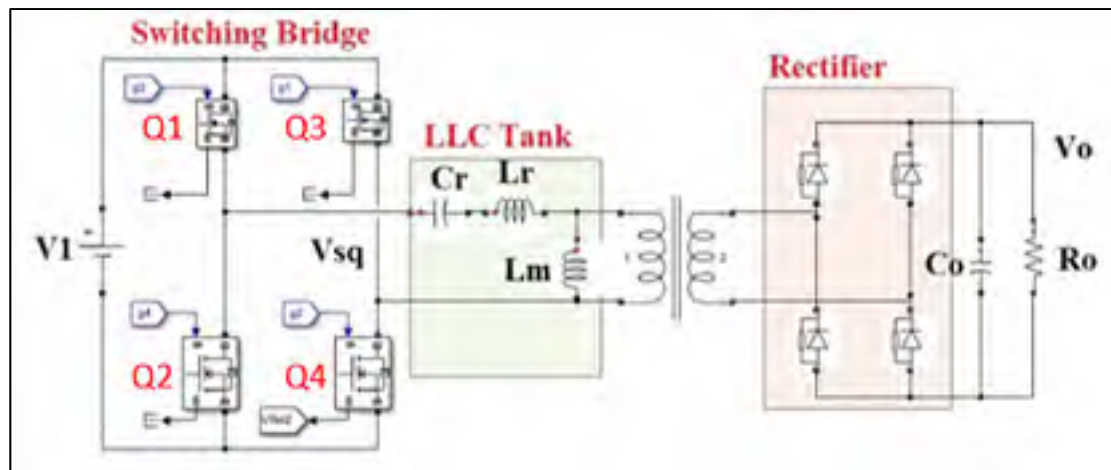


Figure 2.2. A typical configuration of the resonant converter

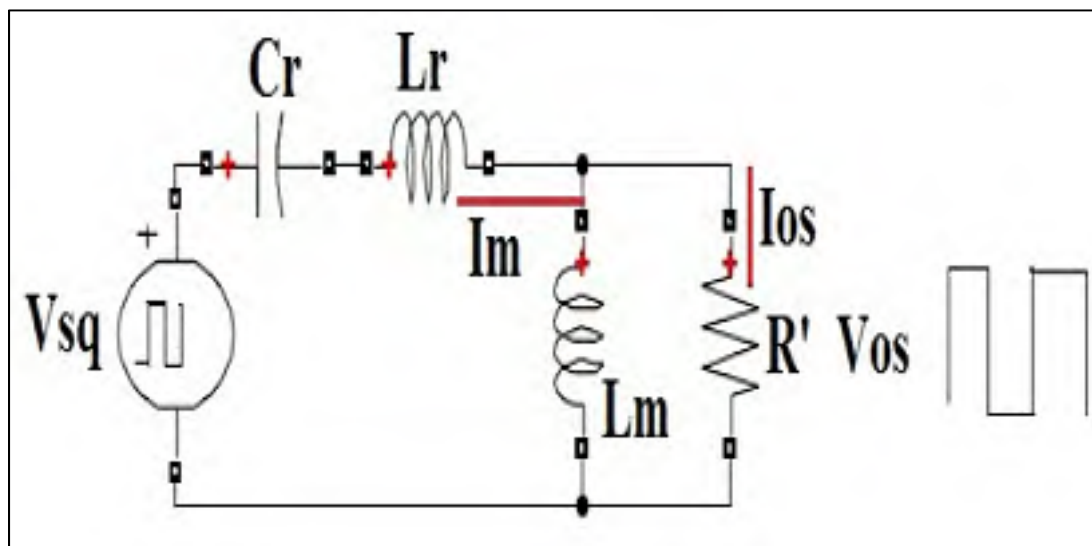


Figure 2.3. Simplified converter circuit squared showing  $V_{os}$  and  $V_s$ . No linear non-sinusoidal circuit



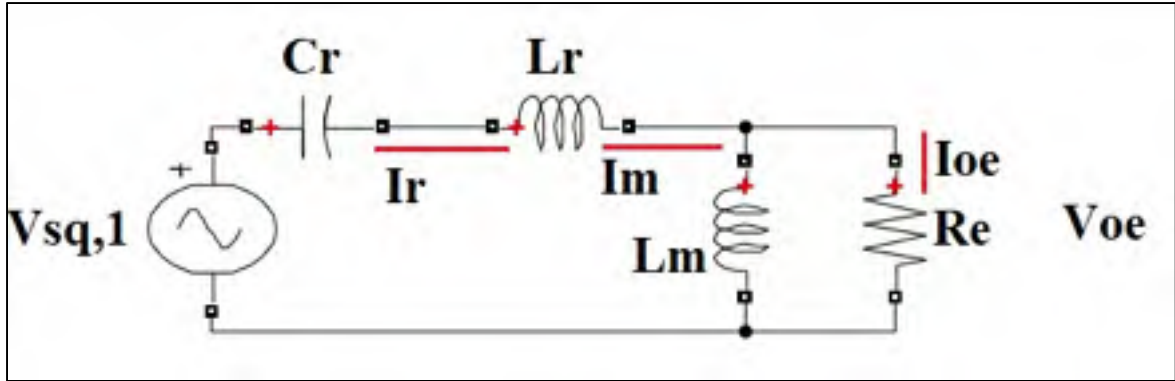


Figure 2.4. Equivalent Circuit of the converter. Linear sinusoidal circuit

Where the circuits elements shown in Figure 2.3, 2.4, 2.5, and 2.6 are defined by:

$V_1$ , is the DC voltage;

$V_{sq}$  is the quadratic output of the full-bridge inverter;

$V_{sq, 1}$  is the fundamental component of the  $V_{sq}$  ;

$V_o$  is the voltage on the load;

$V_{os}$  is the simplified output voltage;

$V_{oe}$  is the fundamental component of the  $V_{os}$  voltage;

$I_o$  is the current on the load R;

$I_{oe}$  is the fundamental component of  $I_o$  ;

$C_r$  is the resonance capacitor in the LLC Tank;

$L_r$  is the resonant Inductor in the LLC tank;

$L_m$  is the transformer's magnetizing inductance;

$N_p$  is the number of turns in the primary coil

$N_s$  is the number of turns in the secondary coil

$f_s$  is the switching frequency.

$f_r$  is the series resonant frequency.

$R'$  is the RLoad from the primary side;

$R_e$  is the equivalent R Load reference of the primary with the FHA simplification;

$Q_1, Q_2, Q_3, Q_4$  Mosfet on the full bridge.



## 2.4 Impedance Calculation

The resonant tank gain can be calculated from the equivalent resonant circuit as shown in Figure 2.5:

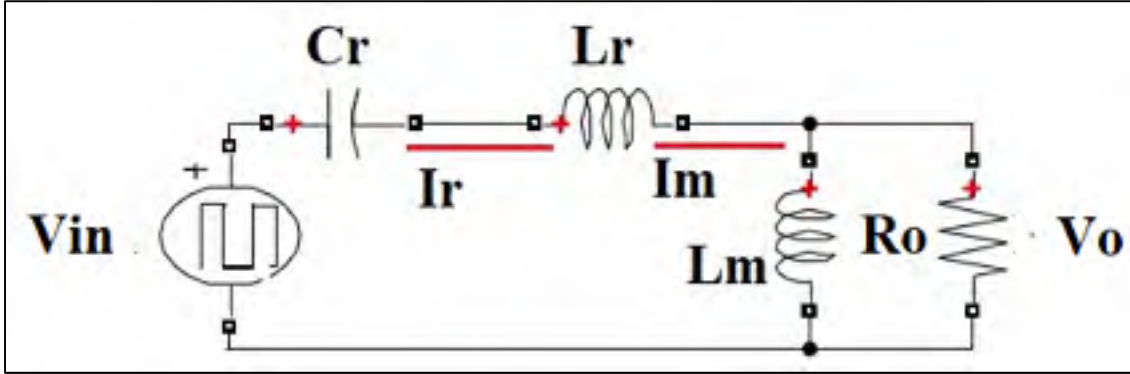


Figure 2.5. Resonant Tank equivalent circuit non-sinusoidal circuit

Which the transfer function  $\frac{V_o(s)}{V_{in}(s)}$  is (detailed are shows in appendix A):

$$K(Q, m, F_x) = \left| \frac{V_o(s)}{V_{in}(s)} \right| = \frac{F_x^2 (m - 1)}{\sqrt{(m * F_x^2 - 1)^2 + F_x^2 * (F_x^2 - 1)^2 * (m - 1)^2 * Q^2}} \quad (2.3)$$

Where:

$$Q = \frac{\sqrt{L_r / C_r}}{R_o} \text{ Quality Factor;}$$

$$R_o = \frac{8}{\pi^2} * \frac{N_p^2}{N_s^2} * R, \text{ Reflected load resistance;}$$

$$F_x = \frac{f_s}{f_r}, \text{ Normalized switching frequency;}$$

$$f_r = \frac{1}{2\pi\sqrt{L_r \cdot C_r}}, \text{ Resonant frequency;}$$

$$m = \frac{L_r + L_m}{L_r}, \text{ Ratio of total primary inductance to resonant inductance.}$$



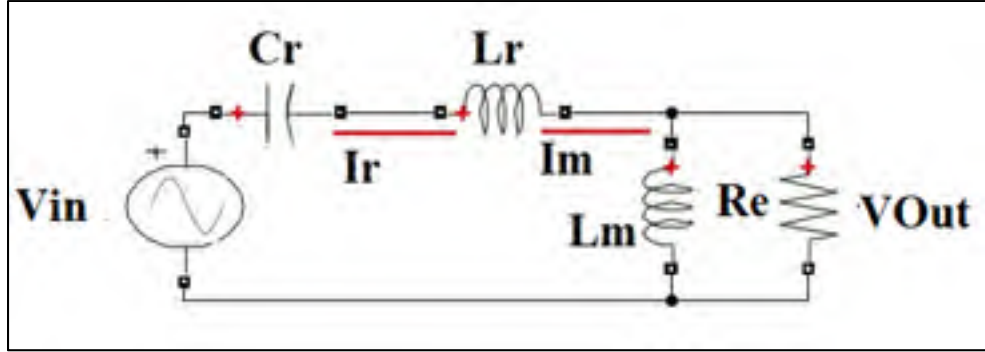


Figure 2.6 Resonant Tank equivalent circuit linear sinusoidal circuit

$$Z(s) = sL_r + \frac{1}{sC_r} + \frac{sL_m R_e}{sL_m + R_e} = \frac{s^3 C_r L_r L_m + s^2 C_r R_e (L_r + L_m) + sL_m + R_e}{s^2 C_r L_m + sC_r R_e} \quad (2.4)$$

After having the impedance of the LLC resonant tank, the two resonant frequencies can be calculated by (2.5) and (2.6). Where  $f_p$  is the total resonant frequency and  $f_r$  is the Series resonant frequency.

$$f_p = \frac{1}{2\pi\sqrt{C_r(L_r + L_m)}} \quad (2.5)$$

$$f_r = \frac{1}{2\pi\sqrt{C_r L_r}} \quad (2.6)$$

#### 2.4.1 Theory of resonant tank operation

The resonant circuit's selective property is defined by the amount of current to be circulated and transferred to the load independence of the resonance circuits impedance (assuming variable frequency control). A series resonance with LC tank converter has the resonance frequency as was shown in Equation (2.5) and (2.6) where  $f_p$  and  $f_r$  were defined as total



resonance and series resonance frequencies. Moreover, the resonant converter  $f_0$  is defined as the resonant frequency depending on the load when the current and voltage input has a zero phase (Lind, 2013).

On the LLC circuit,  $f_0$  value is depending on the load so the frequency could be  $f_p \leq f_0 \leq f_r$ , where; no load  $f_0 = f_p$ . As the load increases,  $f_0$  moves towards  $f_r$ . At a load short circuit  $f_0 = f_r$ .

According to this description, there are three operation regions as shown in Figure 2.7.

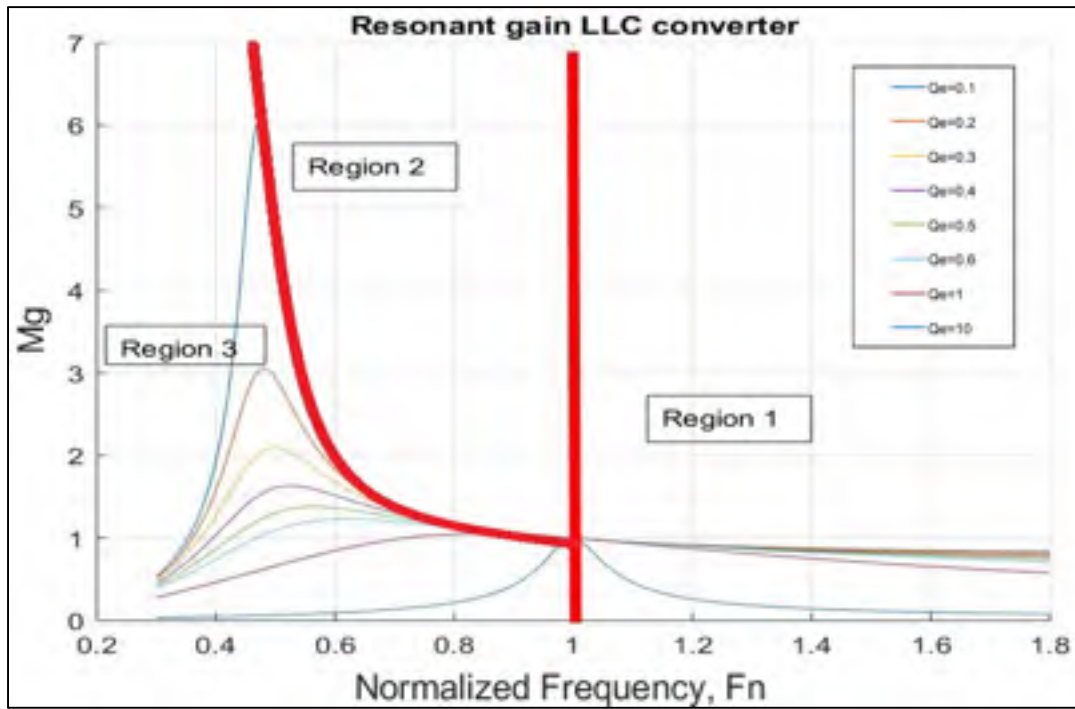


Figure 2.7. LLC Regions (Appendix A, Solving equation 2.5 varying  $Q_e$ ).

As shown in Figure. 2.7, on Region 1,  $f_0 \geq f_r$  the tank impedance is inductive. In Region 2 also,  $f_0 \geq f_p$  and  $f_0 \leq f_r$ , the impedance is inductive. In Region 3,  $f_0 \leq f_p$ , the impedance is capacitive and if  $f_0 = f_r$  the impedance in the resonant tank is resistive. The switching frequency  $f_0$  improved the impedance of the resonant tank. Regions 1 and 2 are defined by zero voltage switching, in this case, the technique of soft switching can be applied, and this



area is known as an inductive. On the other hand, region 3 is capacitive and is well-known as zero current switchings.

In Figure 2.8, the operation zones are described and are going to be explained thereafter:

### **Operation at Resonance (at $f_0$ )**

In this mode, the resonant tank is working at the series resonance frequency, it is the optimal operating point giving the best efficiency of the system for  $f_0 = f_r$ . When Q1 turns off, the resonant current decrease until the value of magnetizing current and there is no more power transferred. Slight delay for the Q2 switch allows the circuit to achieve ZVS on the primary side and soft commutation on the secondary side.

### **Operation Below Resonance ( $f_0 < f_r$ )**

The ZVS can still be obtained by the primary side of this operation region, also soft commutation mode in the rectifier in the secondary side can be obtained, but if the resonance frequency becomes too low it generates switching losses and several associated issues.

### **Operation Above Resonance ( $f_0 > f_r$ )**

At this stage, a small circulating current is presented on the primary side, reducing current losses. On the secondary side, the diodes are not in soft commutation but the ZVS can still be present on the primary side. This method can cause an increase in the frequency under light load conditions.



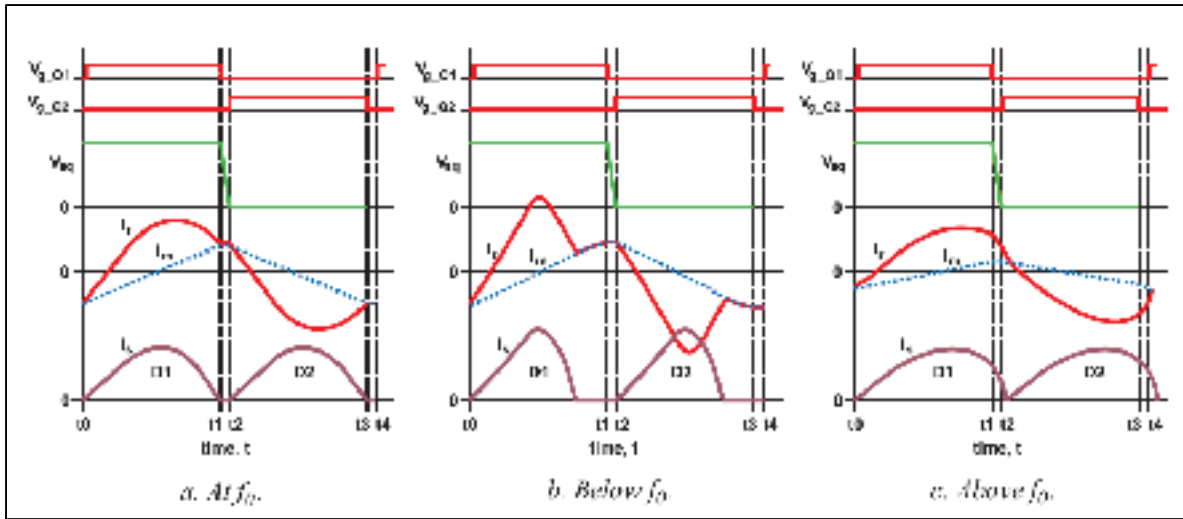
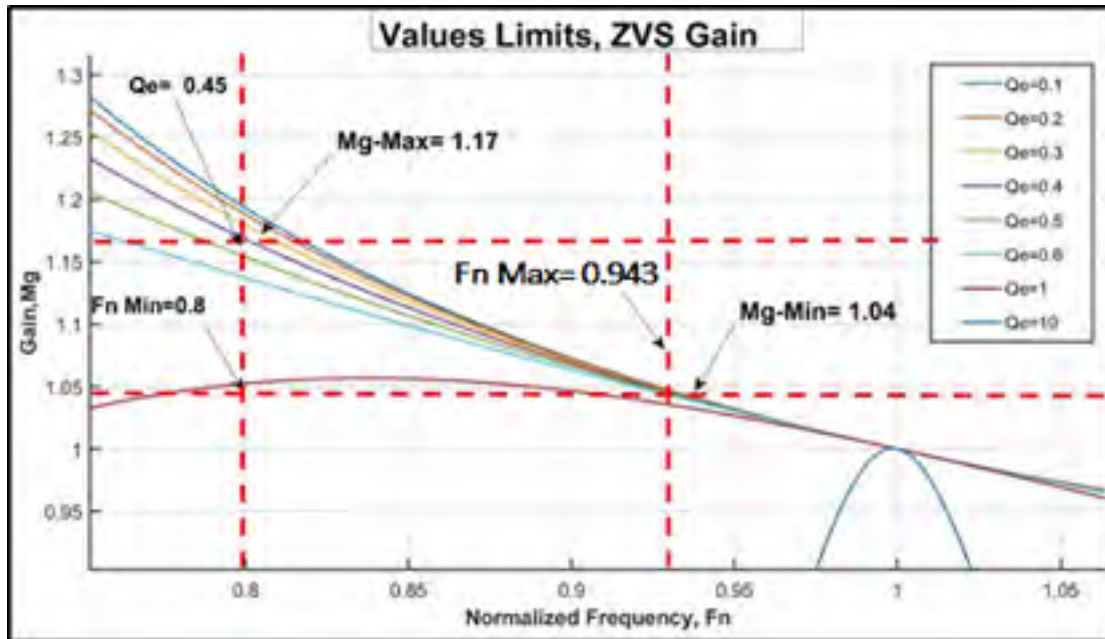


Figure 2.8. LLC Operation (Huang, 2011)

To sum up, the best performance for the resonant tank can be achieved in the vicinity area, which consists of a loose designation between  $M_{g\_min}$ ,  $M_{g\_max}$ ,  $F_{n\_min}$ ,  $F_{n\_max}$  as shown in Figure 2.9.

Figure 2.9. ZVS Gain for different  $Q_e$



## 2.5 Transfer Function

The LLC resonant converter regulates the output voltage by varying the switching frequency of semiconductors, which has an immediate influence on circuit impedance. With this action, the impedance of the resonant tank varies causing variation in the output voltage. A mathematical method is described in order to calculate the relation between the output voltage and switching frequency.

To analyze the stability of the system a Bode diagram was made. Where the magnitude and phase response are displayed. The phase plot is usually in degrees (deg) and the magnitude is in decibels (dB) as shown in Figure 2.10.

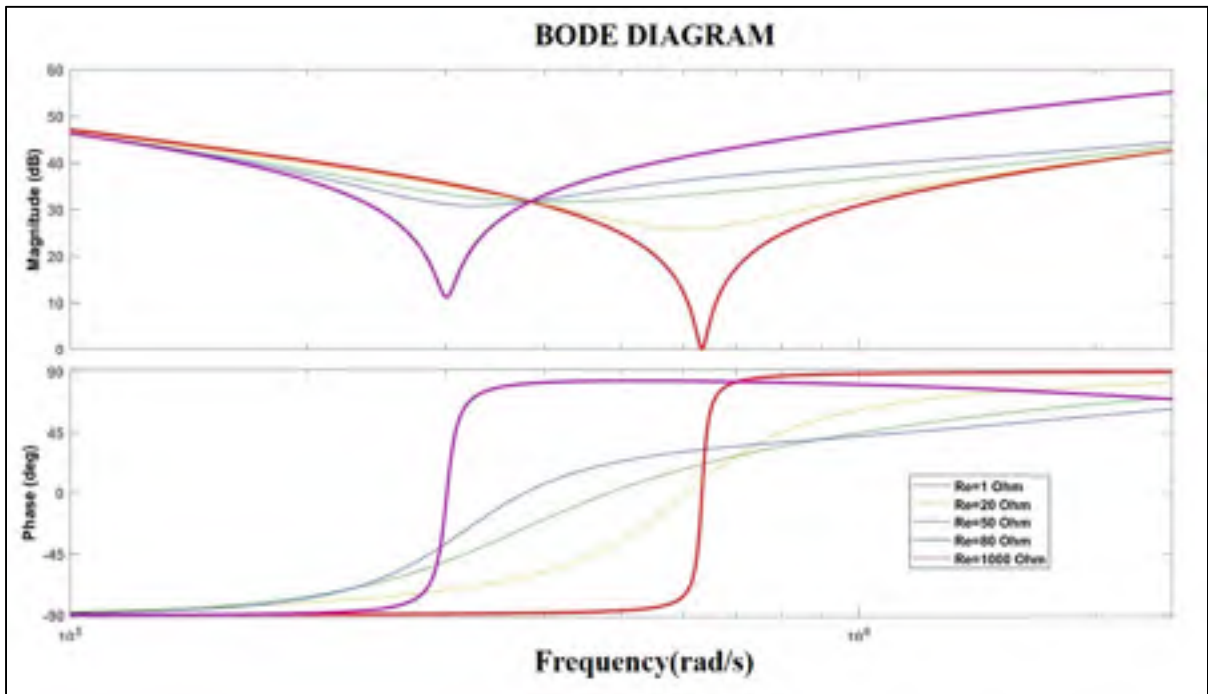


Figure 2.10. Bode diagram of the LLC Tank impedance  
( $L_m = 200\mu H$ ,  $L_r = 58\mu H$ ,  $C_r = 43\text{ nF}$ )



The amplitude of the impedance is calculated as follows:

$$M = \left| \frac{ZL_m || R_e}{ZC_r + ZL_r + (ZL_m || R_e)} \right| \quad (2.7)$$

A transfer function independent (2.11) on the specific values of the capacitor and inductors is developed for generalization purposes (Appendix B).

The following dimensionless parameters of M are defined:

$$M = \left| \frac{L_n f_n^2}{[(L_n + 1)f_n^2 - 1] + j[(f_n^2 - 1)f_n Q_e L_n]} \right| \quad (2.8)$$

As is shown in (2.8), the M(gain) is defined by the resonance frequency of the tank  $f_n$ , the relation between the inductors  $L_n$ , and the quality factor  $Q_e$ .

In Figure 2.11, the design process (Flow Chart) for the resonant tank is detailed. As a first step, the relation between the input and the output voltage is defined, then the max and min gain of the tank were found using the curves of  $Q_e$ . The value of the  $L_n$  is selected in order to approach the design requirements. Then, the resonant capacitor and inductors are calculated. Following this chart will simplify figuring out the specific details of the LLC converter.



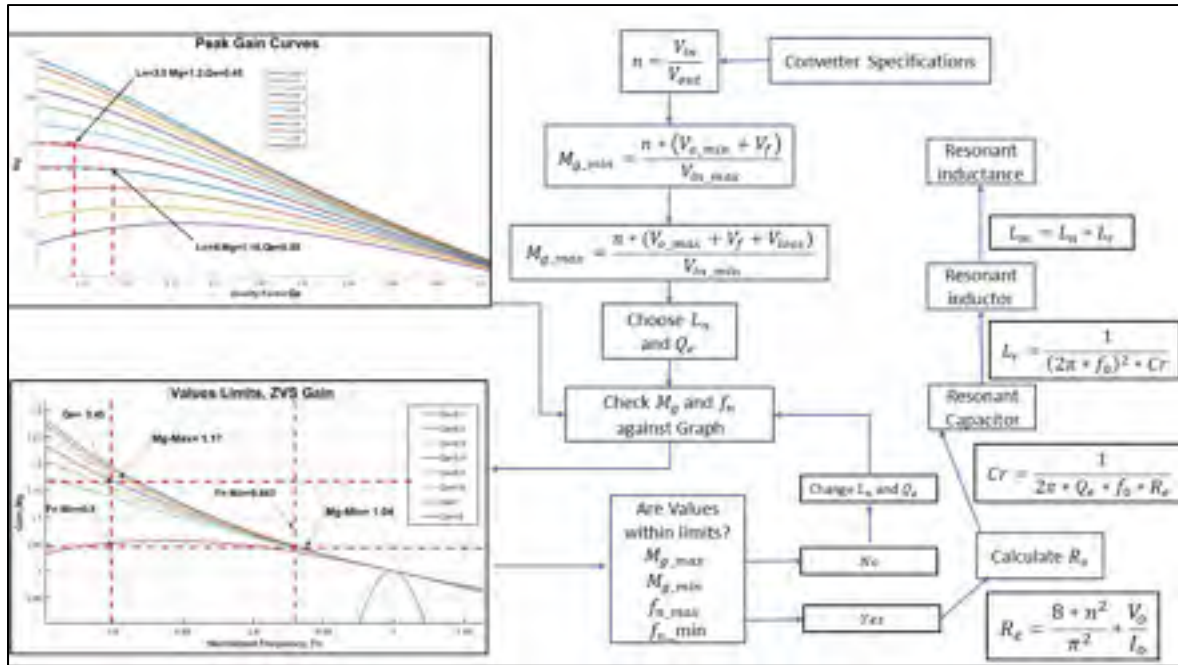


Figure 2.11. Converter Specifications step-by-step design and circuit parameter selections (Huang, 2011)

this project, the design specifications are presented in Table 2.1 , where the input voltage from the grid and the output voltage is defined by the battery type, which in this application is a 12 V-12A type of energy storage device . After doing some calculations with the converter specifications and considering the electronic devices and components that can be found in the GREPCI laboratory, a resonant frequency of 100 kHz was selected.

Table 2.1 Design Specification  
of the LLC converter

Electrical Specifications	
Input Voltage	120V
Rated output power	144 W
Rated Output Current	12 A
Output Voltage peak to peak ripple	12 V
Switching Frequency	100 kHz



## 2.6 Design and simulation of simplified circuit using MATLAB

The converter design specifications are presented and followed from Table 2.1, shall give the following steps to:

- 1) Determine the Transformer Turns ratio (n):

$$\frac{V_{in}}{V_{out}} = \frac{120}{12} = 10 \quad (2.9)$$

- 2) Determine the  $M_{g\_min}$  and  $M_{g\_max}$  :

$$M_{g\_min} = \frac{n * (V_{o\_min} + V_f)}{V_{in\_max}} \quad (2.10)$$

$$M_{g\_min} = \frac{10 * (12V(1 - 1\%) + 0.7V)}{120} = 1.04V$$

$$V_{loss} = \frac{\frac{144W}{92\%} * 8\%}{12A} = 1.04V \quad (2.11)$$

$$M_{g\_max} = \frac{n * (V_{o\_max} + V_f + V_{loss})}{V_{in\_min}} \quad (2.12)$$

$$M_{g\_max} = \frac{10 * (12 * (1 + 1\%) + -0.7V + 1.04V)}{117V} = 1.18V$$

- 3) Selection of  $L_n$  and  $Q_e$  :

From the Figure 2.12  $L_n$  Curves.  $L_n$  and  $Q_e$  were selected as  $L_n = 3.5$  and  $Q_e = 0.45$ .



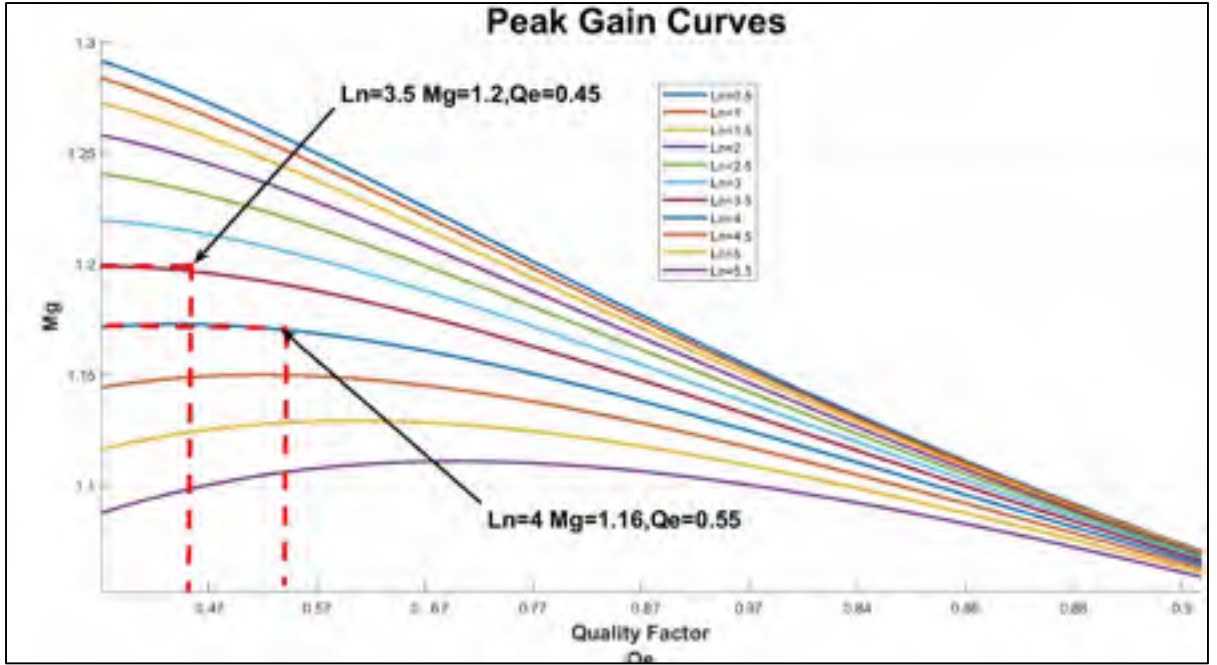


Figure 2.12 Voltage-gain function  $M_g$  with different values of  $L_n$ .

- 4) Determining the equivalent load resistance  $R_e$  :

$$R_e = \frac{8 * n^2}{\pi^2} * \frac{V_o}{I_o} \quad (2.13)$$

$$R_e = \frac{8 * (10)^2}{\pi^2} * \frac{12V}{12A} = 81\Omega$$

At 110% overload :

$$R_e = \frac{8 * (10)^2}{\pi^2} * \frac{12V}{12A * 110\%} = 73 \quad (2.14)$$

- 5) Design of resonant circuit parameters for nominal frequency  $f_0 = 100$  kHz.

$$C_r = \frac{1}{2\pi * Q_e * f_0 * R_e}$$

$$C_r = \frac{1}{2\pi * 0.45 * 100kHz * 81\Omega} = 43nF \quad (2.15)$$



$$L_r = \frac{1}{(2\pi * f_0)^2 * Cr}$$

$$L_r = \frac{1}{(2\pi * 100kHz)^2 * 43nF} = 58\mu H \quad (2.16)$$

$$L_m = L_n * L_r$$

$$L_m = 3.5 * 58 = 200\mu H \quad (2.17)$$

6) determine the primary-side currents.

The primary-side RMS load current with 110% overload:

$$I_{oe} = \frac{\pi}{2\sqrt{2}} * \frac{I_o}{n}$$

$$I_{oe} = 1.11 * \frac{12A * 110\%}{10} = 1.46A \quad (2.18)$$

The RMS magnetizing current ( $I_m$ ):

$$I_m = 0.901 * \frac{n * V_o}{w * L_m}$$

$$I_m = 0.901 * \frac{10 * 12V}{2\pi * 100kHz * 200\mu F} = 0.86A \quad (2.19)$$

The resonant circuits current  $I_r$  :

$$I_r = \sqrt{(I_m)^2 + (I_{oe})^2}$$

$$I_r = \sqrt{(0.86)^2 + (1.46)^2} = 1.69A \quad (2.20)$$



Secondary side currents :

$$I_{oe\_s} = n * I_{oe} = 10 * 1.46A = 14.6A \quad (2.21)$$

The resonant capacitor must have a minimum specification of 1.69A at 100 kHz.

The diodes' voltage rating is defined by (2.22):

$$\begin{aligned} V_{DB} &= \frac{V_{in\_max}/2}{n} * 2 \\ V_{DB} &= \frac{120/2}{10} * 2 = 12V \end{aligned} \quad (2.22)$$

The Diode's current rating is computed as (2.23):

$$\begin{aligned} I_{sav} &= \frac{\sqrt{2} * I_{oe\_s}}{\pi} \\ I_{sav} &= \frac{\sqrt{2} * 14.6A}{\pi} = 7A \end{aligned} \quad (2.23)$$

### **Simulation in MATLAB:**

The model (Figure 2.13) was simulated with the following parameters:

$(L_m = 200\mu H, L_r = 58\mu H, C_r = 43nF, \text{ and } R_e = 81\Omega)$ .



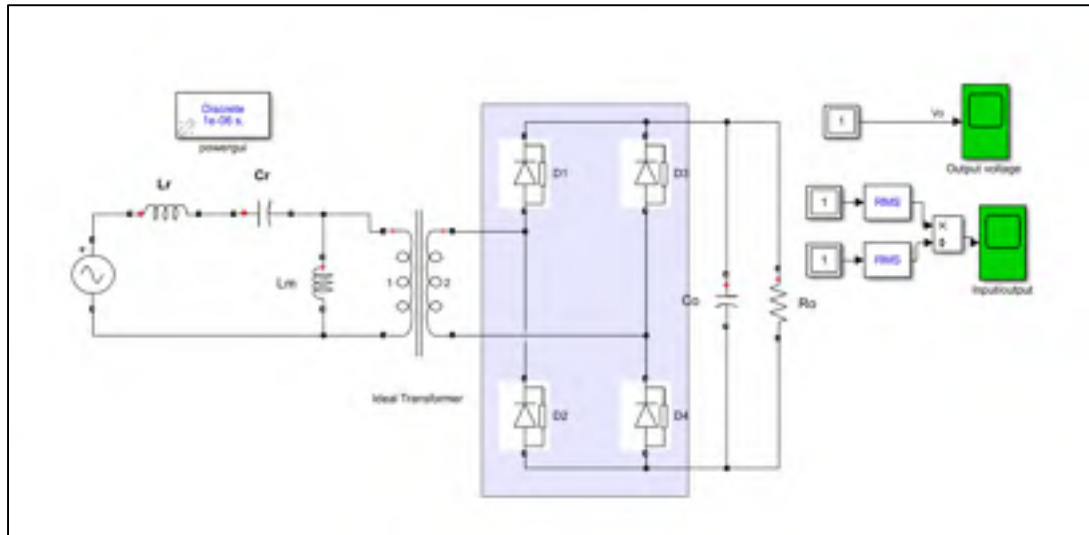


Figure 2.13. Simplified circuit of the LLC converter

As shown in Figure 2.14, the output voltage is 12 V as is desired for the LLC.

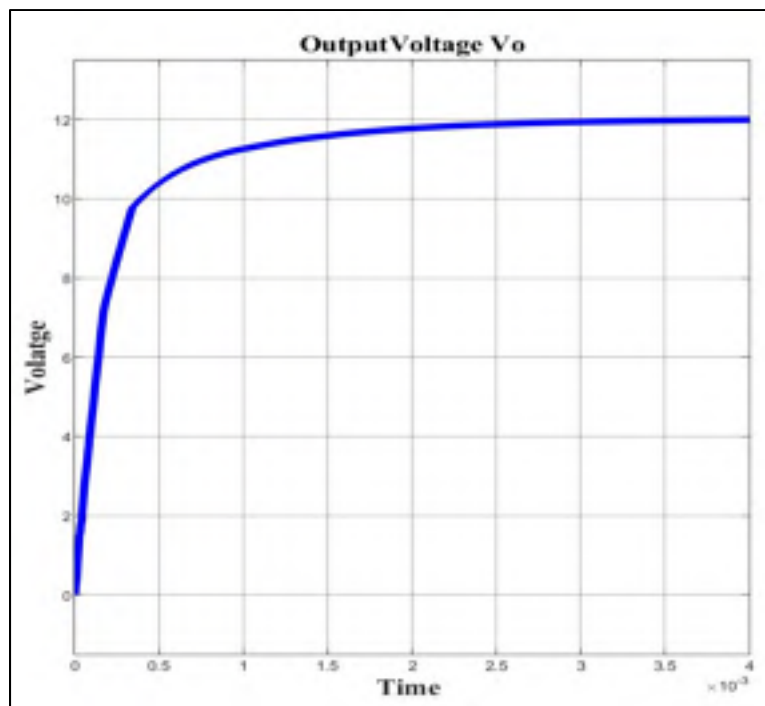


Figure 2.14. Output voltage from the LLC converter



Simulation of the ZVS:

To reduce the switching losses under high-frequency conditions, the switch should operate in the ZVS region. In a design of a series resonant converter, one of the most desirable characteristics is having the best efficiency in the system. In order to achieve that, the switching losses can be reduced by ensuring that the primary side must be in the ZVS area.

Areas showing ZVS and ZCS are presented in Figure 2.15 where:  $L_m = 200\mu H$ ,  $L_r = 58\mu H$ ,  $C_r = 43nF$ ,  $R_e = 81\Omega$ .

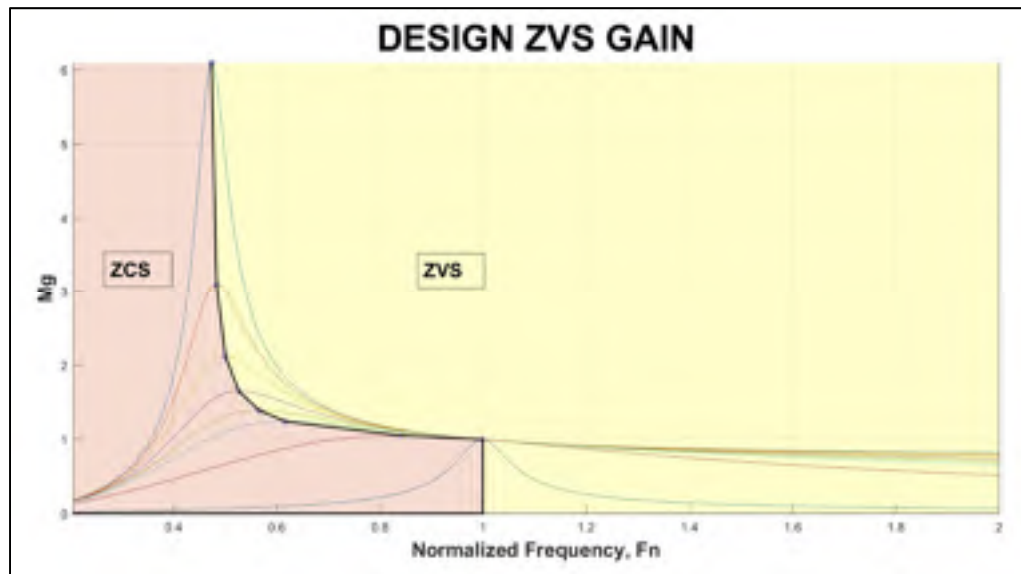


Figure 2.15. Areas showing ZVS and ZCS converter operation.

Now considering the  $Q_e$  and  $L_n$  selection in ZVS operation range, the gain-peak is obtained as shown in Figure 2.16.



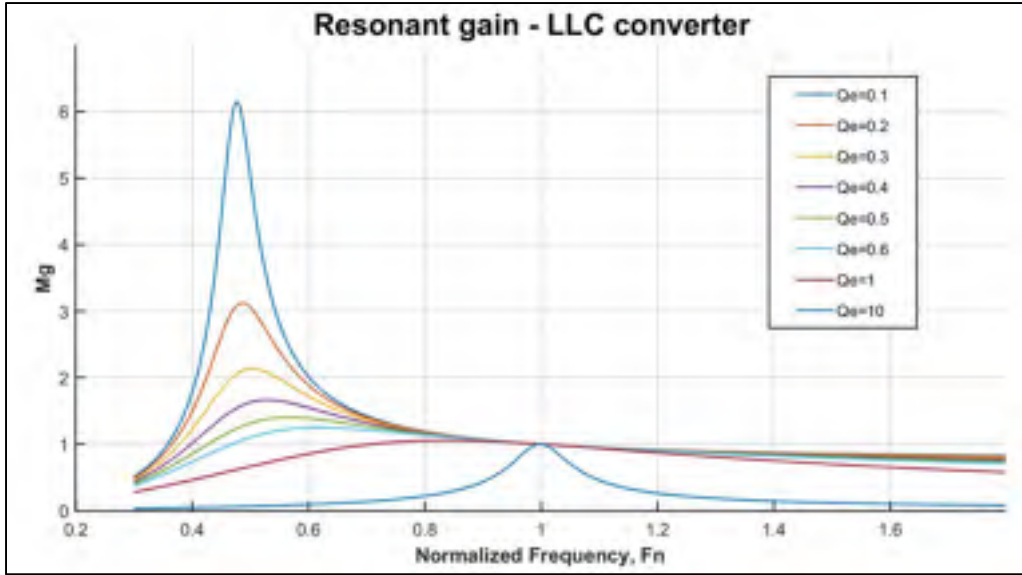


Figure 2.16. Peak-gain curves in MATLAB

In this chapter, an analysis of the LLC converter was detailed, this topology is generally used in distributed power systems. Besides, the main advantage of resonant converters is their reduced switching through zero current switchings (ZCS) and switching at zero voltage (ZVS) that were explained. A step-by-step procedure for the design of an LLC converter was followed where the design specification is selected for a battery charger of 12V, 12A at 100 kHz. After doing the calculation of the passive elements, a Matlab simulation was made in Simulink in order to verify the design. Having the LLC tank design with the values of  $L_m = 200\mu H$ ,  $L_r = 58\mu H$ ,  $C_r = 43nF$ ,  $R_e = 81\Omega$  and a Maximum current of  $I_r = 1.69A$  on the primary and  $I_{oe_s} = 14.6A$  on the secondary the design of the coils are the next steps to follow.



## CHAPTER 3

### DESIGN PROCEDURE OF THE COUPLING COILS

#### 3.1 Design of Wire Litz for the Coupling Coils

This chapter introduces the design procedures of the coupling coil used between the primary and secondary circuits. Since the coupling inductor is made of Litz wire, as mentioned earlier, the selection of such component is an important task. Therefore, the design of the Litz wire can be summarized by the sequences shown in Figure 3.1. Litz Design where 3 steps are explained.

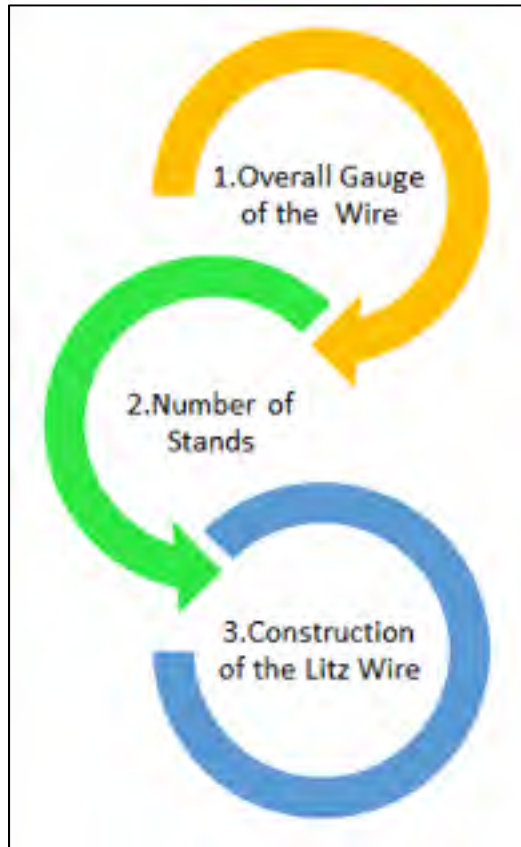


Figure 3.1. Litz Design process.



### 3.1.1 Calculating Overall Gauge of the Wire

The design of the Litz wire usually starts by calculating the current value through the wire. This value was calculated in Equation 2.21 as 15A. That is the current that is going to circulate in the secondary coil. A 20A current was chosen in order to guarantee a safety margin in this application. From the literature review, it is found that the recommended value of the average current density for a given continuous power level and temperature rise over ambient temperature for convection cooling lies between 2 to 6 A/mm<sup>2</sup>, in this case, 5 A/mm<sup>2</sup>. (J. Sallan, 2009) (J. M. Miller and A. Daga, 2015).

$$\begin{aligned}
 \text{Area of cross section of wire} &= \frac{\text{current}}{\text{density}} \\
 \text{Area of cross section of wire} &= \frac{20A}{5 \text{ A/mm}^2} \\
 \text{Area of cross section of wire} &= 4A/\text{mm}^2
 \end{aligned} \tag{3.1}$$

According to the table of American wire gauge (AWG)sizes, a wire of 11 AWG would be enough for this application.

### 3.1.2 Number of Strands

From the literature review for a WPT system, a spiral circular coil is typically used because the profile area is small which is easy to integrate into the system, moreover the circular shape in both coils is more tolerant of alignment errors. Besides, the skin depth is first calculated using Equation 3.2 to calculate the number of strands (A. E. Ruehli, 2012):

$$\delta = \sqrt{\frac{\rho}{\pi f \mu}} \tag{3.2}$$

Where  $\delta$  represents the skin depth in mm,  $f$  the frequency in Hz,  $\mu$  the magnetic permeability of the conductor in H/m, and  $\rho$  the resistivity of the conductor in  $\Omega\cdot\text{m}$  (Akhbari, 2009), chosen



as ( $\rho = 1.72 \times 10^{-8} \Omega m$  at  $20^\circ\text{C}$  and  $2.3 \times 10^{-7}$  at  $100^\circ\text{C}$ ). (C. R. Sullivan and R. Y. Zhang, 2014). Skin depth is complicated by the fact that it has to be known the skin depth not in a solid conductor, but in a medium comprising copper strands separated by thin insulation and airspace.

Considering the previous description, the skin depth is calculated:

$$\delta = \sqrt{\frac{1.72 \times 10^{-8}}{\pi \times 100000 \times 4\pi 10^{-7}}} = 0.2087 \text{ mm} \quad (3.3)$$

Additionally, the skin depth is a measure of the depth at which the current density falls to  $1/e$  of its value near the surface. Over 98% of the current will flow within a layer 4 times the skin depth from the surface. This behavior is distinct from that of direct current which usually will be distributed evenly over the cross-section of the wire. Consequently, the diameter of the strand is selected 4 times smaller than the skin depth (B. Esteban, 2015).

Therefore, the area of the cross section of each strand is calculated by (Aditya, 2016):

$$\begin{aligned} A_n &= \left(\frac{\pi}{4}\right) \times d_n^2 \\ A_n &= 0.0081 \text{ mm}^2 \end{aligned} \quad (3.4)$$

Having the areas now the number of strands can be calculated by:

$$\begin{aligned} \text{Number of strands} &= \frac{\text{area of cross section of overall wire}}{\text{area of cross section of each strand}} \\ \text{Number of strands} &= \frac{4}{0.00801} = 499.37 = 500 \text{ strands} \end{aligned} \quad (3.5)$$

### 3.1.3 Construction of the Litz Wire

The construction of a Litz wire can be affected by different factors, such as skin and proximity



effects, which can be divided into strand level and bundle level. Strand level is the number of individually insulated conductors forming a bundle. Nevertheless, a simple twisting is enough to eliminate the bundle-level proximity effect. (C. R. Sullivan, 1999)

The number of strands can be obtained using the following equation for  $n_1$ :

$$\begin{aligned} n_1 &= \frac{4(\text{sink depth})^2}{(\text{diameter of single strand})^2} \\ n_1 &= \frac{4(0.2087\text{mm})^2}{(0.101\text{mm})^2} \\ n_1 &= 17 \end{aligned} \tag{3.6}$$

The first strand level of twisting is 17 strands together. Then, the number of bundle packing is calculated to reach the 500 Strands resulting in Equation 3.5. For the first bundle level: 17 strands with 5 bundle packing is 85 strands (5 bundle packing is selected because of the skin effect on the WPT and the high frequency. This number of packing is typically used in (C. R. Sullivan, 1999)).

Having the number of strands in the first level and the number of bundle level. Then, the number of bundle packing is 6 in order to reach the 510 strands. The result is calculated by  $17(\text{number of strands}) \times 5 (\text{number of bundle level}) \times 6(\text{number of bundle packing}) = 510$  strands. Moreover, having the number of strands, the number of bundles packing with the American gauge table an 11AWG with single nylon was selected.

However, a 16 AWG roll was used for the coil construction because It was a wire in stock in GREPCI lab. For the AWG the lower the gauge number, the thicker the wire. Thicker wire presents less resistance to current flow, but in this case, because it is the short distance a 16 AWG does not affect the design of the system. Moreover, it is cost-effective and easy to work with.



### 3.2 Design of coils' geometry

An Archimedean spiral form was chosen due to the literature review shown in Chapter 2. In Figure 3.2, the geometrical design is described.



Figure 3.2. Spiral Coil.

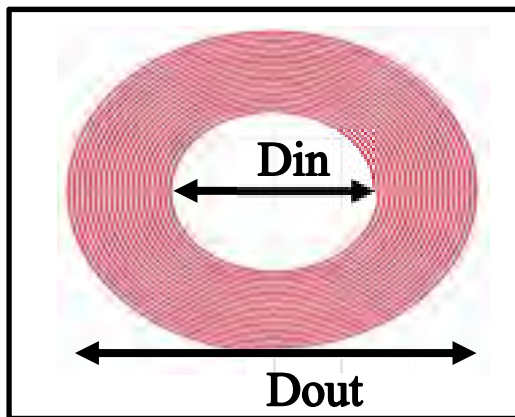


Figure 3.3. Coil Diameters

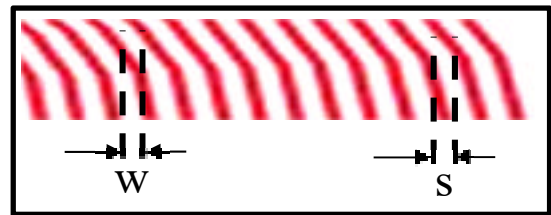


Figure 3.4. Coil Distances







The design process can start with the selection of the diameters in and out. For this application,  $D_{out}$  can be selected considering the air gap from the coils: the primary and the secondary and the physical space of the prototype.  $D_{out}$  was defined as 250 mm because is the area that the scooter has available on the floor next to the batteries Taking Figure 3.2, Figure 3.3 and Figure 3.4 as reference. The following equation is used.

$$L = \frac{a^2 N^2}{8a + 11c} \quad (3.7)$$

The inductance value is calculated, the value is in  $\mu\text{H}$ ,  $N$  is the numbers of turns.

The values of  $a$  and  $c$  are calculated by:

$$a = \frac{D_{out} + D_{in}}{4} \quad (3.8)$$

$$c = \frac{D_{out} - D_{in}}{2} \quad (3.9)$$

Using (3.8),(3.9) and (3.7):

$$L = \frac{N^2 (D_{out} + D_{in})^2}{8(15D_{out} - 7D_{in})2.54} \quad (3.10)$$

Equation 3.10 gives the inductance value in  $\mu\text{H}$  when all the dimensions are in cm.

The equation (3.11) gives the relation between  $D_{out}$  and  $D_{in}$ . This equation comes from Wheeler formula and is going to be used for the design:

$$D_{out} = D_{in} + 2w + (S + w)(2N - 1) \quad (3.11)$$

Figure 3.5, the geometrical specifications are shown below.



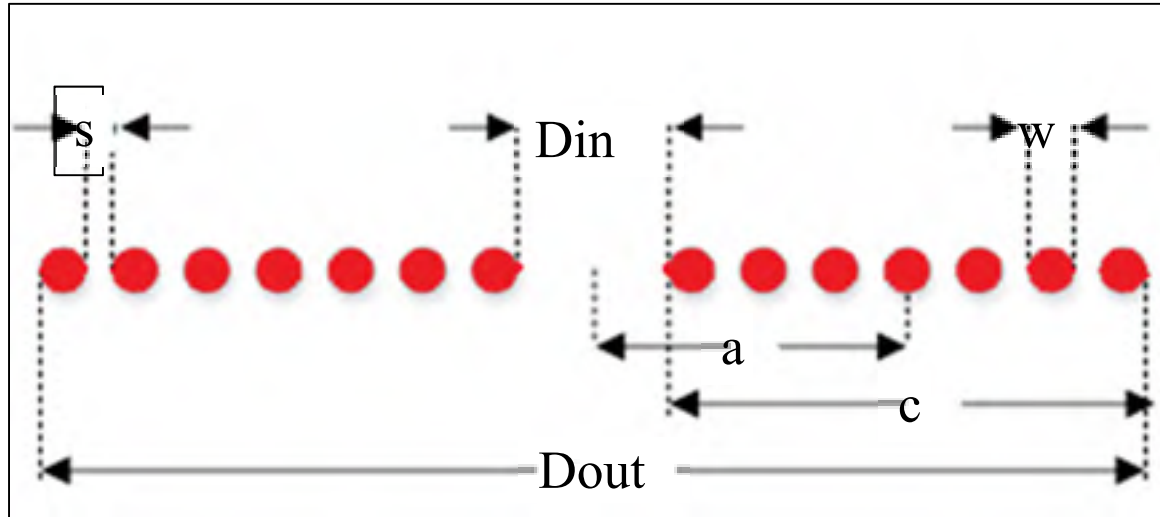


Figure 3.5. Coil Geometry

The design process starts with the  $D_{out}$  selection. It was defined before as 250 mm because is the area that the scooter has available on the floor next to the batteries. Following the numerical interaction process for  $N$  defined as 20 (this value comes from equation 2.9 but it was selecting 20 having an error margin),  $S$  0.001 (value close to zero),  $w$  4.1723 (value from the AWG wire) the parameters are shown in Table 4.

**Table.4.** Calculated values for coils' geometry

<i>Coils</i>	<i>N</i>	<i>D<sub>out</sub> (mm)</i>	<i>D<sub>in</sub> (mm)</i>	<i>S (mm)</i>	<i>W (mm)</i>
<i>P</i>	20	250	50	0.01	4.1723
<i>S</i>	20	250	50	0.01	4.1723

Inter-turn spacing  $S$  was kept to the minimum possible since it has been established in the literature that an increase in turn spacing decreases mutual inductance. Mutual inductance decreases with turn spacing because flux collapses in between the spacing, thereby reducing the coil's overall magnetomotive force (MMF). In Chapter 2, the calculation was made for  $N=10$ , but for the coil geometry, it was designed with  $N=20$  for the final design. Due to the external factor that decreases the transfer of energy between the coils, the coils were fabricated in the GREPCI lab with a Litz



wire of 16. The final design and Inductance measured around  $50\mu\text{H}$  are shown in Figure 3.6 and Figure 3.7.

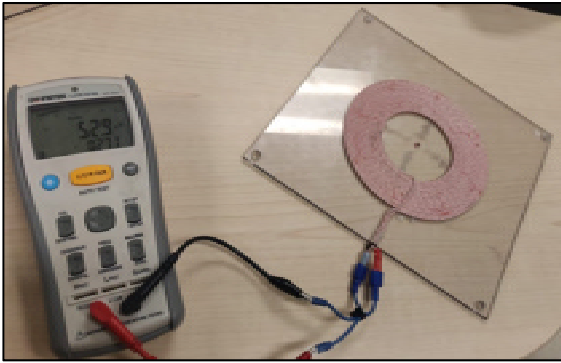


Figure 3.6. Primary coil inductance measures

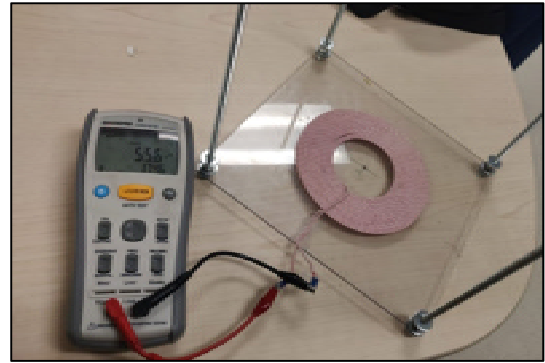


Figure 3.7 Secondary coil inductance measures

Moreover, the inductance was measured around  $50\mu\text{H}$ .

### 3.3 Simulation of Coils in MATLAB

Having the dimensions and geometric shape of the coil, a simulation in MATLAB was made. Modeling Resonant Coupled Wireless Power Transfer System, consists of Matlab code that requires the inner and output diameters in a spiral form, calculated in the previous section. The specifications are shown below:

The antenna Toolbox was used to generate the mesh of the coil. At the first step, the resonant frequency was chosen as a 100 kHz. The code is attached to the references. As the first step frequency boundaries were defined. The resonant frequency is  $f_c = 100\text{ kHz}$ , minimum frequency is  $f_{cmin} = 75\text{ kHz}$ , and maximum frequency is  $f_{cmax} = 113\text{ kHz}$ . Those values were selected based on the Figure 2.9 in order to design the converter in the ZVS area.



### 3.3.1 The Spiral Resonator

Archimedean Spiral Design is the common shape used in the WPT systems. It has less skin effect and is useful for high-frequency applications. On the construction of the coil width of 1.45 mm between coils was selected. The mesh is shown in Figure 3.8.  $D_{in} = 50mm, D_{out} = 250mm, N = 20$ . These values come from Table 4.

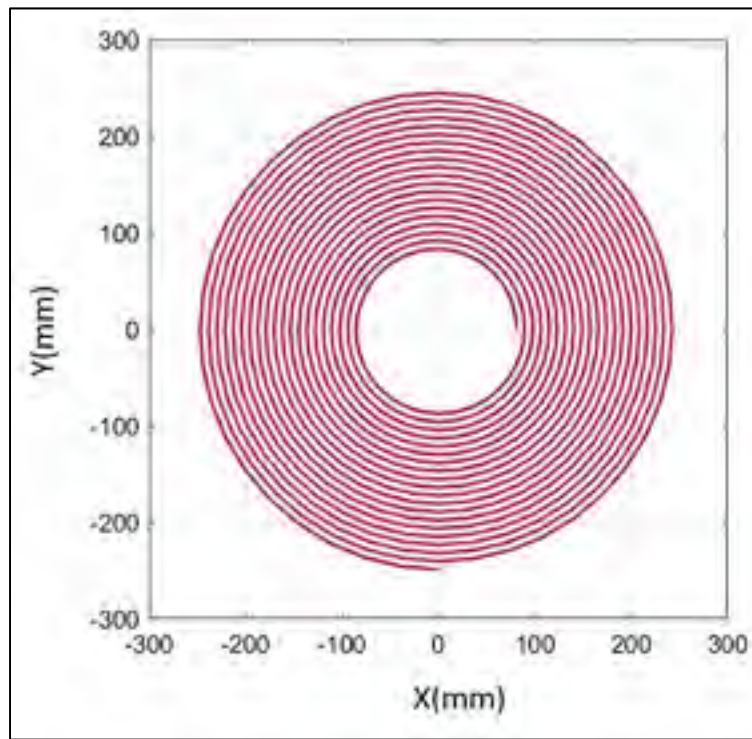


Figure 3.8. Antenna mesh (Appendix C)

### 3.3.2 Resonance Frequency and Mode

The impedance of the spiral resonator is shown in Figure 3.9. Considering that the coil is a magnetic resonator, the Lorentz shape reactance can help the impedance calculation. The high impedance is presented around 84 kHz, which means the design can be used at 100 kHz when the resistance and the reactance of the coil are zero. Leading to maximum transfer energy.



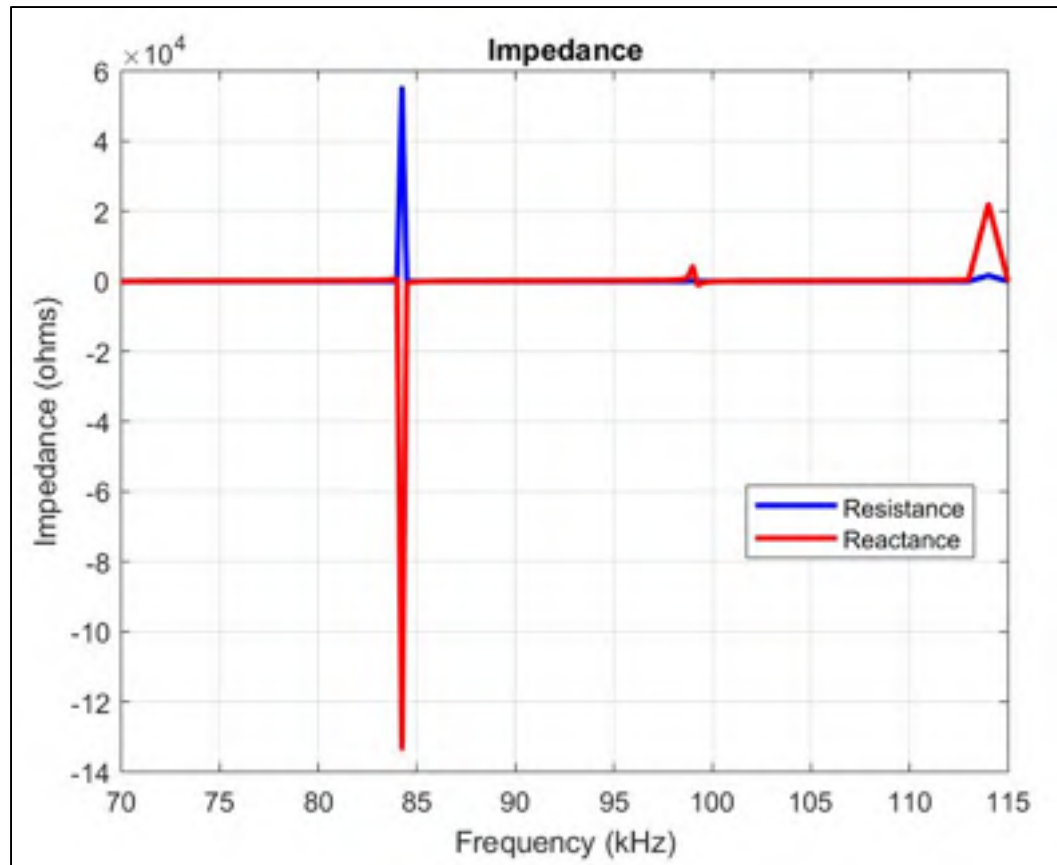


Figure 3.9. Spiral Impedance (Appendix C)

### 3.3.3 Coupling Mode between Two Spiral Resonators

The system is made by a transmitter and a receiver with identical geometric specifications. Seeing a magnetic resonator and the magnetic field, a representation in the near distance is shown in Figure 3.10. At the maximum distance of 15 cm, energy transfer is still working. This data is going to be tested in the lab and presented thereafter.



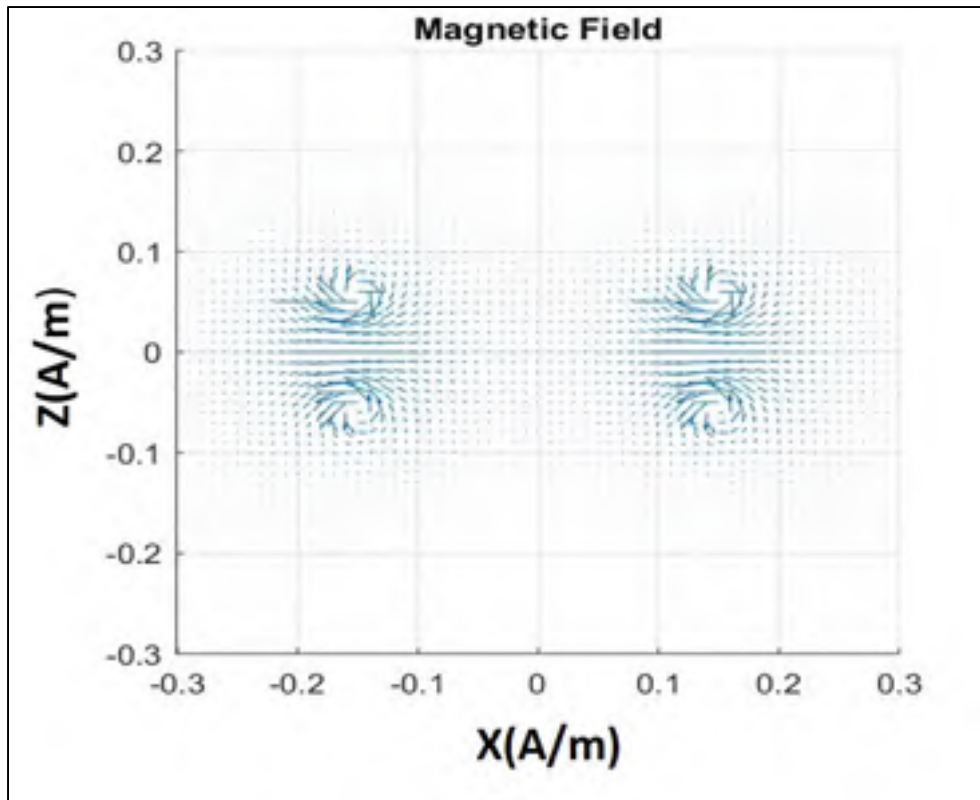


Figure 3.10. Magnetic Field (Appendix C)

### 3.3.4 Variation of System Efficiency with Transfer Distance

One way to evaluate the efficiency of the system is by studying the  $S_{21}$ . The S-parameters has shown in Figure 3.11. are defined by a matrix of Reflection/Transmission characteristics (Amplitude/Phase) in the frequency domain. This type of parameters can be measured with Vector Network Analyzer (VNA) and Time domain Reflectometers (TDR).



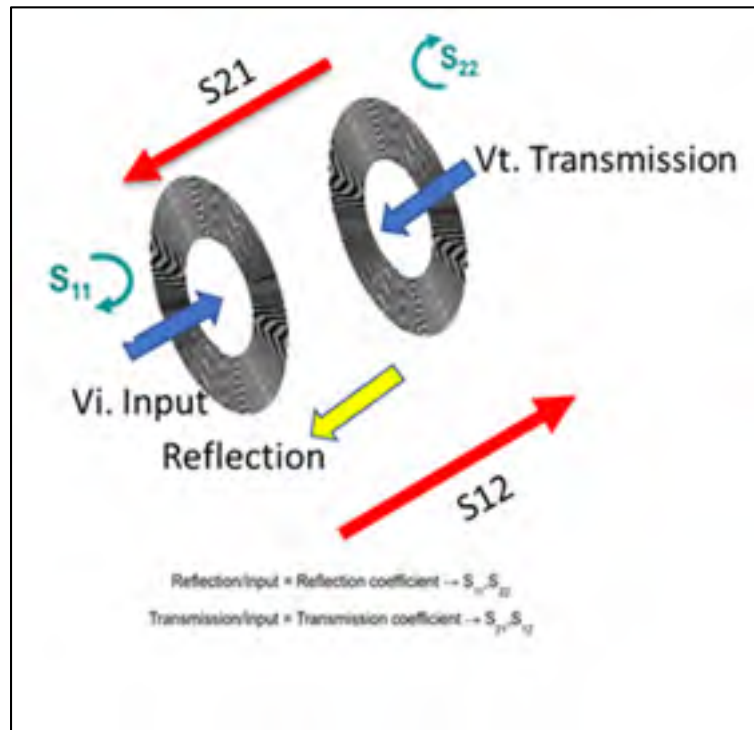


Figure 3.11 S Parameters

Furthermore, the system efficiency can be evaluated with the operating frequency and the coupling strength between the coils. Figure 3.12 shows the maximum efficiency at operating frequency and the maximum distance where the two coils can be coupled.

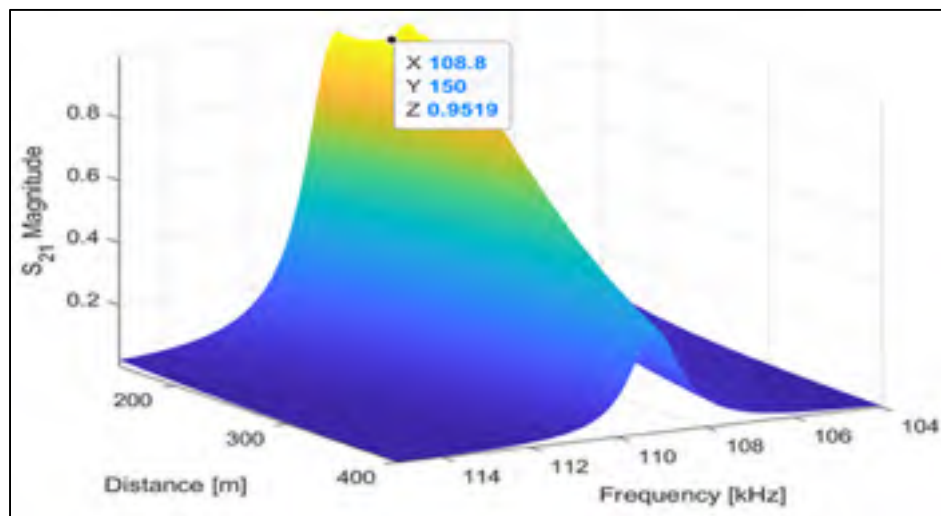


Figure 3.12. Efficiency (Appendix C)



As presented, the maximum efficiency is obtained at a frequency of 108.8 kHz, with a maximum distance of 15 cm and an  $S_{21}$  of 0.95.

### 3.4 Laboratory Tested Coils

As mentioned before, efficiency can be measured with a VNA instrument, which in this project the ENA series Networker Analyzer E5061B 5 Hz – 3 GHz in GREPCI Lab was used. For this test, the coil was connected directly to the VNA considering that the inter impedance of the VNA is  $50\ \Omega$ . The setup and connections are presented in Figure 3.13



Figure 3.13. Setup use for the VNA Test.

In Figure 3.14 shows the description of  $S_{11}$  parameters in the primary coil, where the coil has an impedance of  $26.56\ \mu\text{H}$  that is close to  $30\ \mu\text{H}$ . This test was repeated many times and the inductance was changing every time due to the connectors and the type of wire that was used, the average reading was  $30\ \mu\text{H}$ .



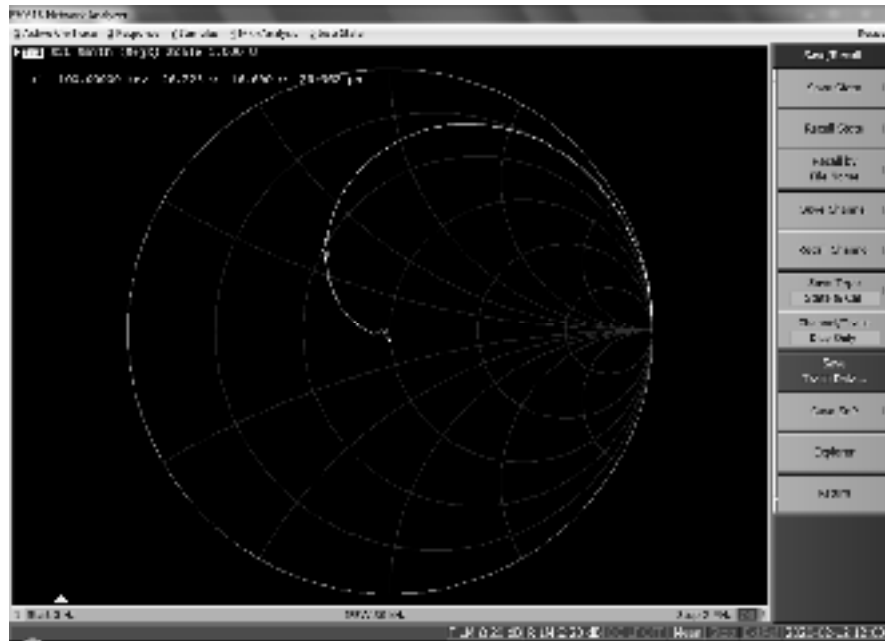


Figure 3.14. S Parameter (Smith Chart with the Y (real part) and Z (Imaginary))

In this chapter, the design procedures of the coupling coil used between the primary and secondary circuits were applied. The overall gauge of the wire and the number of strands were calculated depending on the power that needed to be transferred as well as the frequency and the current flowing in the wire found in the previous chapter. The construction of the Litz wire was made considering the wire quality, the number of strands as well as external parameters. Then, a Litz wire of 15 was designed and tested independently before adding the LLC converter.















## CHAPTER 4

### CONTROL OF LLC CONVERTER

For the efficiency of the WPT system, the power transfer must be kept constant for a period of 6 hours at least to charge the battery. Factors such as pads alignment, fluctuation in supply voltage, variation in the load, and battery pack can affect the system performance. The objective is to design a voltage control loop to regulate the output voltage, according to a predefined reference voltage

#### 4.1 Modelling of the System

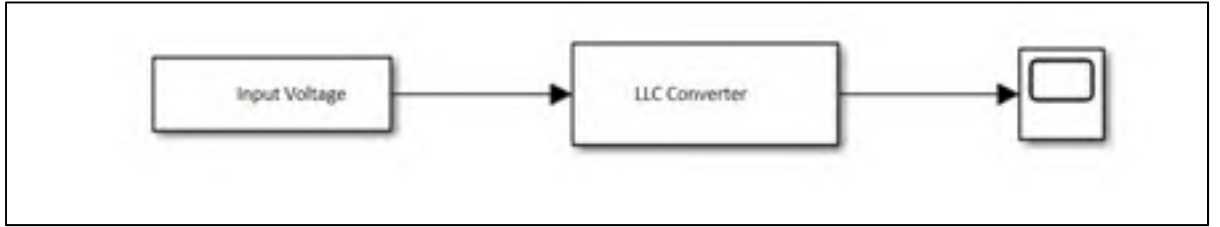


Figure 4.1 Conversion scheme block diagram used in the simulation.

For the design of the Open-loop system, a transfer Function of the LLC as defined in chapter 2, was used:

$$Gp(s) = \frac{S^3 Cr Lr Lm + S^2 Cr Re (Lr + Lm) + S (Lm + Re)}{S^2 Cr Lm + S Cr Re} \quad (4.1)$$

The compensation design for the feedback system can be designed using a Bode diagram and root locus.



### 4.1.1 The Root Locus

The root locus method is a plot of all system poles of the closed-loop transfer function as some parameters of the system varied. (B. Kim, 2012)

Verifying the stability of a plant in a continuous-time domain and solving the root locus. In Figure 4.2, Figure 4.3, Figure 4.4, Figure 4.5 and Figure 4.6, the root locus with the different Re are shown:

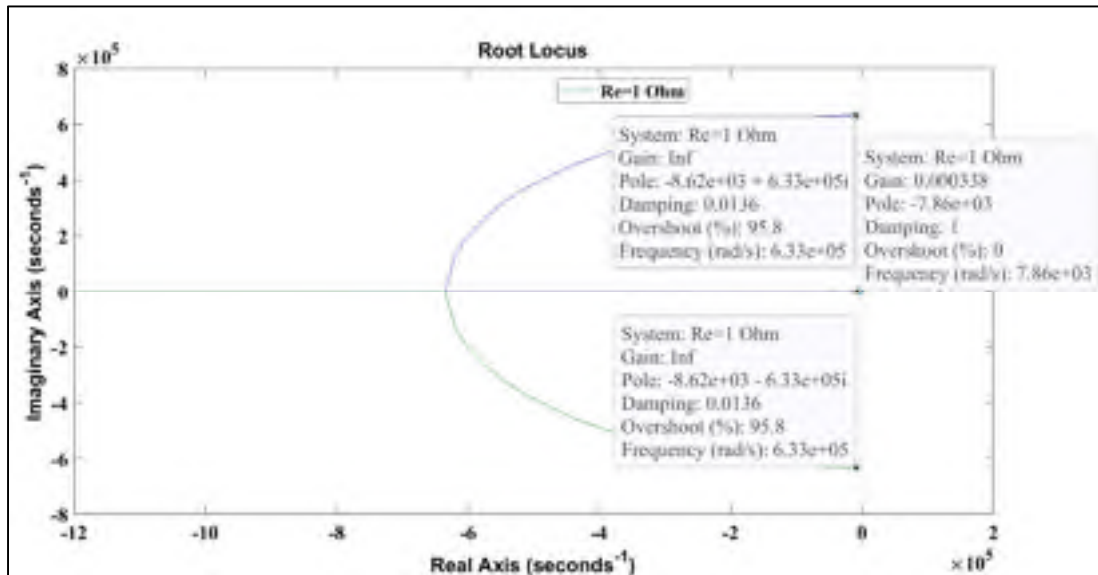


Figure 4.2 Root locus of the system with Re of 1 Ohm



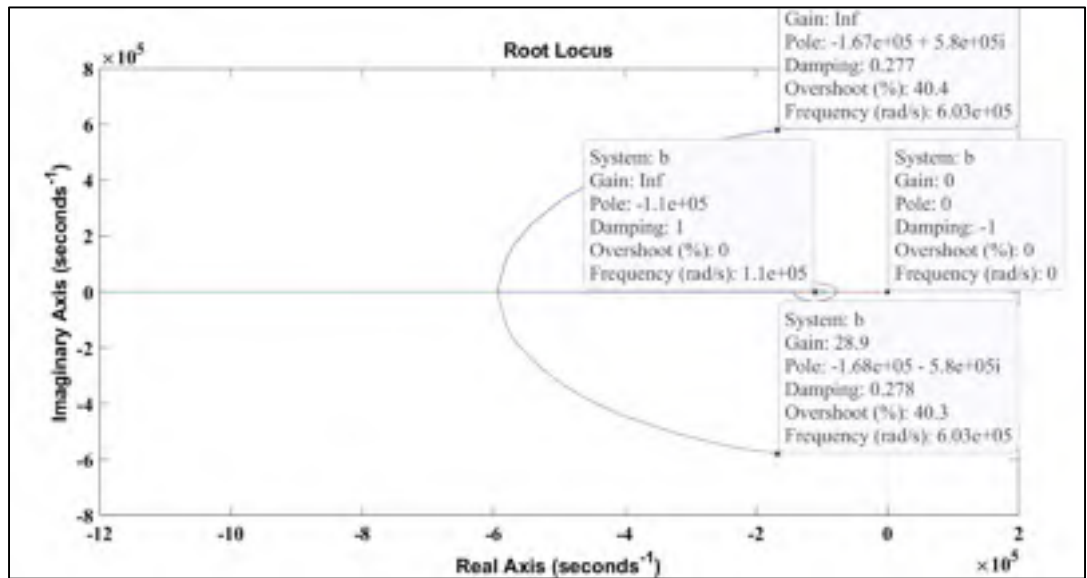


Figure 4.3. Root locus of the system with Re of 20 Ohms

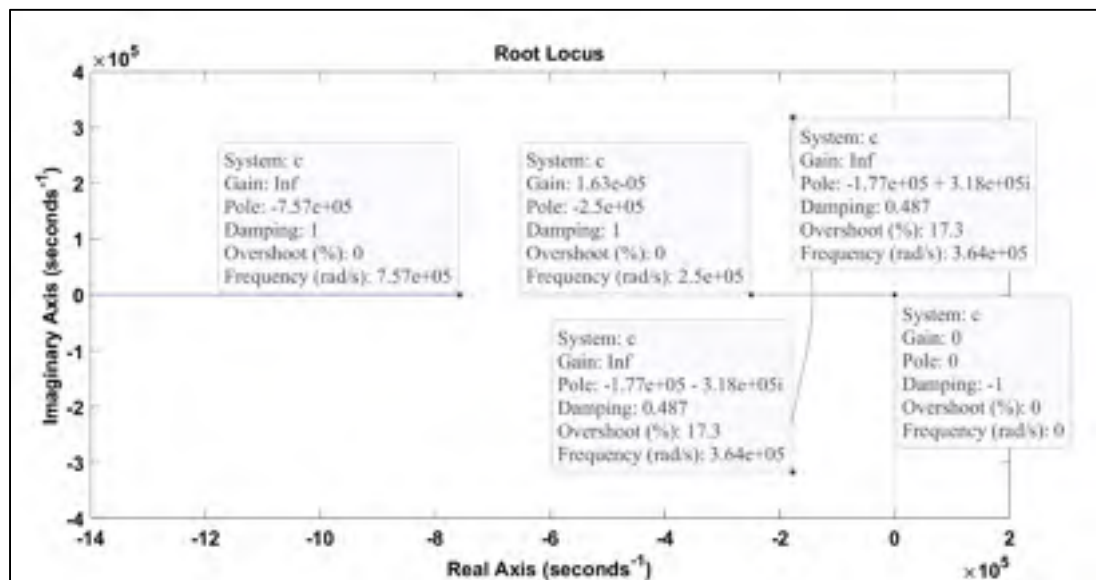


Figure 4.3 Root locus of the system with Re of 50 Ohms



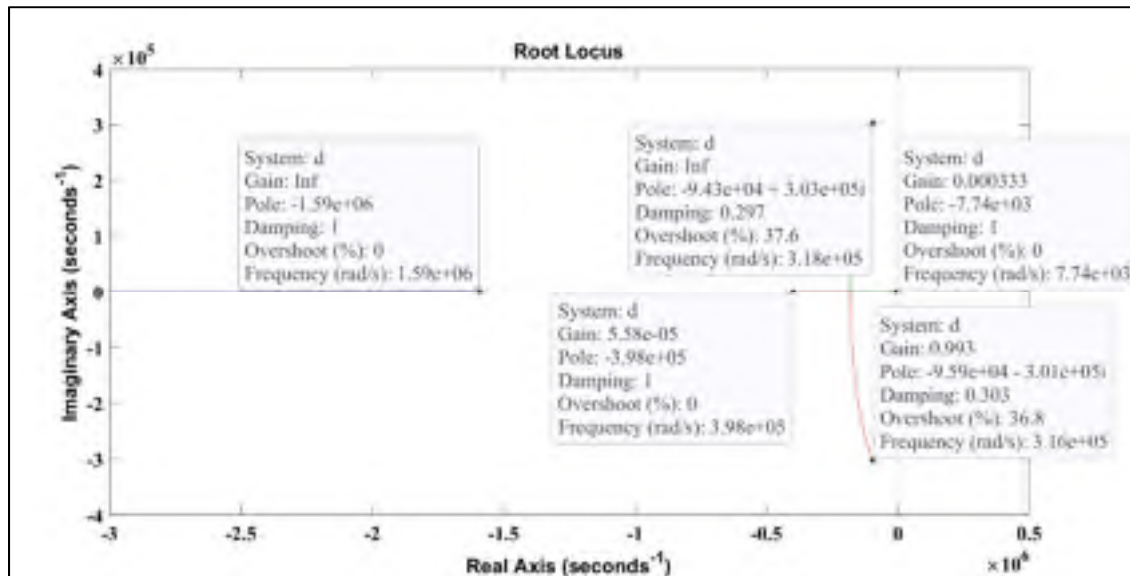


Figure 4.4 Root locus of the system with Re of 80 Ohms

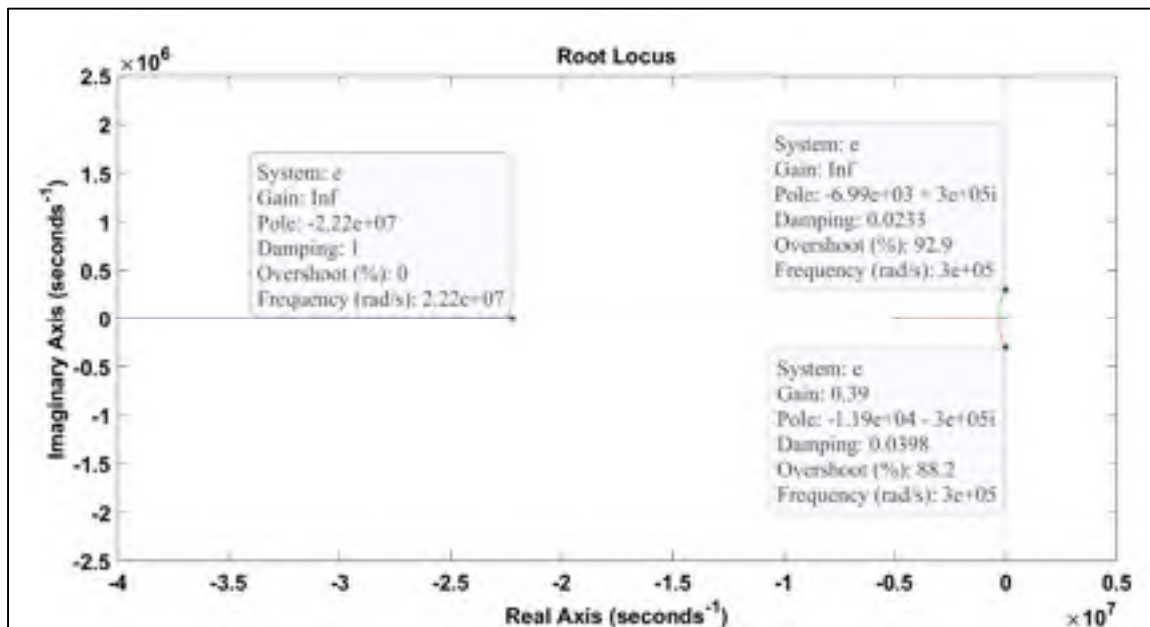


Figure 4.5 Root locus of the system with Re of 1000 Ohms

As shown in Figure 4.2 and Figure 4.6, when  $R_e = 1$  Ohm and 1000 Ohms, these are the critical values of the system due to the proximity of the poles with the Imaginary axis although the



system is still stable. These Figures are the representation of the open loop of the system. For a time, response of 4 seconds and a  $R_e$  of 80 Ohm, the Gain was chosen as 1 as is shown in Figure 4.5 the maximum gain can be 2.93 before the system gets unstable.

#### 4.1.2 Representation using Bode Diagram

Displaying the magnitude and phase responses of a feedback system is a simple tool analyzing transfer function stability as is shown in Figure 4.7.

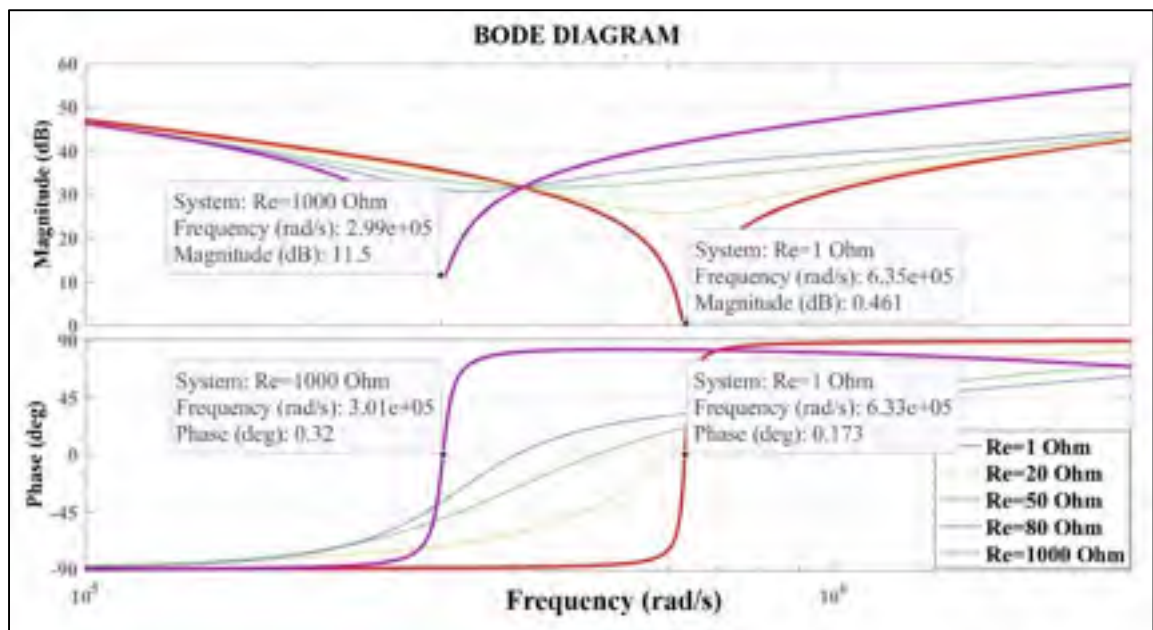


Figure 4.6 Bode Diagram of the LLC system

The stability of the feedback system can be determined from Figure 4.7 by observing the gain and phase margins. The phase margin is defined as the phase difference from -180 at the crossover frequency  $f_c$ . The crossover frequency is defined as the instance at which the magnitude plot is 1. In this case, the  $f_c$  is  $6.33 \times 10^5$  or 100.7kHz. The system with  $R_e=1$  Ohm represents a phase of 0.173 with a magnitude of 0.461dB, and on the other hand, a system with  $R_e=1000$  Ohms obtains a phase of 0.32 with a magnitude of 11.5 db. Moreover, the resonance



frequency of the system was selected as 100 kHz or  $6.28 \times 10^5$  rad/s, which is with a  $R_e = 80 \Omega$  of the maximum frequency of  $6.33 \times 10^5$  rad/s and minimum frequency of  $3.01 \times 10^5$

## 4.2 Voltage Control Loop

As the types of controls were explained in Chapter 1, the one that is common to use in a battery charger application is voltage control varying the frequency of the Mosfet.

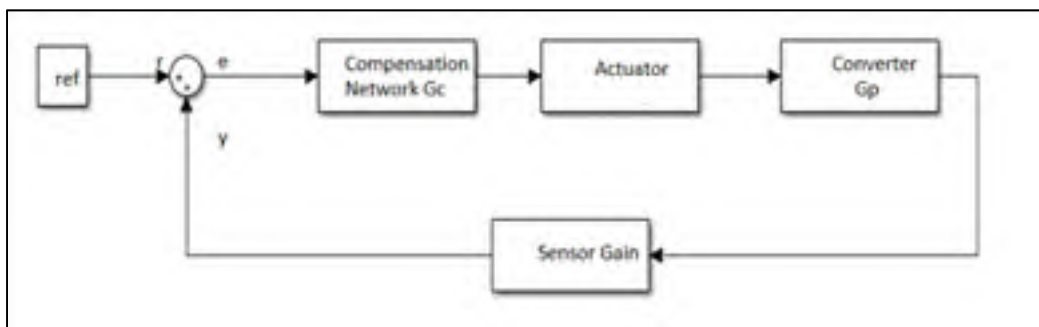


Figure 4.7. Feedback Control loop

In Figure 4.8. a feedback controller eliminates steady-state errors, moderates system sensitivity, and modifies the gain or phase of the system over a fixed frequency. With this digital controller, the main purpose is to generate a gate driving signals of frequency for the primary-side switch.

The system is sensing the output voltage ( $y$ ) and comparing it with the reference value 12V. Then, the compensator  $G_C$  generates the gate drive signals based on the error ( $e$ ), and in a stable control loop system, the error tends to be zero after some time. In order to implement a variable frequency control.

The cost and size of digital signal processors (DSP) have made digital control a practical option for power electronic applications.



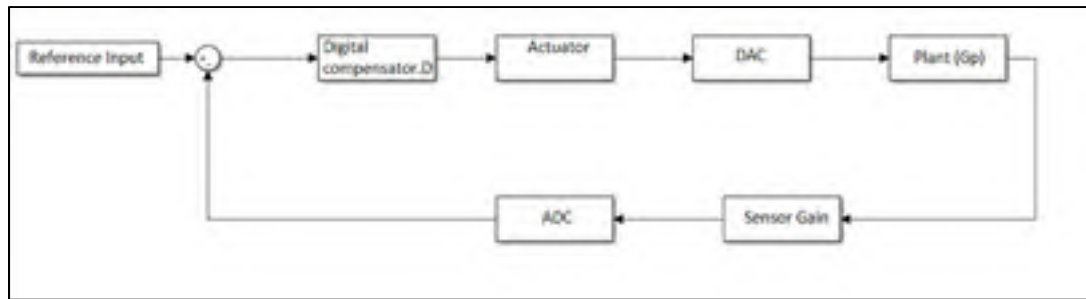


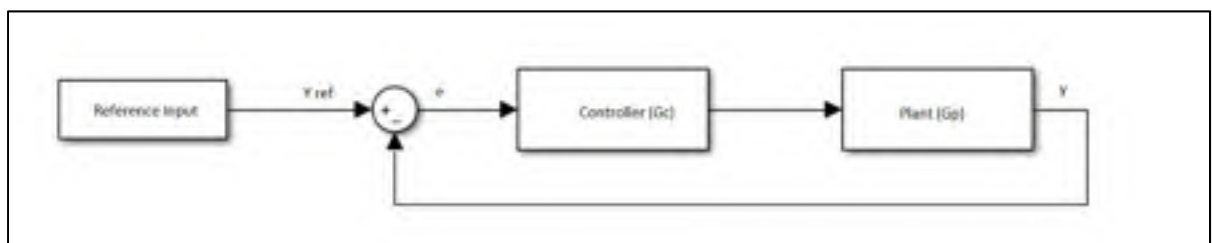
Figure 4.8. Digital Feedback Control loop

There are two main methods to design a digital control system: emulation and direct digital design.

The emulation method uses a continuous-time plant model and obtains the compensation model in continuous time. After having the s-domain model, the conversion to a z-domain is made by mathematical transformation such as Tustin or Euler. Zero hold is the most accurate discretization method. This method is an assurance and the sample rates are fast in the simulation.

### 4.3 Compensator PI Design

The closed loop system with a PID Controller can be defined by:



Where the PI of  $G_c$  is represented as:

$$G_c = \frac{K_p S + K_i}{S} \quad (4.2)$$



The Transfer Function of the system is defined by:

$$\frac{y}{Y_{ref}} = \frac{G_p G_c}{1 + G_p G_c} \quad (4.3)$$

#### 4.3.1 The Root Locus of the PI (Close Loop)

This method relocates the closed-loop poles to meet performance specifications such as overshoot, rise, and settling times. A PI controller increases the low-frequency gain and reduces the steady-state error between the reference and the actual output, while having a positive phase margin. Using the Matlab control system linearized tool, the variables of the controller were defined as  $G_c = 10 + \frac{5e6}{s}$ .

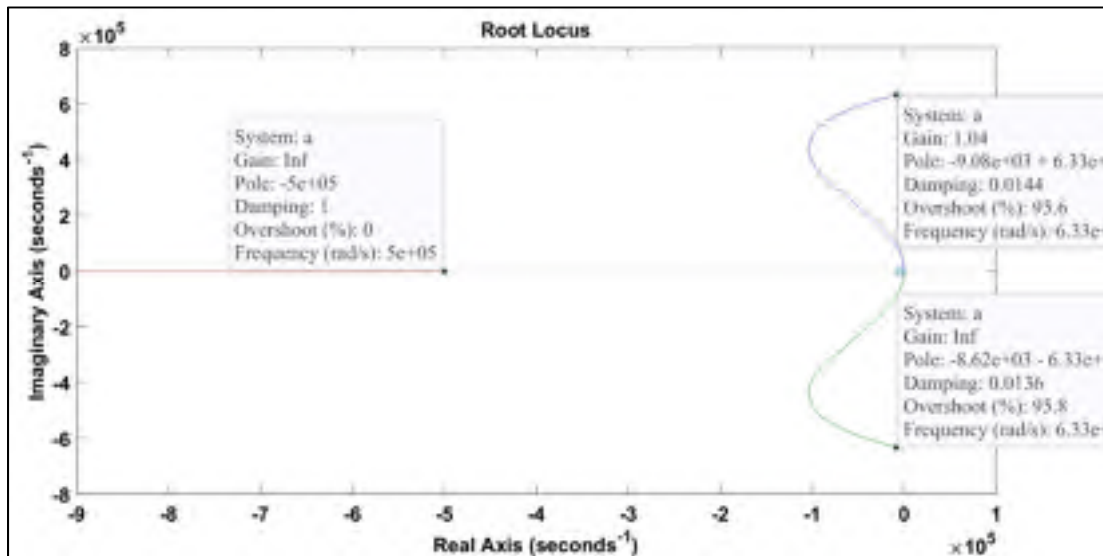


Figure 4.9 Root locus of the close system with PI compensator and Re of 1 Ohm



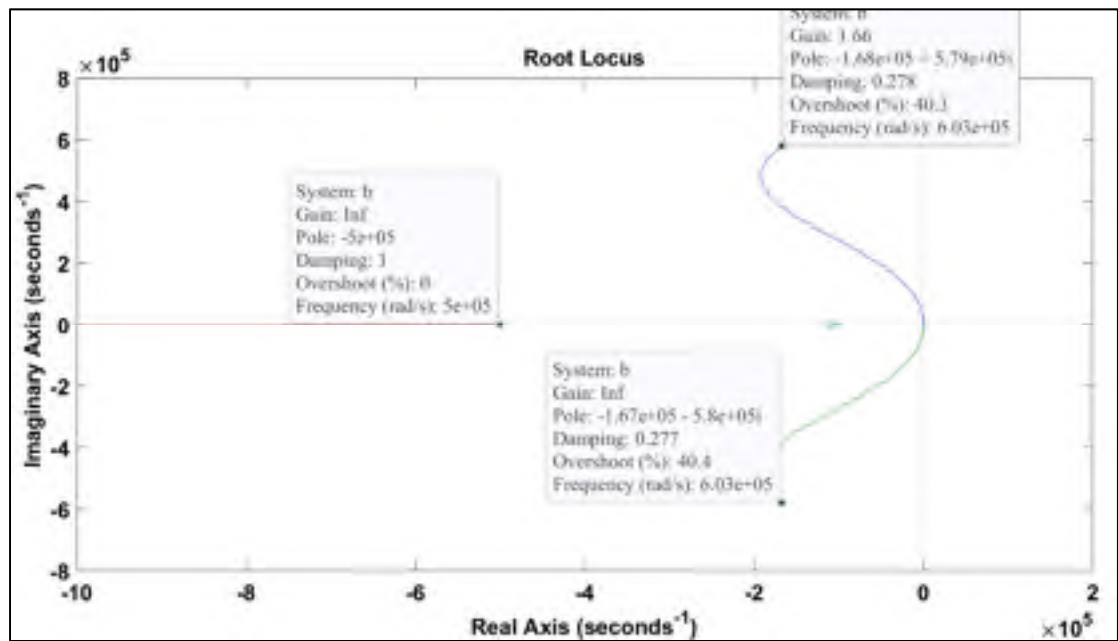


Figure 4.10 Root locus of the close system with PI compensator and Re of 20 Ohms

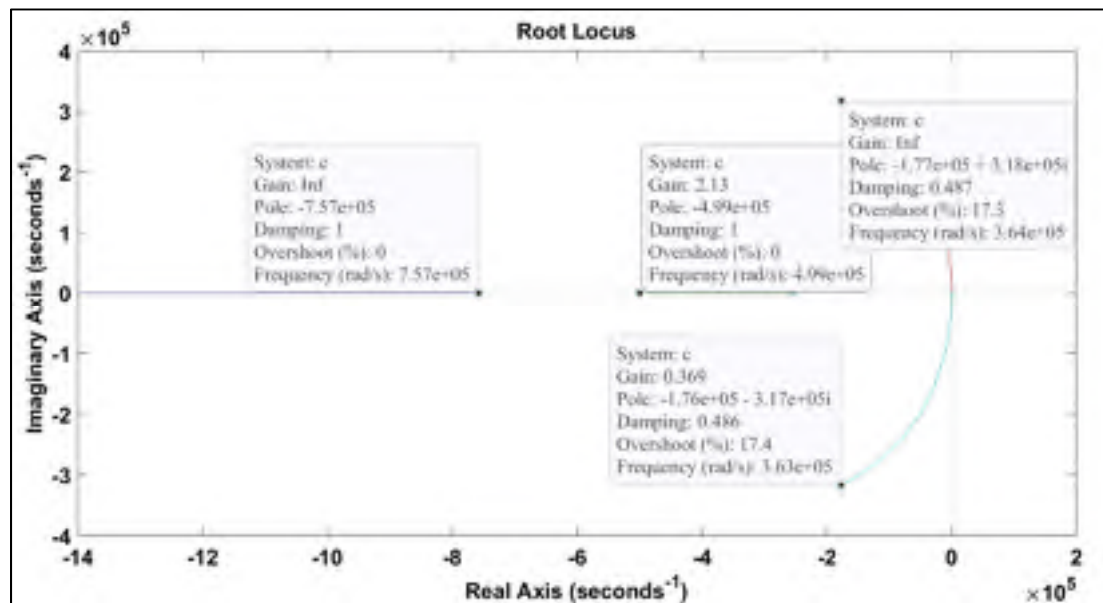


Figure 4.11 Root locus of the close system with PI compensator and Re of 50 Ohms



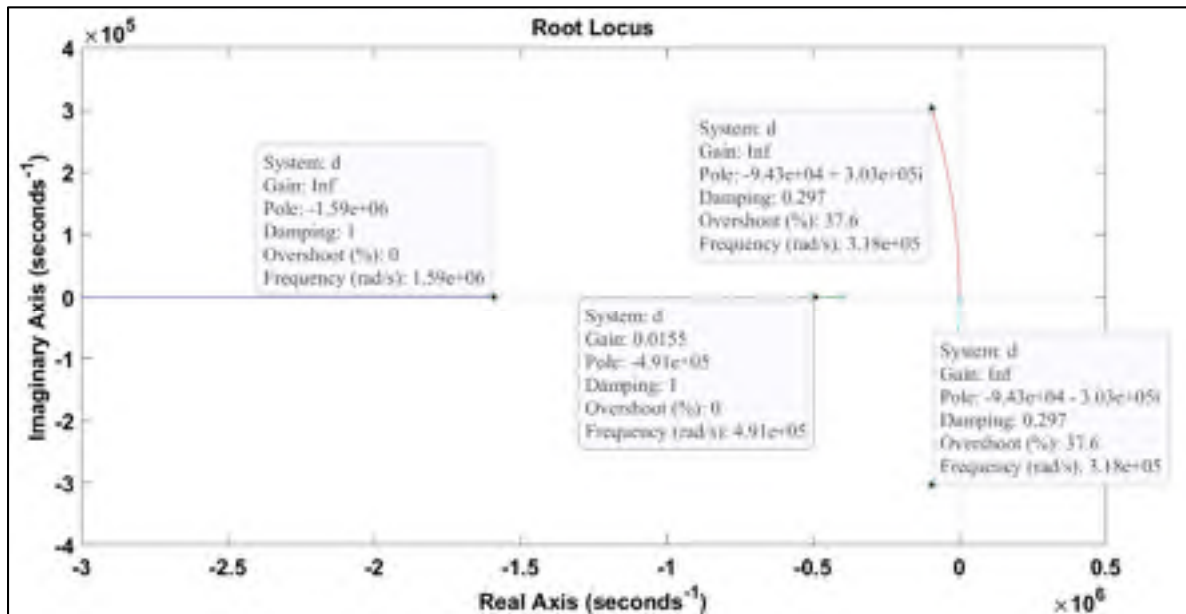


Figure 4.12 Root locus of the close system with PI compensator and Re of 80 Ohms

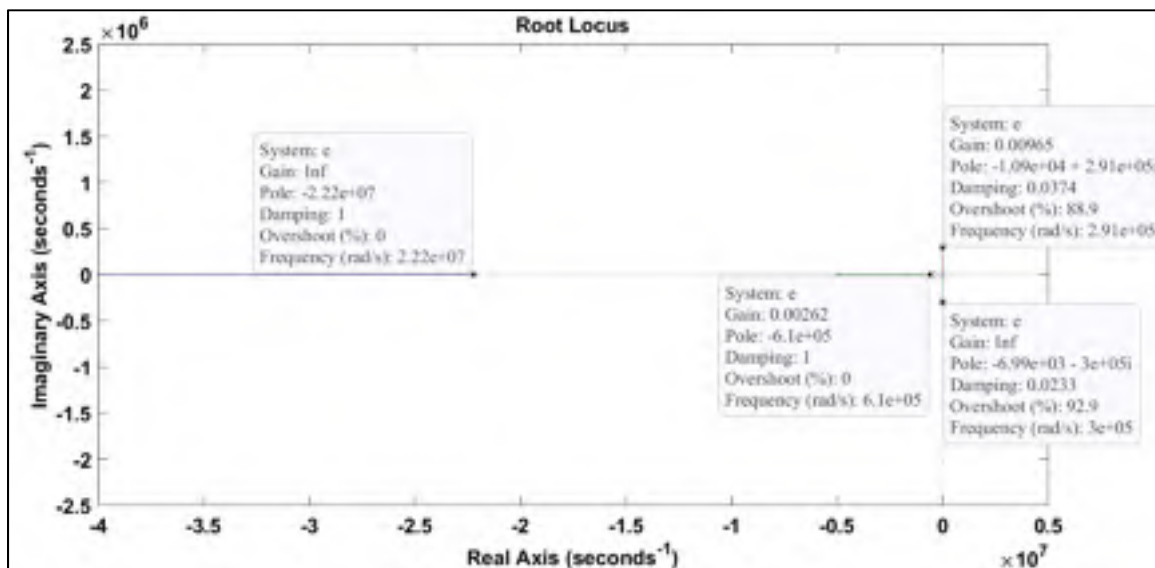


Figure 4.13 Root locus of the close system with PI compensator and Re of 1000 Ohms

With the Root Locus diagrams, the system is trying to be more stable, the poles are moving to the left with a bigger gain, the gains selected for the system was 1.5.



### 4.3.2 Bode Diagram of the PI

The stability of the feedback system can be determined from the Bode diagram by observing the gain and phase margins. For  $R_e = 1 \text{ Ohm}$ , the phase is now 1.54 with a magnitude of 22.6 dB, compared to 0.173 with a magnitude of 0.461 dB without the PI controller. For  $R_e = 1000 \text{ Ohms}$  the phase increases with the same crossover frequency of  $6.33 \times 10^5$  from 0.32 to 1.08 and the magnitude increase from 11.5 dB to 37.3 dB.

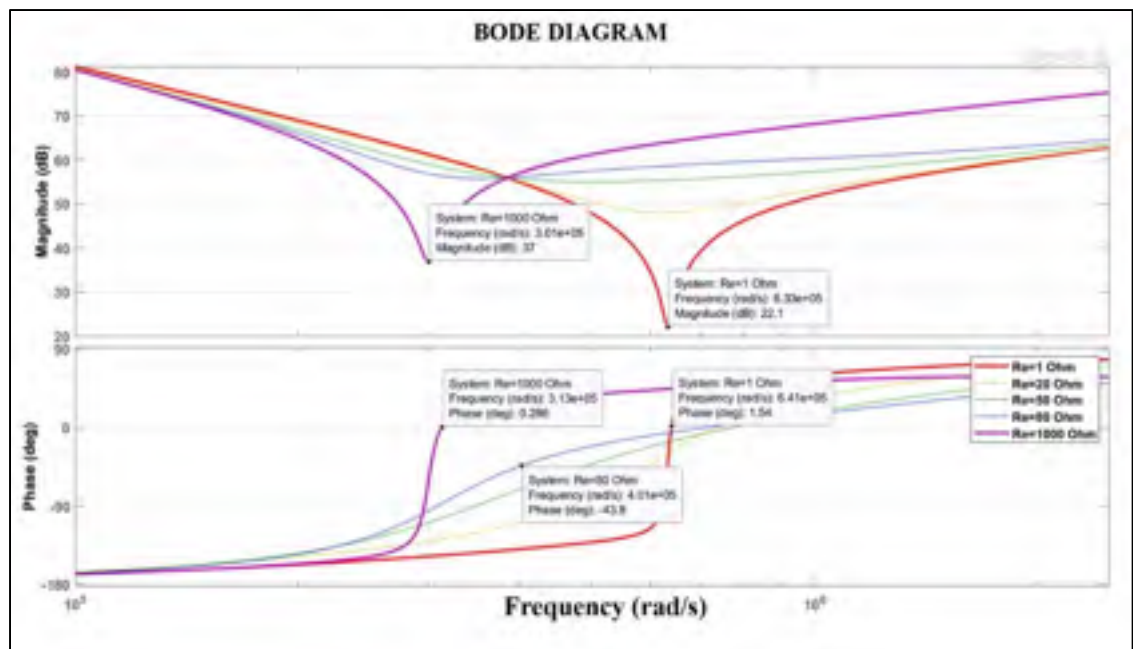


Figure 4.14 PI Controller Bode

## 4.4 Simulation in MATLAB

A PID tuning tool was used to simulate the whole system. Figure 4.16 shows the designed converter and the results.



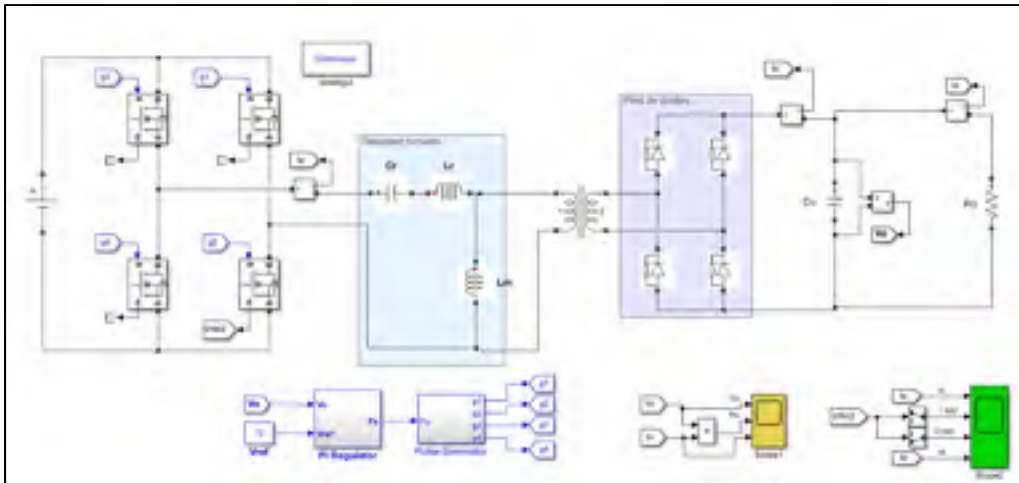


Figure 4.15. Simulation of the LLC converter topology with PI Controller

For the PI Controller, after using the autotuning tool of MATLAB, the value of the proportional was 10 and the integrator was 5e6 as is shown in Figure 4.16. There is no N value because a derivative variable is not going to be used.

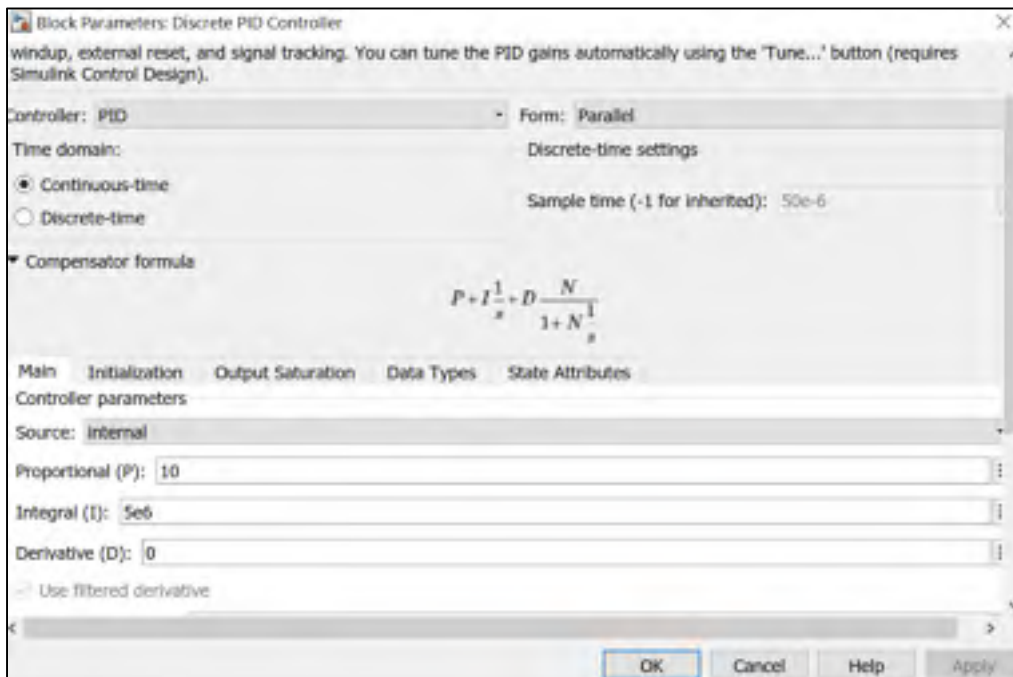


Figure 4.16. PI Parameters



The output voltage and current are 12 V and 12A with an output power of 144W based on the design parameters. As shown in Figure 4.18.

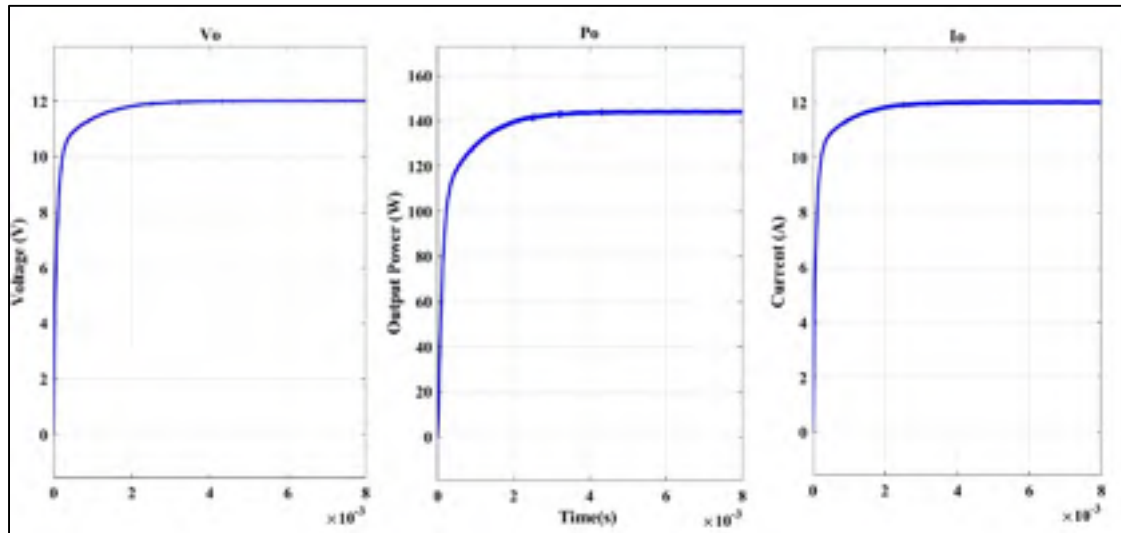


Figure 4.17. Output signal of the LLC converter with the PI controller

This simulation was using the Control system designer tool of MATLAB Simulink, which can linearize the system and tune the PI. In Figure 4.19, the voltage, the current of the Mosfet, and the inverter are shown as well as the  $I_d$  current, which is the output current on the load. In Figure 4.19 a maximum of 4Arms of current is presented in the primary  $I_p$ , with oscillation mood. The sinusoidal current is going through the LLC tank as is desired. The MOSFET on the switching bridge is denied by a  $V_{fet2}$  with an on and off signal of 120 V and a quasi-sinusoidal current going through the MOSFETs of 4Arms. In the last part in the Figure 4.19,



the AC current on the secondary coils is 12A as is desired.

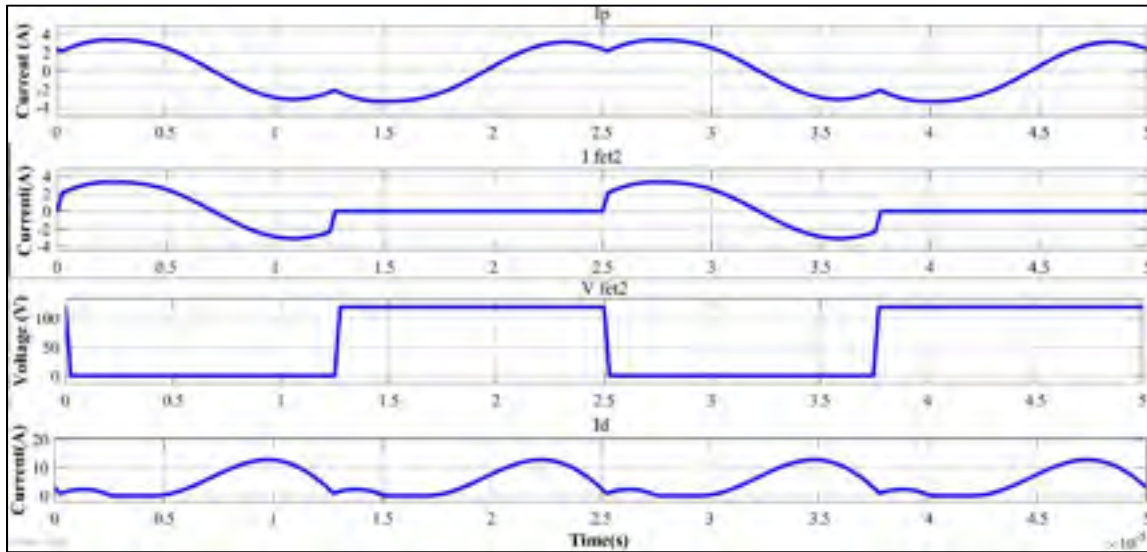


Figure 4.18. FET Voltage and Current

In this chapter, a PI voltage control was designed for changing the switching frequency in the full-bridge Mosfet. Through analyzing the open and close loop on the plant via bode diagram and root locus methods, a PI was designed leading to values of 10 for the proportional value and  $5e6$  for the integrator.

Moreover, the resonance frequency on the Bode diagram was selected as 100 kHz or  $6.2e5$  rad/s. Solving these values in MATLAB, the output voltage and current are 12 V and 12A with an output power of 144W as required.



## CHAPTER 5

### EXPERIMENTAL VALIDATION

#### 5.1 Design of PCB- LLC and rectifier

For the design of the PCB, a circuit simulator software “Proteus” was used on the LLC on the primary coil. The schematic is shown in Figure 5.1 and Figure 5.2. To define the path width of the circuit, a Saturn PCB Software was also used.

##### 5.1.1 PCB LLC Primary

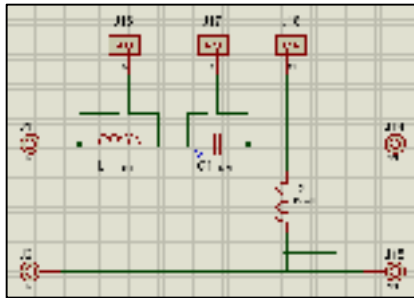


Figure 5.1. Scheme of LLC primary circuit

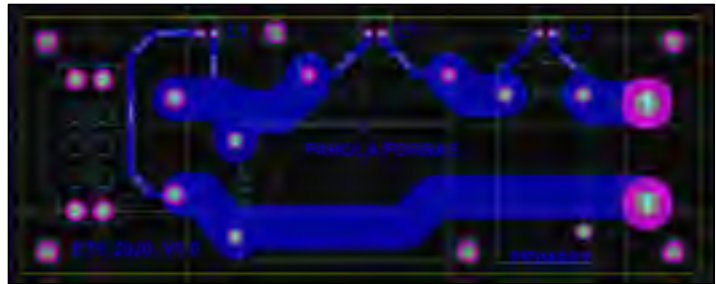


Figure 5.2. PCB design of LLC primary circuit

The 3D views are shown in Figure 5.3 and Figure 5.4. Moreover, this PCB can be used in the future for other LLC systems in GREPCI Lab.



### 5.1.2 PCB LLC Secondary

For the rectifier and filter on the secondary coil, the 4 diodes were MB40250TG, and the Filter Capacitor was 220 UF.

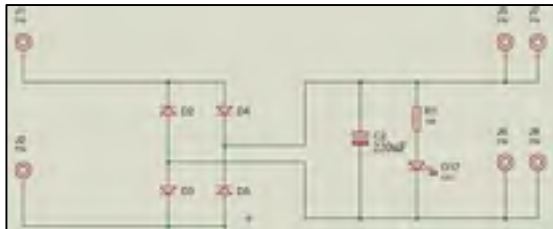


Figure 5.3. Scheme of rectifier secondary circuit.



Figure 5.4 PCB of rectifier secondary circuit.

And the 3D design is shown in Figure 5.5.

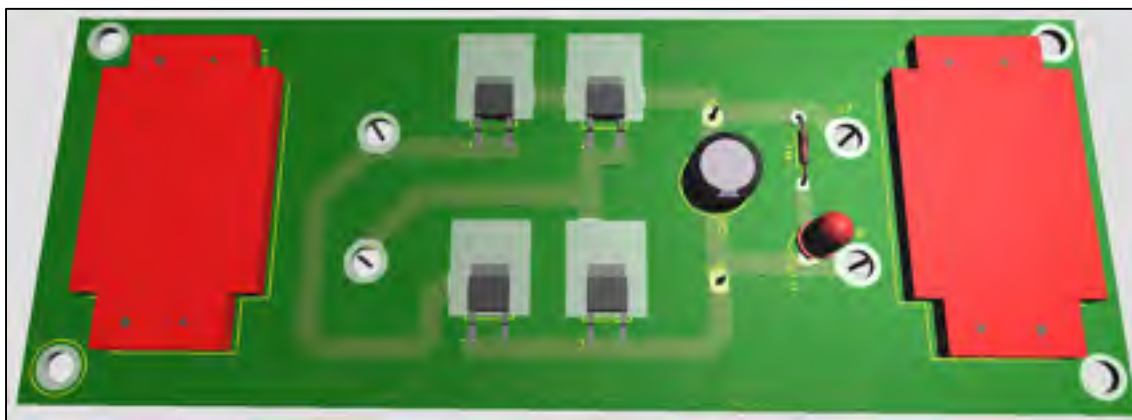


Figure 5.5. 3D Rectifier and Filter.

The LED that is parallel to the Capacitor is an indicator of the voltage on the PCB.

## 5.2 Description of Hardware Setup

The LLC and PI controller designed in the last chapter were implemented in the GREPCI Lab. As shown in Figure 5.6, the whole system integrates the power supply, and the Full bridge rectifier, which were already assembled in the Laboratory, an LLC PCB that were already



described, two spiral coils known as primary and secondary coils with a mechanical system that can change the air gap through 2 long screws, a rectifier circuit, and a filter. The PCB secondary design explained before, contains an ion battery for a Scooter, a Voltage Sensor, which was already found in the GREPCI Lab and a supply voltage of -15V and 15 V. Moreover, the DSP and the buffer do the negation of the PWM used to commute the full-bridge inverter.

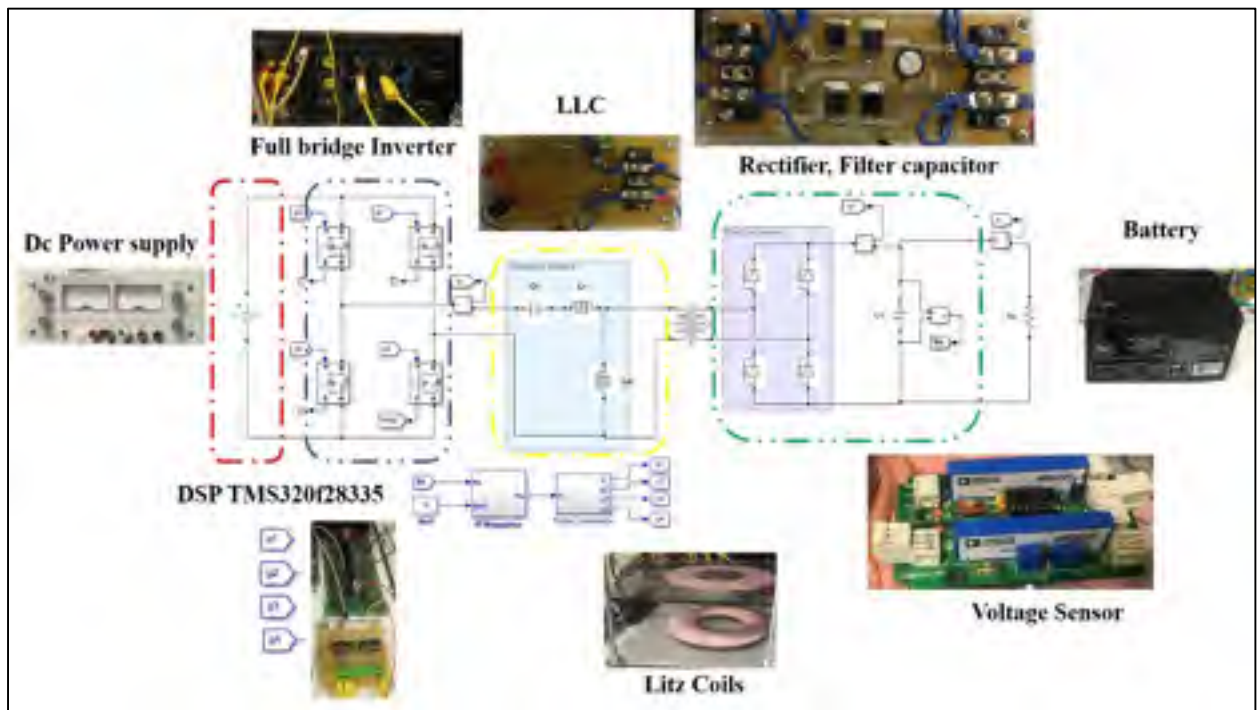


Figure 5.6. Hardware setup in the laboratory

In Table 5.1, the components, used in the hardware setup, are described with a reference number and manufacturer in case some of the components are changed for future tests.







Table 5.1. Components of the designed WPT Charger Scooter.

<b>CIRCUIT CONFIGURATION</b>	<b>COMPONENT DESCRIPTION</b>
DC Source	6236B Triple output power supply Hewlett Packard
Full Bridge Inverter	Mosfet IXTH30N60P 600 Vdss 30A Id25
Resonant Tank LLC	<b>Lr</b> = 60 uH, 16A Part Number: 553-1723-ND Manufacturer: Pulse Electronics power. <b>Lm</b> = 150uH, 30A Part Number: IHV30BZ150-ND Manufacturer: Vishay Dale <b>Cr</b> = 47nF 10% 2KVDC AXIAL Part Number: 338-1173-ND Manufacturer: Cornell Dubilier Electronics (CDE)/ 940C20C47K-F
Rectifier	Switch-mode Schottky Power Rectifier 250 V, 40 A Part Number: MB40250TG
Filter Capacitor	220uF
Battery	Drive Medical Spitfire Scout 4 Wheel SFSCOUT4 12V 12Ah. Manufacturer: Battery Clerk
Voltage Sensor	IC OPAMP ISOLATION 2 CIRC 10SIP Part Number: AD202JY Manufacturer: Analog Devices Inc.
Power Supply Voltage Sensor	Dual Power supply Part number: PC-3030 Manufacturer: Instek
Litz Coil	High frequency Litz wire with nylon served. Model: H2UEW 0.04(mm) Manufacturer: YDK, Korea
DSP	TMS320F28335 Manufacturer: Texas Instruments
Power Supply Buffer	Dual Regulate Power supply Part Number: LQD422 Manufacturer: Lambda
PWM buffer CMOS	1.2A-Peak Low-Side MOSFET Driver Part Number: MIC4469YN Manufacturer: Micrel Inc



Some of the components were already in the GREPCI Lab, and the remaining were ordered online through Digi-Key. During the first test, inductors of 1.25 Watts were used, and every time burned because of the high current through the element. As a result, the inductors were changed to 15 A as detailed in the datasheet. Another aspect to consider is the size of the components and the distance between them. On the first model of the PCB LLC primary, the inductors were too close, making a short circuit. On the PCB rectifier secondary, it was difficult to do the measurements with the oscilloscope of the output voltage because of the connections with the Voltage Sensor. Finally, in Figure 5.7 WPT Scooter Charger, the system is exposed, and the lab tests are shown in the next chapter.

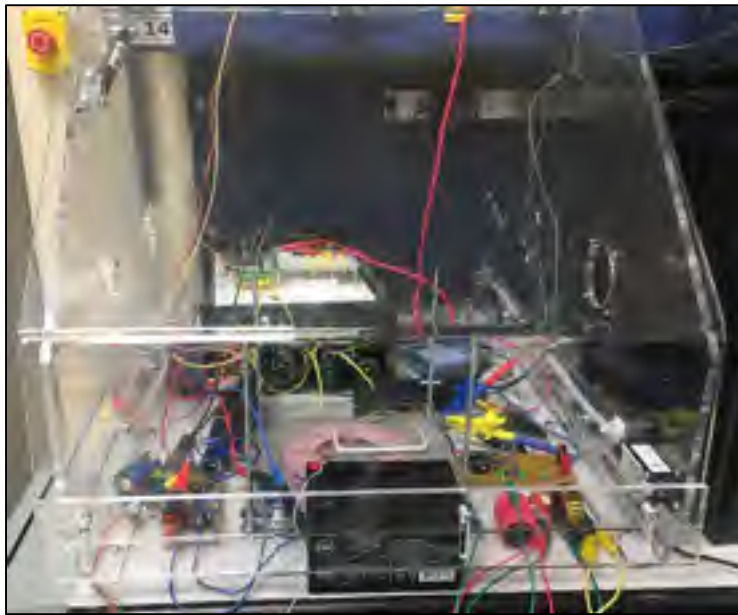


Figure 5.7 WPT Scooter Charger fully implemented

In this chapter, a PCB design with “Proteus” was shown. In the primary PCB the LLC tank is contained, for the secondary PCB, the full bridge rectifier and the output capacitor are shown. The hardware installation on GREPCI Lab is presented and the electrical components are detailed with the circuit configuration and component description in case of future changes.



## CHAPTER 6

### EXPERIMENTAL RESULTS

On the experimental setup, the maximum input supply voltage was set to 10 V. The previous simulations were with 120 V on the entry. For that reason, the same converter design is used, but with less entry voltage in the system.

#### 6.1 Output Inverter

On the experimental setup shown in Figure 6.1, the load was  $1\Omega$  in order to check the current and voltage in the output.



Figure 6.1. Experimental setup for the inverter circuit



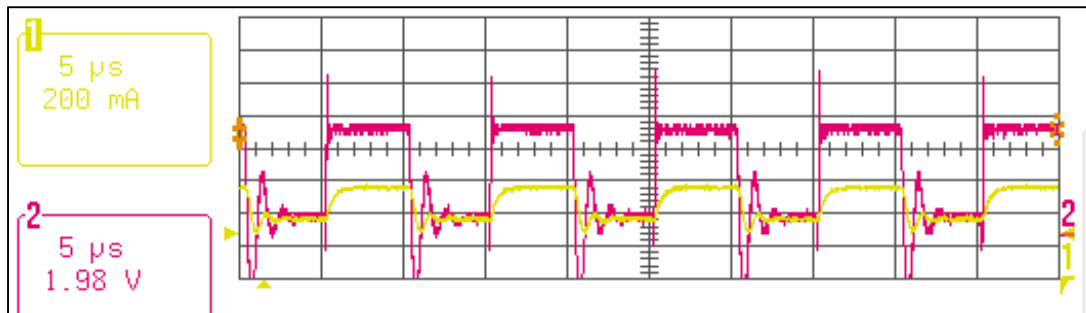


Figure 6.2 Oscilloscope waveforms at the Inverter Output

On the output voltage; the red signal in Figure 6.2, the V peak to peak was 14.25 V and the  $V_{rms}$  was 4.639, with a frequency of 100 kHz. For the Current output signal which is the yellow one in Figure 6.2, the current  $I_{pk-pk}$  was 306 mA and the  $I_{rms}$  was 1.09A.

## 6.2 Air Gap Variations

In the lab, the methodology to verify the design of the WPT was developed as is shown in Figure 6.3.

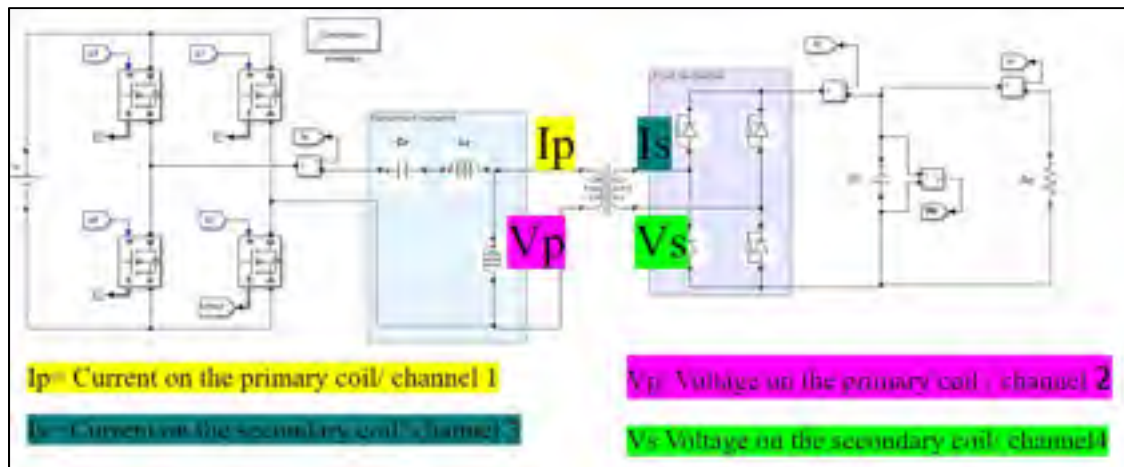


Figure 6.3. Design circuit and hardware connections/Channels in the oscilloscope

In order to identify the channels from the oscilloscope, Figure 6.3 shows where the thumbs were connected in the hardware circuit and the colors of each channel.



### 6.2.1 Air Gap variation of 1 cm

Figure 6.4 shows the measurement of the voltage between the two coils, and the voltage at the primary coil. The yellow channel 1 represents the current in the primary coil, the blue channel 3 represents the current on the secondary side. The red channel 2 shows the voltage in the primary coil and the green channel 4 represents the voltage on the secondary coil.

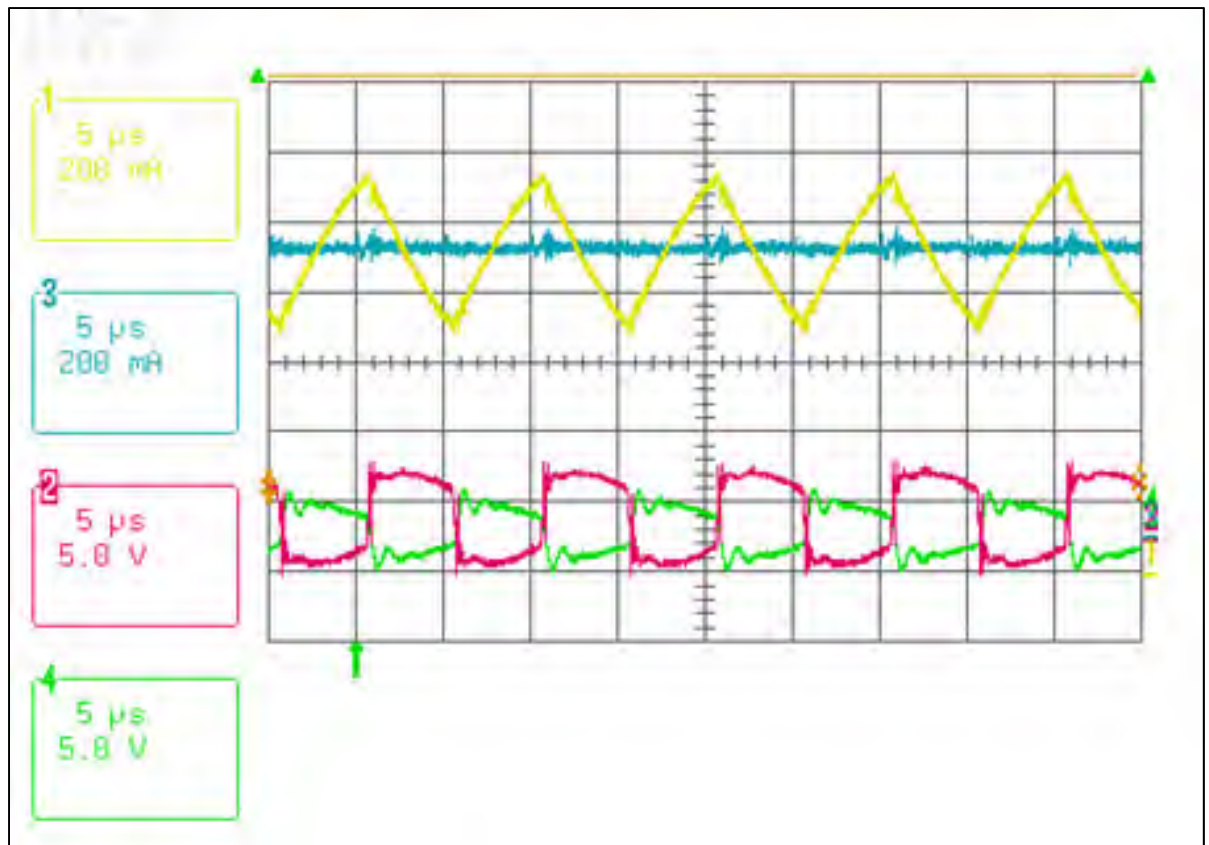


Figure 6.4 Current and voltage levels at the primary and secondary coils for an air gap of 1 cm between coils, max power transfer

As for the current on the primary coil (channel 1, yellow),  $I_{pk-pk}$  is 481 mA and the  $I_{rms}$  is 919.1mA, the output voltage on the primary coil (channel 2, red) is  $V_{pk-pk}$  8.38V,  $V_{rms}$  3.179V. In the secondary coil voltage (channel 4, green) is  $V_{pk-pk}$  5.74V and  $V_{rms}$  2.539V. The efficiency of the system is 79.86%.



### 6.2.2 Air Gap variation of 2 cm

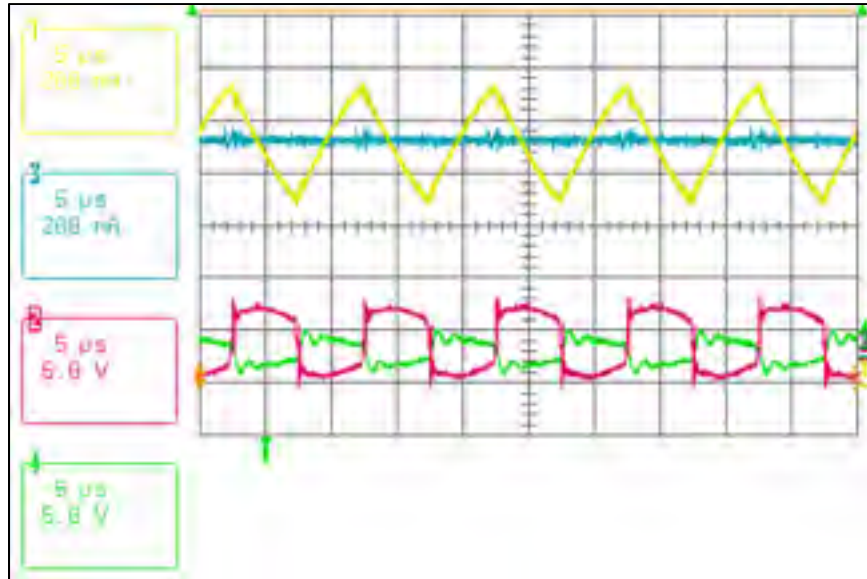


Figure 6.5. Current and voltage levels at the primary and secondary coils for an air gap of 2 cm between the coils.

In Figure 6.6, the current on the primary coil (channel 1, yellow)  $I_{pk-pk}$  is 492 mA and the  $I_{rms}$  is 949.1 mA, the output voltage on the primary coil (channel 2, red) is  $V_{pk-pk}$  2.09 V,  $V_{rms}$  1.623 V. In the secondary coil the voltage (channel 4, green)  $V_{pk-pk}$  is 4.53 V, and  $V_{rms}$  1.276 V. The efficiency of the system is 78.6% with a frequency of 100 kHz.



### 6.2.3 Air Gap variation of 5 cm

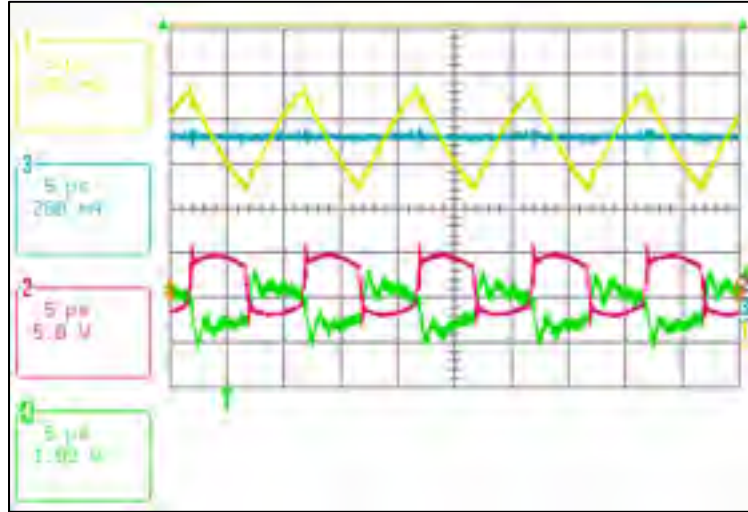


Figure 6.6 Current and voltage levels at the primary and secondary coils for an air gap of 5 cm between the coils

In Figure 6.6, the current on the primary (channel 1, yellow) coil  $I_{pk-pk}$  is 483 mA and the  $I_{rms}$  is 907.1mA, the output voltage on the primary coil(channel 2, red) is  $V_{pk-pk}$  9.57 V,  $V_{rms}$  3.203V. For the secondary coil, the voltage (channel 4, green) is  $V_{pk-pk}$  1.03V and  $V_{rms}$  476 mV. The efficiency of the system is 15 % with a frequency of 100 kHz.



#### 6.2.4 Air Gap variation of 10 cm

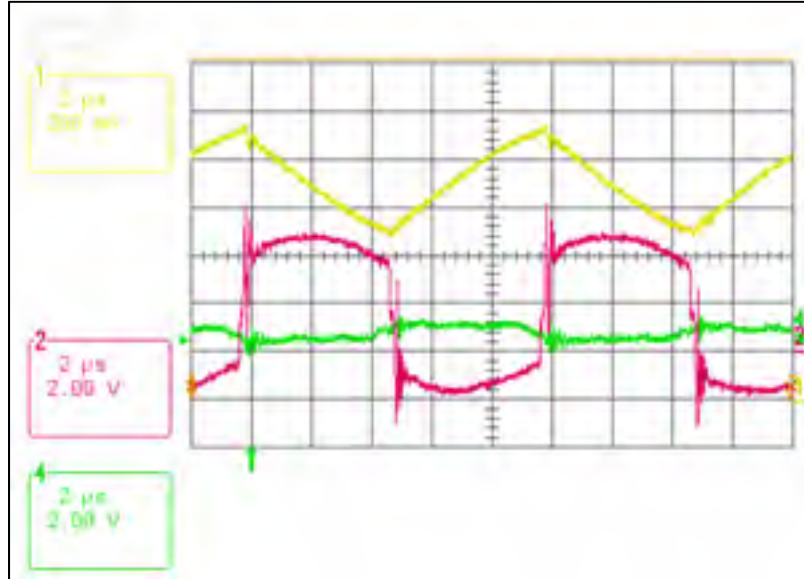


Figure 6.7 Current and voltage levels at the primary and secondary coils for an air gap of 10 cm between the coils

In Figure 6.7, the current on the primary coil (channel 1, yellow),  $I_{pk-pk}$  is 475 mA and the  $I_{rms}$  is 916.3mA, the output voltage on the primary coil (channel 2, red) is  $V_{pk-pk}$  9.16 V,  $V_{rms}$  3.219V. In the secondary coil, the voltage (channel 4, green) is  $V_{pk-pk}$  1.81V and  $V_{rms}$  278 mV. The efficiency of the system is 9 % with a frequency of 100 kHz.

According to the lab tests, the maximum transfer voltage on the secondary is 3 Volts with an air gap of 1 cm.



### 6.3 Experimental results

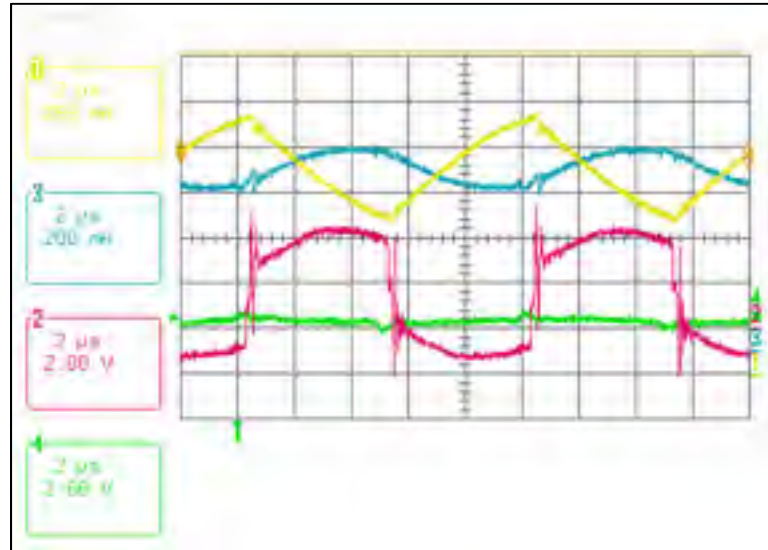


Figure 6.8. Current and voltage levels at the primary and secondary coil with short circuit operation.

In Figure 6.8, having a short-circuit on the secondary coil, the maximum current through the system can be evaluated. The current on the primary coil  $I_{pk-pk}$  is 495 mA and the  $I_{rms}$  is 914.6 mA. On the secondary coil  $I_{pk-pk} = 235$  mA and  $I_{rms} = 806.8$  mA. The maximum current through the circuit is nearly 1A.



6.4 DC exit on the Battery

In Figure 6.9, the dc output voltage is 2.47Vdc directly on the battery.

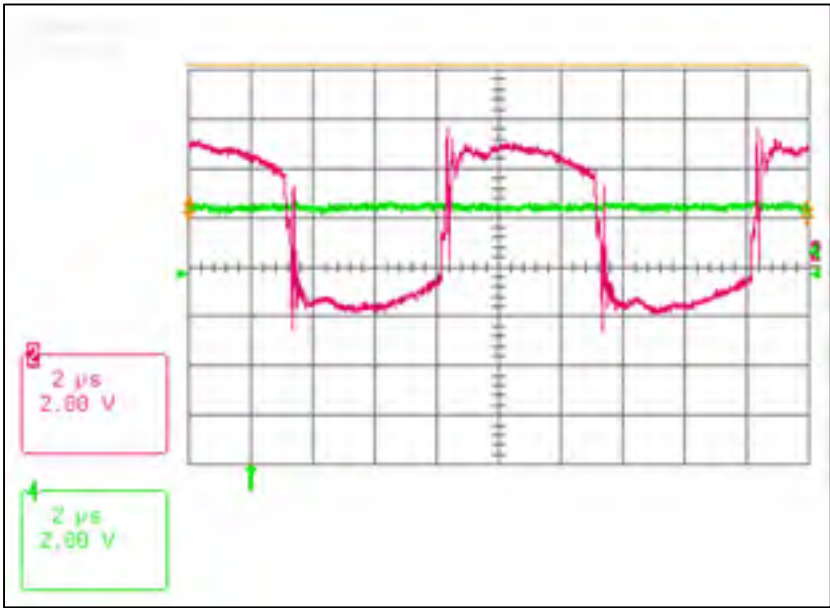


Figure 6.9 Voltage levels at battery and in the secondary coil

6.5 System efficiency

In the following Table 6.1, the efficiency of the system is presented as well as the air gap between the two coils. As it was explained in the introduction, WPT system efficiency is around 80%. The minimum air gap variation that can be evaluated is 1 cm because of the screws and nuts on the mechanical setup.

Table 6.1 Efficiency.

Air Gap	Efficiency
1 cm	80%
2cm	79%
5 cm	15%
10 cm	9%



## 6.6 200 W System

An application of the WPT system developed by the company Infineon and Würth Elektronik was bought for the GREPCI Lab, with an efficiency of 61% with 1 cm Airgap variation. This system is a plug-in device, small and easy to connect with a maximum coil distance of 10mm. The  $V_{RMS}$  on the primary (channel 1, Yellow) was 34.16 V and on the secondary (Channel 2, red), it was 20.66 V which verify the expected efficiency of around 60.5 %. In Figure 6.10 and Figure 6.11, the setup connections are shown.

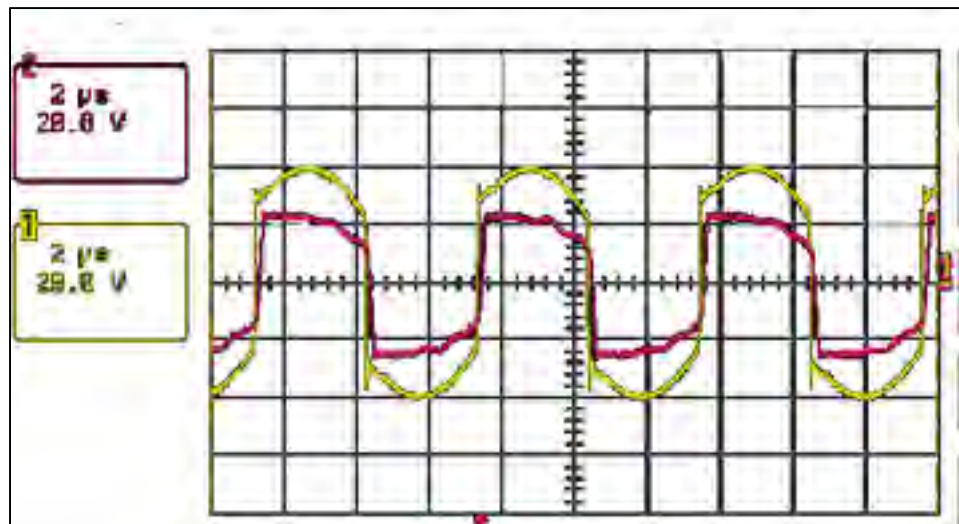


Figure 6.10 Waveforms from 200 W kit showing both v and i



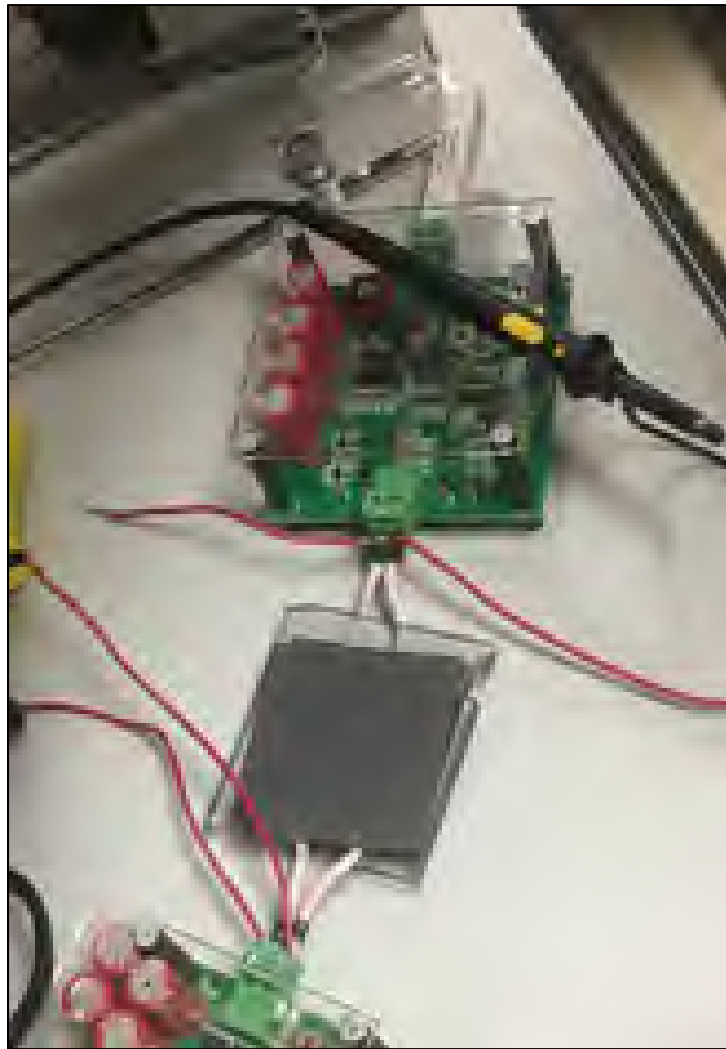


Figure 6.11 200 W kit hardware setup in GREPCI Lab

In this chapter, experimental results were shown, with a maximum input voltage of 10 V and the air gap was tested between 1 cm to 10 cm, when the maximum efficiency of the system is 80% at 1 cm and the maximum voltage of 3 V in the battery with 100 kHz. Moreover, a 200 W kit from Würth Elektronik was tested with a 61% of efficiency.



## CONCLUSION

In this thesis, the design of a WPT system for a scooter battery was presented with the purpose of give a solution for a disable people.

In Chapter 1, the most common mobility scooter brands on the market normally Pride, Merits, and Drive were presented the price and versatility, the WPT systems classification was described.

In Chapter 2, the design of the DC-DC converter able to reduce the switching loss and improve the efficiency of the system, in addition to having magnetic components reduced in size by high operating frequency was presented. In addition, the FHA approximation helps to understand the operation regions of resonant converters. The output voltage can be linked to the converter through a transfer function of the LLC resonant tank. The first harmonic approximation helps to provide an effective Q factor of the converter and a switching frequency approximately close to resonance.

In chapter 3, it was shown that the coil design with the spiral circular flat is the most useful because it has a better performance with misalignment. Moreover, the Litz wire coils are usually designed for a high frequency in WPT systems.

In chapter 4, a PI compensator is designed and simulated in MATLAB. The stability of continuous and discrete-time control systems was also shown. The application of Bode diagrams and Root Locus plots for control system design was shown. Lastly, a voltage control loop was selected.

In chapter 5, the experimental validation was presented. The PCB was designed in Proteus, and the hardware setup was assembled in the electrical department of GREPCI laboratory.

Finally, in chapter 6, the laboratory test results of the power wireless systems were presented with a maximum efficiency of 80% at 100 k.















## APPENDIX A

```
clear all clc
%%%%%%%%%%%%%%%%%%%%%%%%%%%%%%%%%%%%%%%%%%%%%%%%%%%%%%%%%%%%%%%%%%%%%%%% M Variation in function of Fn and
Qe %%%%%%%%%%%%%%%%%%%%%%%%%%%%%%%%%%%%%%%%%%%%%%%%%%%%%%%%%%%%%%%%%%%%%%%%%

Fn_max=5;
Fn_min=0.5;
step=0.001;
Lr=58e-6;
Lm=150e-6;

Ln=3.5;
Qe=[0.05  0.12  0.187  0.25  0.311  0.374  0.43  0.498
    0.5609 0.6232 0.6855];

X=zeros(1,((Fn_max-Fn_min)/step)+1);
Y=zeros(1,((Fn_max-Fn_min)/step)+1);
F0=zeros(1,length(Qe));
j=1;
k=1;
for i=1:length(Qe)
    for Fn=Fn_min:step:Fn_max
        Mn=abs(((Fn^2)*(Ln-1))/((Ln*(Fn^2)-
1)+(Qe(1,i))*(Ln-1)*((Fn^2)-1)*Fn)*1i));
        X(1,j)=Mn;
        Y(1,j)=Fn;
        j=j+1;
    end
end
```



```
[a,b]=find(X==max(X));  
Max=X(a,b);  
F0(i)=Max;  
Fs_gmax=Y(a,b);    figure(4);  
hold on  
plot(Y,X);  
plot(Fs_gmax,Max, 'b--*');  
grid on  
hold on  
j=1;
```



## APPENDIX B

On the input side, the fundamental voltage the square wave voltage  $V_{sq}$  :

$$v_{sq,1}(t) = \frac{2}{\pi} \cdot V_{DC} \cdot \sin(2\pi f_s t)$$

Its RMS value is:

$$V_{sq,1} = \frac{\sqrt{2}}{\pi} \cdot V_{DC}$$

On the output side,  $V_{so}$  is approximated as a square wave and its fundamental voltage is defined as follow:

$$v_{oe}(t) = \frac{4}{\pi} \cdot n \cdot V_o \cdot \sin(2\pi f_s t - \varphi_V)$$

Where  $\varphi_V$  is the phase angle between  $V_{oe}$  and  $V_{sq,1}$ .

The RMS output voltage is defined as follow:

$$V_{oe} = \frac{2\sqrt{2}}{\pi} \cdot n \cdot V_o$$

The fundamental component of current corresponding to  $V_{oe}$  and  $I_{oe}$  is:

$$i_{oe}(t) = \frac{\pi}{2} \cdot \frac{1}{n} \cdot I_o \cdot \sin(2\pi f_s t - \varphi_i)$$

Where  $\varphi_i$  is the phase angle between  $i_{oe}$  and  $v_{oe}$  and the RMS output current is:

$$I_{oe} = \frac{\pi}{2\sqrt{2}} \cdot \frac{1}{n} \cdot I_o$$

The AC equivalent load resistance  $R_e$  can be calculated as follow:

$$R_e = \frac{V_{oe}}{I_{oe}} = \frac{8 \cdot n^2}{\pi^2} \cdot \frac{V_o}{I_o} = \frac{8 \cdot n^2}{\pi^2} \cdot R_L$$

The circuit is a single sinusoidal AC circuit so the calculation can be made in the same way as for all sinusoidal circuits.



The angular frequency is :

$$\omega_s = 2\pi f_s = \omega$$

The capacitive and inductive reactance of  $C_r$ ,  $L_r$  and  $L_m$  are respectively:

$$X_{Cr} = \frac{1}{\omega C_r}, X_{Lr} = \omega \cdot L_r \text{ and } X_{Lm} = \omega \cdot L_m$$

The RMS magnetizing current is:

$$I_m = \frac{V_{oe}}{\omega \cdot L_m} = \frac{2\sqrt{2}}{\pi} \cdot \frac{n \cdot V_o}{\omega \cdot L_m}$$

The circulating current in the series resonant circuit is:

$$I_r = \sqrt{I_m^2 + I_{oe}^2}$$

The voltage gain function is :

$$M_{g\_DC} = \frac{n \cdot V_o}{\frac{V_{in}}{2}} = \frac{n \cdot V_o}{\frac{V_{dc}}{2}}$$

The DC voltage and output voltage are converted into switching mode.

The voltage gain function can be approximated as the bipolar square wave voltage  $V_{so}$  to the unipolar square wave voltage  $V_{sq}$  :

$$M_{g\_DC} \approx M_{g\_sw} = \frac{V_{so}}{V_{sq}}$$

The AC voltage ratio  $M_{g\_AC}$  can be approximated using fundamental components  $V_{sq,1}$  and  $V_{oe}$  replacing respectively  $V_{sq}$  and  $V_{so}$  .:

$$\begin{aligned} M_{g\_DC} &= \frac{n \cdot V_o}{\frac{V_{in}}{2}} \approx M_{g\_sw} \\ &= \frac{V_{so}}{V_{sq}} \approx M_{g\_AC} = \frac{V_{oe}}{V_{sq,1}} \end{aligned}$$



$M_g$  will be used to simplify the notation and replace  $M_{g\_AC}$  then the input to output voltage gain becomes:

$$M_g = \frac{V_{oe}}{V_{sq,1}} = \left| \frac{jX_{Lm} || R_e}{(jX_{Lm} || R_e) + j(X_{Lr} - X_{Cr})} \right|$$

$$= \left| \frac{(j\omega L_m) || R_e}{(j\omega L_m) || R_e + j\omega L_r + \frac{1}{j\omega C_r}} \right|$$

Where  $j = \sqrt{-1}$ .

Then the following approximation can be used:

$$V_o = M_g \cdot \frac{1}{n} \cdot \frac{V_{in}}{2}$$

The normalized format of the voltage gain can be calculated using the normalized frequency  $f_n$ , inductance ratio  $L_n$  and quality factor  $Q_e$  :

$$M_g = \left| \frac{L_n \cdot f_n^2}{[(L_n + 1) \cdot f_n^2 - 1] + j[(f_n^2 - 1) \cdot f_n \cdot Q_e \cdot L_n]} \right|$$

The input and output voltage relationship can also be obtained as follow:

$$V_o = M_g \cdot \frac{1}{n} \cdot \frac{V_{in}}{2} = M_g(f_n, L_n, Q_e) \cdot \frac{1}{n} \cdot \frac{V_{DC}}{2}$$

Where  $V_{in} = V_{DC}$ .







## APPENDIX C

```
%% Modeling Resonant Coupled Wireless Power
Transfer System
% This example shows how to create and analyze a
resonant coupling type
% copyright 2015 The MathWorks, Inc.

%%wireless power transfer(WPT) system with emphasis
on concepts such as
% resonant mode, coupling effect, and magnetic
field pattern. The analysis
% is based on a 2-element system of spiral
resonators.
%
% This example requires the following product:
%
% * Partial Differential Equation Toolbox(TM)

% C Design Frequency and System Parameters
% Choose the design frequency to be 30MHz. This is
a popular frequency for
% compact WPT system design. Also specify the
frequency for broadband
% analysis, and the points in space to plot near
fields.
clc

fc=100e6;
fcmin = 75e6;

fcmax = 113e6;
fband1 = 70e6:1e6:fcmin;
fband2 = fcmin:0.25e6:fcmax;
fband3 = fcmax:1e6:115e6;
```



```

freq = unique([fband1 fband2 fband3]);
pt=linspace(-0.3,0.3,61);
[X,Y,Z]=meshgrid(pt,0,pt);
field_p=[X(:)';Y(:)';Z(:)'];

%% The Spiral Resonator
% The spiral is a very popular geometry in a
resonant coupling type
% wireless power transfer system for its compact
size and highly confined
% magnetic field. We will use such a spiral as the
fundamental element in
% this example.

%%
% *Create Spiral Geometry* The spiral is defined by
its inner and outer
% radius, and number of turns. Express the geometry
by its boundary points,
% then import its boundary points into pdetool. The
mesh is generated in
% pdetool and exported. The mesh is described by
points and triangles.
Rin=0.07;
Rout=0.15;
N=20;
[p,t]=createSpiral(Rin,Rout,N);
%%
% *Create custom antenna* Use customAntennaMesh to
import the mesh.
% The feed is created at the inner circle of the
spiral mesh. This
% structure is now ready for analysis.
spiralobj=customAntennaMesh(p,t);
spiralobj.Tilt=90;
spiralobj.TiltAxis='Y';
createFeed(spiralobj);

```



```

spiralobj = spiralArchimedean('NumArms', 1,
    'Turns', N, ...
    'InnerRadius', Rin, 'OuterRadius', Rout,
    'Tilt', 90, 'TiltAxis', 'Y');

%% Resonance Frequency and Mode
% It is important to find the resonant frequency of
the designed spiral
% geometry. A good way to find the resonant
frequency is to study the
% impedance of the spiral resonator. Since the
spiral is a magnetic
% resonator, a lorentz shaped reactance is expected
and observed in the
% calculated impedance result.
figure;
impedance(spiralobj,freq);

%%
% Since the spiral is a magnetic resonator, the
dominant field component of
% this resonance is the magnetic field. A strongly
localized magnetic field
% is observed when the near field is plotted.
figure;
EHfields(spiralobj,fc,field_p,'ViewField','H','ScaleFields',[0 5]);

%% Create Spiral to Spiral Power Transfer System
% The complete wireless power transfer system is
composed of two parts: the
% transmitter(Tx) and receiver(Rx). Choose
identical resonators for both
% transmitter and receiver to maximize the transfer
efficiency. Here, the
% wireless power transfer system is modeled as a
linear array.

```



```

wptsys=linearArray('Element',[spiralobj
spiralobj]);
wptsys.ElementSpacing=Rout*2;
figure;
show(wptsys);

%% Variation of System Efficiency with Transfer
Distance
% One way to evaluate the efficiency of the system
is by studying the S21
% parameter. As presented in [1], the system
efficiency changes rapidly
% with operating frequency and the coupling
strength between the
% transmitter and receiver resonator. Peak
efficiency occurs when the
% system is operating at its resonant frequency,
and the two resonators are
% strongly coupled. The results for s-parameter
analysis has been
% precomputed and stored in a MAT-file.
%load arraysparam
%figure;
%rfplot(sparam,2,1,'abs');

%%
% *Critical Coupled Point* The coupling between two
spirals increases with
% decreasing distance between two resonators. This
trend is approximately
% proportional to  $1/d^3$ . Therefore, the system
efficiency increases with
% shorter transfer distance until it reaches the
critical coupled regime
% [1]. When the two spirals are over coupled,
exceeding the critical

```



```

% coupled threshold, system efficiency remains at
% its peak, as shown in
% Fig.3 in[1]. We observe this critical coupling
% point and over coupling
% effect during modeling of the system. Perform a
% parametric study of the
% system s-parameters as a function of the transfer
% distance. The transfer
% distance is varied by changing the
% ElementSpacing. It is varied from half
% of the spiral dimension to one and half times of
% the spiral dimension,
% which is twice of the spiral's outer radius. The
% frequency range is
% expanded and set from 25 MHz to 36 MHz.
freq=(80:0.1:115)*1e6;
dist=Rout*2*(0.6:0.1:1.6);

load('wptData.mat');
s21_dist=zeros(length(dist),length(freq));
for i=1:length(dist)
    s21_dist(i,:)=rfparam(sparam_dist(i),2,1);
end

figure;
[X,Y]=meshgrid(freq/1e3,dist);
surf(X,Y,abs(s21_dist),'EdgeColor','none');
view(150,20);
shading(gca,'interp');
axis tight;
xlabel('Frequency [MHz]');
ylabel('Distance [m]');
zlabel('S_{21} Magnitude');

figure;
plot(Y,abs(s21_dist));
figure;

```



```

plot(X,abs(s21_dist));

%% Coupling Mode between Two Spiral Resonator
% The dominant energy exchange mechanism between
the two spiral resonators
% is through the magnetic field. Strong magnetic
fields are present between
% the two spirals at the resonant frequency.
wptsys.ElementSpacing=Rout*2;
figure;
EHfields(wptsys,fc,field_p,'ViewField','H','Scale
Fields',[0 5]);
view(0,0);

%% Conclusion
% The results obtained for the wireless power
transfer system match well
% with the results published in [1].

%% References
%
% [1] A. P. Sample, D. T. Meyer, and J. R. Smith,
"Analysis, Experimental
% Results, and Range Adaptation of Magnetically
Coupled Resonators for
% Wireless Power Transfer", IEEE Transactions on
Industrial Electronics,
% pp.544-554, 58, 2, 2011.

CREATE SPRIAL FUNCTION

function [p,t]=createSpiral(Rin,Rout,N)
% This function is only for supporting the wireless
power transfer example.
% It may be removed in future release.

% Copyright 2015 The MathWorks, Inc.

```



```

%% Define spiral by its boundary points
width=(Rout-Rin)/4/N;
spacing=width;
growthRate=(width+spacing)/pi;

phi_start=0;
phi_end = ((Rout-width)-Rin)/growthRate;
delta_phi=pi/20;

phi=phi_start:delta_phi:phi_end;

r1=Rin+growthRate.*phi;
x1=r1.*cos(phi+0);
y1=r1.*sin(phi+0);

r2=Rin+width+growthRate.*phi;
x2=r2.*cos(phi+0);
y2=r2.*sin(phi+0);

xs1 = [x1';fliplr(x2)'];
ys1 = [y1';fliplr(y2)'];

xlim = [-1.2*Rout , 1.2*Rout];
ylim = [-1.2*Rout, 1.2*Rout];

%% Generate mesh in pde tool with specified spiral
boundary.
[pde_fig,ax] = pdeinit;
set(pde_fig,'Name','Spiral')
set(ax,'XLim',xlim);
set(ax,'YLim',ylim);
set(ax,'XTickMode','auto');
set(ax,'YTickMode','auto');
set(ax,'XGrid','on');
set(ax,'YGrid','on');
setappdata(pde_fig,'MesherVersion','R2013a');

pdepoly(xs1,ys1,'W1')

```



```
% mesh spiral
meshmenu = pde_fig.Children(20);
meshmenuchildren = meshmenu.Children;
eval(meshmenuchildren(9).Callback);

% extract p t
p = getappdata(pde_fig,'p1');
t = getappdata(pde_fig,'t1');

end
```



## LIST OF BIBLIOGRAPHICAL REFERENCES

- A. E. Ruehli, G. A. a. L. J. (2012). Skin-effect model for round wires in PEEC,. *IEEE International Symposium on Electromagnetic Compatibility*, pp. 1-6.
- Abou Houran, M. Y., xu & Chen, Wenjie. (2018). Magnetically Coupled Resonance WPT: Review of Compensation Topologies, Resonator Structures with Misalignment, and EMI Diagnostics. *electronics*( 7. 10.3390/electronics7110296).
- Aditya, K. (2016). *DESIGN AND IMPLEMENTATION OF AN INDUCTIVE POWER TRANSFER SYSTEM FOR WIRELESS CHARGING OF FUTURE ELECTRIC TRANSPORTATION*. (Degree of Doctor of Philosophy). University of Ontario, University of Ontario Institute of Technology Oshawa, Ontario, Canada.
- Akhbari, M. H. a. M. (2009). New approach in design of planar coil of induction cooker based on skin and proximity effects analysis. *IEEE International Conference on Industrial Technology*, pp. 1-6.
- B. Esteban, N. S., M. Sid-Ahmed and N. C. Kar. (2015). Development of mutual inductance formula for misaligned planar circular spiral coils. *2015 IEEE Energy Conversion Congress and Exposition (ECCE), Montreal, QC, 2015, pp. 1306-1313*.
- B. Kim, K. P. a. G. M. (2012). Asymmetric PWM Control Scheme During Hold-Up Time for \$LLC\$ Resonant Converter. *IEEE Transactions on Industrial Electronics*, 59(7).
- C. R. Sullivan. (1999). Optimal choice for number of strands in a litz-wire transformer winding. *IEEE Trans. on Power Electronics*, vol 14 n2 pp. 283–291.
- C. R. Sullivan and R. Y. Zhang. (2014). Simplified design method for litz wire. *Proc. IEEE Applied Power Electronics Conference and Exposition*,, pp. 2667-2674.
- Campi, T. C., S.; Palandrani, F.; De Santis, V.; Hirata, A.; Feliziani, M. (2016). Wireless power transfer charging system for AIMDs and pacemakers. *IEEE Transactions on Microwave Theory and Techniques*, 64(2), 633 - 642. doi:10.1109/TMTT.2015.2511011.
- Cem Som, D. M. A. d. R. (2019). Basic principles. In S. H. Jana Haisch (Ed.), *Trilogy of wireless power transfer* (pp. 14-18). Germany: Wurth Elektronik eiSos GmbH & Co. KG.



Chabalko, M. J. S., A.P. (2014). Resonant cavity mode enabled wireless power transfer. *Appl. Phys. Lett.*

Corp, P. M. P. (2012). Owner's manual, GoGo Elite. In Pride (Ed.).

Elektronik, I. a. W. (2019). Manual 200W Wireless Power Development Kit. *760308EMP*, 1-10.

F. Musavi, M. C., D. S. Gautam, W. Eberle and W. G. Dunford. (2013). An LLC Resonant DC–DC Converter for Wide Output Voltage Range Battery Charging Applications. *IEEE Transactions on Power Electronics*, 28(12), 5437-5445.

H. Mizutani, T. M. a. M. N. (2013). *A dual pulse modulated five-element multi-resonant DC-DC converter and its performance evaluations*. Paper presented at the IEEE Energy Conversion Congress and Exposition, Denver, CO.

H. Wu, T. M., X. Gao and Y. Xing. (2015). A Secondary-Side Phase-Shift-Controlled LLC Resonant Converter With Reduced Conduction Loss at Normal Operation for Hold-Up Time Compensation Application. *IEEE Transactions on Power Electronics*, 30(10).

Hekal, S. A.-R., A.B.; Jia, H.; Allam, A.; Barakat, A.; Pokharel, R.K. (2017). A Novel Technique for Compact Size Wireless Power Transfer Applications Using Defected.

Ground Structures. *IEEE Transactions on Microwave Theory and Techniques*, 66(2), 591 - 599. doi:10.1109/TMTT.2016.2618919.

Huang, H. (2011). Designing an LLC resonant half-bridge power converter. *Power supply design seminar*.

TAXONOMY & CLASSIFICATION OF POWERED MICROMOBILITY VEHICLES, (2019).

J. Liao, J. W., J. Zhang and Z. Qian. (2011). *A novel current driving scheme for LLC resonant converter with Synchronized voltage-doubler rectifier*. Paper presented at the Twenty-Sixth Annual IEEE Applied Power Electronics Conference and Exposition, Fort Worth, TX.

J. M. Miller and A. Daga. (2015). Elements of Wireless Power Transfer Essential to High Power Charging of Heavy Duty Vehicles. *IEEE Trans. on Transportation Electrifications*,, *voll*, pp. 26–39.

J. Sallan, J. L. V., a. Llombart, and J. F. Sanz,. (2009). Optimal Design of ICPT Systems Applied to Electric Vehicle Battery Charge. *IEEE Trans.on Industrial Electronics*,, vol. 56, no. 56, pp. 2140–2149.



- Jain, M. Z. Y. a. P. K. (2007a). *Design and Performance of a Resonant LLC 48V Voltage Regulator Module with a Self-sustained Oscillation Controller*. Paper presented at the Twenty-Second Annual IEEE Applied Power Electronics Conference and Exposition, Anaheim, CA, USA.
- Jain, M. Z. Y. a. P. K. (2007b). Series–Parallel Resonant Converter in Self-Sustained Oscillation Mode With the High-Frequency Transformer-Leakage-Inductance Effect: Analysis, Modeling, and Design. *IEEE Transactions on Industrial Electronics*, 54(3).
- Jawad, A. M. N., R.; Gharghan, S.K.; Jawad, H.M.; Ismail, M. (2017). Opportunities and Challenges for Near-Field Wireless Power Transfer: A Review. *Energies*, 10.
- Jeong, I. S. J., B.I.; You, D.S.; Choi, H.S. (2016). Analysis of S-Parameters in Magnetic Resonance WPT Using Superconducting Coils. *IEEE Transactions on Applied Superconductivity*, 26(3). doi:10.1109/TASC.2016.2544139.
- Jiang, C. C., K.T. & Chunhua, Liu & Lee, Christopher Ho Tin. (2017). An Overview of Resonant Circuits for Wireless Power Transfer. *Energies*, 10.
- Kang, S. H. J., C.W. (2017). Textile Resonators with Thin Copper Wire for Wearable MR-WPT System. *IEEE Microwave and Wireless Components Letters*, 27(1), 91 - 93. doi:10.1109/LMWC.2016.2629976.
- Kim, M. K., H.; Kim, D.; Jeong, Y.; Park, H.H.; Ahn, S. (2015). A Three-Phase Wireless-Power-Transfer System for Online Electric Vehicles with Reduction of Leakage Magnetic Fields. *IEEE Trans. Microw. Theory Tech.*
- Kim, M. K., H.; Kim, D.; Jeong, Y.; Park, H.H.; Ahn, S, A. (2015). Three-Phase Wireless-Power-Transfer System for Online Electric Vehicles with Reduction of Leakage Magnetic Fields. *IEEE Trans. Microw. Theory Tech.*
- L. Sahaya Senthamil, P. P. a. V. R. (2012). *Design and implementation of LLC resonant half bridge converter*. Paper presented at the IEEE-International Conference On Advances In Engineering, Science And Management, Nagapattinam, Tamil Nadu.
- Li, W. Z., H.; Deng, J.; Li, S.; Mi, C.C. (2016). Comparison study on SS and double-sided LCC compensation topologies for EV/PHEV wireless chargers. *IEEE Trans. Veh. Technol.*
- Li, W. Z., H.; Deng, J.; Li, S.; Mi, C.C. (2018). Comparison study on SS and double-sided LCC compensation topologies for EV/PHEV wireless chargers. *IEEE Trans. Veh. Technol.* 2016, 65, 4429-4439. doi:10.1109/TVT.2015.2479938.
- Lind, A. (2013). *LLC Converter Design Note*.



Longzhao Sun, D. M., Houjun Tang,. (2018). A review of recent trends in wireless power transfer technology and its applications in electric vehicle wireless charging. *Renewable and Sustainable Energy Review*, 91, 490-503. doi:<https://doi.org/10.1016/j.rser.2018.04.016>.

Manufacturing, D. M. D. (2017). Scout Owner's Manual In D. Medical (Ed.).

Martinelli, J. F. L. a. R. (2001). *Steady-state analysis of the LLC series resonant converter*. Paper presented at the Sixteenth Annual IEEE Applied Power Electronics Conference and Exposition Anaheim, CA, USA.

Merits. Owner's Manual Merits. In Merits (Ed.).

Nakaoka, T. M. a. M. (2009). A Novel High-Frequency Transformer-Linked Soft-Switching Half-Bridge DC–DC Converter With Constant-Frequency Asymmetrical PWM Scheme. *IEEE Transactions on Industrial Electronics*, 56(8).

Oncu, S. K., Akif. (2017). Pulse density modulation controlled converter for PV systems. *International Journal of Hydrogen Energy*, 42.

P. Kowstubha, K. K. a. K. R. R. (2014). *Review on different control strategies of LLC series resonant converters*. Paper presented at the International Conference on Advances in Electrical Engineering Vellore.

Park, M. N., V.T.; Yu, S.D.; Yim, S.W.; Park, K.; Min, B.D.; Kim, S.D.; Cho, J.G. (2016). *A study of wireless power transfer topologies for 3.3 kW and 6.6 kW electric vehicle charging infrastructure*. Paper presented at the 2016 IEEE Transportation Electrification Conference and Expo, Asia-Pacific (ITEC Asia-Pacific), Busan, South Korea. <https://ieeexplore.ieee.org/document/7513041>.

S. Kang, H. K. a. B. C. (2016). Adaptive Voltage-Controlled Oscillator for Improved Dynamic Performance in LLC Resonant Converter. *IEEE Transactions on Industry Applications*, 52(2).

S. W. Kang, H. J. K. a. B. H. C. (2014). *Gain-scheduled control using voltage controlled oscillator with variable gain for a LLC resonant converter*. Paper presented at the 2014 IEEE Energy Conversion Congress and Exposition Pittsburgh.

*Topologies*. Paper presented at the 2018 Texas Instruments Power Supply Design Seminar.

Song, J. K., S.; Bae, B.; Kim, J.J.; Jung, D.H.; Kim, J. (2014). *Design and analysis of magnetically coupled coil structures for PCB-to-active interposer wireless power transfer in 2.5 D/3D-IC*. Paper presented at the 2014 IEEE Electrical Design of



- Advanced Packaging & Systems Symposium (EDAPS), Bangalore, India.  
<https://ieeexplore.ieee.org/document/7030800>.
- Technologies, N. E. W. (2018). Litz types \* construction. Retrieved from  
[www.litzwire.com/litz\\_types.htm](http://www.litzwire.com/litz_types.htm).
- W. Cha, J. K. a. B. K. (2016). Highly Efficient Asymmetrical PWM Full-Bridge Converter for Renewable Energy Sources. *IEEE Transactions on Industrial Electronics*, 63(5).
- W. Feng, D. H., P. Mattavelli, D. Fu and F. C. Lee. (2010). *Digital implementation of driving scheme for synchronous rectification in LLC resonant converter*. Paper presented at the IEEE Energy Conversion Congress and Exposition, Atlanta, GA.
- Wang, Y. Y., Y.; Liu, X.; Xu, D. (2017). S/CLC Compensation Topology Analysis and Circular Coil Design for Wireless Power Transfer. *IEEE Transactions on Transportation Electrification*, 3(2), 496 - 507. doi:10.1109/TTE.2017.2651067.
- Yang, C. T., K. (2014). A Novel Parallel Double Helix Loop Resonator for Magnetic Coupled Resonance Wireless Power Transfer. *PIERS Proceedings*.
- Zhang, F. L., J.; Mao, Z.; Sun, M. (2012). Mid-range wireless power transfer and its application to body sensor networks. *Open J. Appl. Sci*.
- Sheng-Yang, Y., C. Runruo, and V. Ananthakrishnan. (2018). *Survey of Resonant Converter*
- Zhang, W. W., J.C.; Abraham, A.M.; Mi, C.C. (2015). Loosely coupled transformer structure and interoperability study for EV wireless charging systems. *IEEE Transactions on Power Electronics*, 30(11). doi:10.1109/TPEL.2015.2433678.